Space-time evolution of hot and dense matter probed by Bose-Einstein correlation in Au+Au collisions at $\sqrt{s_{\mathrm{NN}}} = 200$ GeV

Akitomo ENOKIZONO

Department of Physical Science
Graduate School of Science, Hiroshima University
Kagamiyama 1-3-1, Higashi-Hiroshima, 739-8526, Japan

September 2004

Abstract

In the framework of Quantum-Chromo-Dynamics (QCD), color-charged quarks and anti-quarks are elementary particles and always confined in a color-less hadron via strong forces intermediated by another color-charged gluons in the QCD vacuum. In an extremely hot and/or dense QCD matter, however, quarks and gluons are expected to be deconfined from hadrons and move freely to one another within the QCD theory. In the cosmology, the new state of such partonic matter, called "Quark-Gluon Plasma" (QGP), is considered to exist in the early Universe in a few μs after the Big-Bang. One can also expect to re-form such a matter in relativistic heavy-ion collisions in a laboratory.

There are many discussions how to distinguish the QGP formation during a process of heavy-ion collisions and some interesting ideas came out such as J/ψ suppression, jet quenching, direct photons enhancement, strangeness enhancement and so on. If a first-order phase transition from the QGP to a hadronic state is assumed, the physical volume is prevented from its fast expansion and cooling due to the softening of the equation of state. Hence, the theory of thermodynamics tells us that one of the crucial signatures could be an enlargement of the physical volume and a prolongation of the duration of particle emission ($\Delta\tau \sim 10$ fm). The method of Bose-Einstein correlation is a powerful tool to study the space-time evolution of the physical volume in the heavy-ion collisions because the width of the correlation peak is inversely proportional to the size of the emitting source, often refered to as "HBT radius", and a multi-dimensional analysis provides us about temporal information of particle emissions from the source.

This thesis presents for the first time the measurement of Bose-Einstein correlations of like-signed pions at the mid-rapidity in Au+Au collisions at $\sqrt{s_{\rm NN}} = 200$ GeV, measured by the PHENIX experiment at the Relativistic Heavy-Ion Collider (RHIC) in Brookhaven National Laboratory, U.S.A. I measured the multi-dimensional HBT radii and the duration of pion emission as a function of two independent external parameters; the mean transverse momentum of pair ($k_{\rm T}$) and the collision centrality in detail.

In the central Au+Au collision, the HBT radii are found to depend strongly on $k_{\rm T}$, indicating a picture of source which correctively expands in the transverse direction. From a comparison with those results at lower energies at AGS or SPS, the transverse HBT radii are realized to be less sensitive to the collision energy, while the longitudinal HBT radius is found to slightly increase as the collision energy increasing from $\sqrt{s_{\rm NN}}$ ~4 to 200

GeV. Taking a hydrodynamics model, the k_{T} dependence of HBT radii shows about 7 fm of the RMS-width of the transverse source size and about 9 fm/c of the life time at hadron freeze-out stage. These results are only a few fm larger than those at AGS energies, even though the center of mass energy increases by nearly one order of magnitude.

Two methodologies are applied in this analysis – the Coulomb correction that has been conventionally used mostly in earlier Bose-Einstein correlation analyses so far, and an improved Coulomb correction that is based on a picture of the core-halo structure. With the conventional Coulomb correction, the duration of pion emission becomes apparently negative which is not acceptable in a physics sense, and cannot be reproduced by any models. Developing the new methodology, I found the duration to be zero within the statistical and systematic errors for all the k_{T} and centrality measured, and then the duration time first gets a physical meaning at this RHIC energy. This is a great success to understand the space-time evolution of the hot and dense matter created in heavy-ion collisions at the RHIC energy and has solved the "HBT-puzzle". However, this experimental result would contradict to a simple picture of "slowly-burning" QGP, in which quarks are slowly hadronized with a long-lived mixed phase due to the first-order phase transition. There are still room to study properties of QGP, especially in terms of the order of the phase transition between the QGP and hadronic phases.

Contents

List of Figures

List of Tables

Acknowledgement

I first would like to express my great gratitude to my supervisor, Prof. T. Sugitate of Hiroshima University for his extensive advice and full support during this thesis work. He continuously supervises and encourages me to get involved in the PHENIX experiment. I am also deeply grateful to Prof. R.A. Soltz of Lawrence Livermore National Laboratory (LLNL) for his specialized advice and discussions in this analysis. His thoughtful and well-informed suggestions lead this thesis up to one of fruitful researches in the relativistic heavy-ion collisions at RHIC.

I would like to express my gratitude to co-authors of the Bose-Einstein correlation analysis at PHENIX: Dr. S.C. Johnson, Dr. M. Heffner, Dr. J.M. Burward-Hoy and Dr. J.P. Sullivan for their kind help and meaningful discussions. I also would like to thanks to Prof. S.Y. Fung and Dr. H.V. Hecke for their careful supports for the publication of this analysis. I wish to express my thanks to Dr. H. Ohnishi, Dr. T. Chujo, Dr. H. Torii and Dr. T. Kohama for their technical supports to start up this two-particle correlation analysis. I would like to express my thanks to Dr. Y. Akiba, Prof. B.V. Jacak, Dr. M. Kaneta and Dr. T. Csörgő for their valuable comments and useful suggestions on the publication and my presentations. I also acknowledge co-conveners: Dr. A. Franz, Dr. J.T. Mitchell, Prof. J. Velkovska, Dr. S. Esumi and especially Prof. C. Ogilvie for their supports and advices on this analysis at the Global and Hadron Physics Working Groups.

I would like to express great thanks to all of the collaborators of the PHENIX experiment. This analysis would never be possible without their great supports – developments of state-of-the-art detectors, works on data taking in the Counting House and skillful calibrations of data. I wish to thank Prof. W.A. Zajc, the spokesperson of the PHENIX

experiment, for his gladly accepting and supporting me as a member of the PHENIX Collaboration. I wish to appreciate Prof. H. Hamagaki, Prof. E.J. O'Brien, Dr. B. Johnson, Ms. D. Earley, Dr. Y. Akiba and Dr. K. Ozawa for their supports and kind hospitality during stay at Brookhaven National Laboratory.

I wish to express my thanks to emeritus Prof. Y. Sumi, Prof. O. Miyamura and Prof. T. Ohsugi for introducing me to the field of high energy experimental physics, and Prof. K. Shigaki and Dr. K. Homma for their encouragements and educational suggestions. I also would like to express my gratitude to colleagues at Hiroshima University: Mr. T. Hachiya, Mr. T. Nakamura, Mr. N. Sugita, Mr. R. Kohara and Mr. Y. Tsuchimoto. Some valuable discussions and joyful conversations with them gave me some physics insight into heavy-ion experiments.

Finally, I express my greatest thanks to my parents for giving me a great deal of support, cheering me up at all times.

Chapter 1

Introduction

1.1 Relativistic Heavy-Ion Experiments

1.1.1 Quark-gluon plasma

"How nuclear matter was created after the Big-Bang, and how it can be created at present world?" The nature of quark matter at extreme high energy density, which is believed to exist in the early universe in a few μs after the Big-Bang, is one of the most interesting themes not only for cosmologists but also for particle and nuclear physicists because a new form of quark matter is theoretically expected to be created at a high energy density.

According to the Quantum-Chromo-Dynamics (QCD) theory, quarks and anti-quarks, which are elementary particles in the QCD frame, interact with one another exchanging gluons, namely strong force. In the QCD vacuum, the effective coupling constant decreases as the 4-momentum transfer increases at small distance of the interaction range, called "asymptotic freedom". Thus, in a normal condition, color-charged quarks are always confined in neutral color (color-singlet) states, comprising baryons (3-quark bound state) or mesons (2-quark bound state) by exchanging their color charges through gluons. At extremely high density and/or temperature, however, the color force between quarks for long distance is screened by dense gluons, allowing quarks to propagate for a long distance. In such a medium, quarks are deconfined and can traverse freely to one another. The deconfinement state is referred to as "Quark-Gluon Plasma" (QGP) because of the QCD

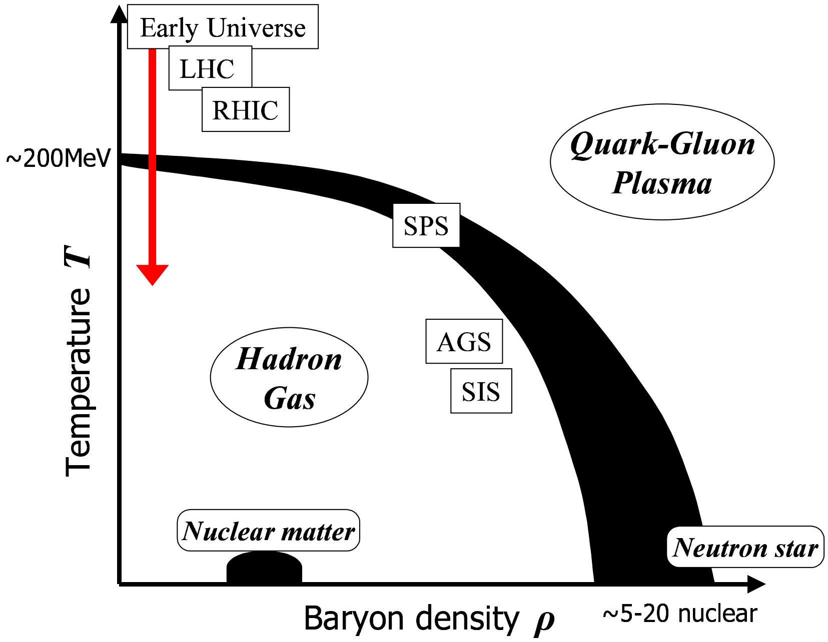

Figure 1.1: A phase diagram of nuclear matter as a function of baryon density ρ and temperature T. Hadronic phase is shown at low density and temperature, and the QGP phase is shown at high density and/or temperature, separated by mixed phase shown by the black band. The predicted transitions from hadronic to QGP phase at RHIC and LHC experiments are shown by arrows.

analogue of the plasma phase of ordinary atomic matter.

At one extreme condition, the QGP state is expected to exist in the center of cold neutron stars, in which the baryon density reaches about 10 times more than that of ordinary nuclear matters on earth. In our world, relativistic heavy-ion collisions would provide the unique opportunity to study the nature of nuclear matter at such a high energy density, which could be the QGP state, in the laboratory. Recent lattice QCD models, which can provide a treatment of non-perturbative QCD using lattice gauge simulation from the first principle, predict that the QGP state could be formed at a high energy density around a few GeV/fm^3, corresponding to the temperature of a few hundred MeV.

Fig. 1.1 shows a naive phase diagram of nuclear matter as a function of baryon density and temperature, and how the QGP state can be explored in relativistic heavy-ion collisions. To study nature of the state of high baryon and/or energy densities, enormous experimental effort has been carried out in the fixed target programs using Bevatron at Lawrence Berkeley National Laboratory (LBNL), the Alternating Gradient Synchrotron (AGS) at Brookhaven National Laboratory (BNL), and also the Super Proton Synchrotron (SPS) at CERN. Despite some of the experimental results suggest the signatures of the QGP formation in the AGS-SPS energies [1, 2], the smoking gun has not been confirmed in the fixed target experiments. Following the fixed target experiments till 1999, the study of high energy nuclear collisions has opened a new stage with the Relativistic Heavy-Ion Collider (RHIC) at BNL, where the initial energy density in central collisions is expected to be sufficient for QGP formation.

1.1.2 Space-time evolution of heavy-ion collisions

In the relativistic heavy-ion collisions, nuclei are contracted in the beam direction like pancakes due to the Lorentz boost. Fig. 1.2 shows a schematic drawing of a heavy-ion collision. The number of nucleons participating in the collision, called “participants”, and the rest that do not participate in the collision, called “spectators”, could be geometrically determined by cut with the straight line at the impact parameter b, namely the length of the overlap region of colliding two nuclei.

In heavy-ion collisions at RHIC, the participants may deposit the energy density about 5 fm/cm^3, equivalent to the temperature about 300 MeV. The energy density is sufficient to form the QGP state comparing to the QGP formation temperature evaluated by lattice QCD to be of the order of 1$-$3 GeV/fm^3, corresponding to the temperature T = 150$-$200 MeV. Similar to the phase transition of an ideal gas, the evolution of a heavy-ion collision from QGP to hadronic state is described in terms of the equation of state. The order of the transition is still open question, and the investigation is one of the important topics in heavy-ion programs. For a good example, Fig. 1.3 show a schematic diagram of the space-time evolution of the medium in relativistic heavy-ion collisions assuming the first-order phase transition, where the “space” corresponds to the extent of the longitudinal source size. The space-time evolution is summarized as four different stages below:

1. In the initial stage of collisions, labelled as "pre-equilibrium" in Fig. 1.3, processes of parton-parton hard scatterings may predominantly occur in the overlap region of two colliding nuclei, depositing a large amount of energy in the medium. The matter is not still in thermal equilibrium state and perturbative QCD models can describe its dynamics by a cascade of freely colliding partons. The time of the pre-equilibration state is predicted to be about 1 fm/c or less.
2. After the short pre-equilibration time, the QGP phase would be formed, in which parton-parton and string-string interactions reach thermal equilibration state. The volume of the QGP state, which energy density is expected to reach above 3−5 GeV/fm^3, equivalent to the temperature 200−300 MeV, rapidly expands with decreasing its temperature and energy density.
3. If the first-order phase transition is assumed, the "mixed phase" is expected to exist between the QGP and hadron phases, in which quarks and gluons are being again confined into hadrons at the critical temperature T_c. At the mixed phase, the entropy density is being transferred into lower degrees of freedom, and therefore, the system is prevented from its fast expansion and cooling due to the "softest point" defined by a minimum ε/p (pressure/energy density) in the equation of state. This leads to a maximum in the lifetime of the mixed phase, which is expected to last for a relatively long time ($\tau > 10$ fm/c) during the softening of the equation of state.
4. In the hadronic phase, the system keep collective expansion via hadron-hadron interactions, decreasing its temperature. Then, the hadron interactions cease when the system reaches a certain size and temperature (called the hadron freeze-out temperature T_f), and hadrons freely stream out from the medium to be detected.

1.2 Approach to a quark-gluon deconfined state

Unlike the plasma of ordinary atomic matter, most of the observables in the relativistic heavy-ion collisions may not be direct signals of the QGP formation due to the fun-

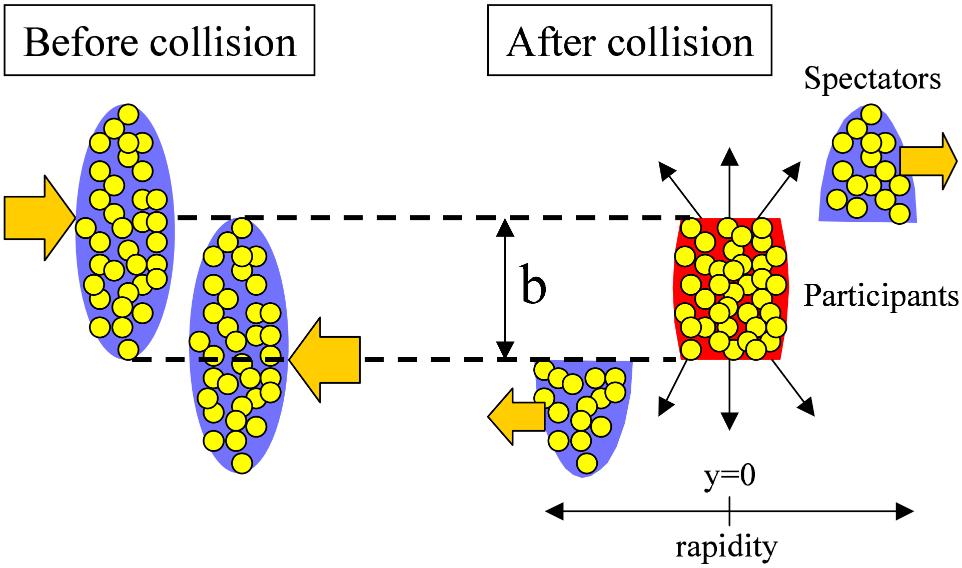

Figure 1.2: A schematic diagram of a heavy-ion collision. Nucleons are geometrically separated into participants and spectators for the impact parameter b.

damental confining property of the physical QCD vacuum. Instead, most experimental investigations should rely on the indirect signatures which are sensitive to the transient QGP state. This section introduces the approaches to investigate the QGP formation and its phase transition to hadronic matter, and the space-time evolution of the medium produced in the relativistic heavy-ion collisions.

1.2.1 Medium effect

The observation of the so-called "jet quenching" effect is a prominent signature of the medium effect of the QGP [7]. In the RHIC energy, parton hard scatterings with large 4-momentum transfer happen at the initial stage of collision. In the $p+p$ or $p+\bar{p}$ collisions in the RHIC energy range, the scattered high p_{T} partons can be observed as two back-to-back jets that fragment into high p_{T} hadrons at p_{T} >2 GeV/c, and the production rate is well calculated by perturbative QCD. If the QGP is formed in the heavy-ion collisions, the scattered high p_{T} partons may loose their large fraction of momentum by induced gluon bremsstrahlung when traversing in the hot and dense color field, resulting

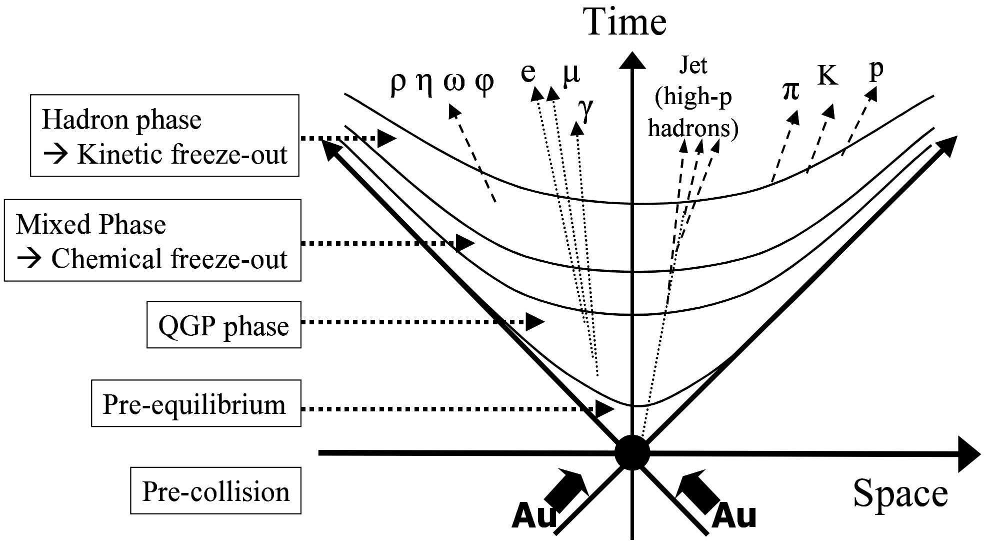

Figure 1.3: A schematic diagram of space-time evolution of a relativistic heavy-ion collision.

in the suppression of high $p_{\rm T}$ particle. To study the suppression, the so-called "nuclear modification factor" (R_{AA}) has recently been measured in heavy-ion experiments at RHIC. The R_{AA} is defined by the ratio of the yield of high-$p_{\rm T}$ particle in nucleus-nucleus collisions to the yield in nucleon-nucleon collisions normalized by the number of binary scaled nucleon-nucleon collisions, and it should be unity if there is no any medium effect in the nucleus-nucleus collisions.

The PHENIX collaboration has reported that R_{AA} of charged hadrons measured in $Au + Au$ collisions is significantly suppressed less than unity while that measured in deuteron (d)+Au collisions is apparently more than unity at high $p_{\rm T}$ region [12]. This is considered as a strong evidence of the existence of a medium effect of QGP. Also the jet quenching effect can be observed via the azimuthal correlation of high-$p_{\rm T}$ particles. If the deconfinement state is produced in relativistic heavy-ion collisions, observed jets predominantly produced near the surface and directed outward. In case one of jets traversing the dense core loose its energy, resulting in the suppression of back-to-back high-$p_{\rm T}$ pairs, while near side pairs are not suppressed and similar to those of $p + p$ collisions. Recently, the STAR experiment have reported a signature of jet quenching by comparing two-particle azimuthal distributions of inclusive charged hadrons at high-p_T between $Au + Au$, $p + p$ and $d + Au$ collisions [13].

The measurement of J/ψ is also believed to be one of the major signatures of the presence of QGP since Matsui and Satz predicted the suppression of J/ψ yield in the QGP formation in heavy-ion collisions [10]. Because the J/ψ, which is a bound state of $c\bar{c}$ pair, is formed in a hard scattering process at the very early stage of heavy-ion collisions, then it would be melt through color screening in the QGP state, commonly referred to as Debye screening [10]. The deconfined c and $\bar{c}$ are mostly coupled with the other quarks, then observed as charmed bosons such as D and $\bar{D}$. Recently, a clear observation of J/ψ suppression has been reported by NA50 experiment at SPS [11].

1.2.2 Temperature of hot and dense matter

The measurements of transverse momentum p_T and energy E_T spectra of single particles provide the temperature of the medium by fitting the spectra the slopes with a Boltzmann distribution if the medium is assumed to be in thermal equilibrium state [3, 4]. The so-called "thermal" photons and dileptons (i.e. virtual photons) which are directly emitted from the early stage of a collision would not be disturbed by the final state interactions, and carry information on the temperature of the hot and dense matter at the moment of their production.

The thermal photons from the thermalized QGP state are created by annihilation ($q + g \rightarrow q + \gamma$) and Compton scattering ($q + \bar{q} \rightarrow g + \gamma$) processes, and those photons are expected to be visible at the momentum range $2< p_\mathrm{T} <5$ GeV/c. At lower p_T region, background photons which are originated from electro-magnetic decays, such as π^0 and η, would significantly exceed the yield of the thermal photons from the QGP, and those photons would represent the temperature of the medium after the mixed phase. At very high p_T region, the yield of "hard" photons, which are originated from the single-parton scatterings and the Drell-Yan process at the very early stage of the collision, probably become dominant.

Also thermal dileptons, which are originated from virtual photons created in the same stage as the thermal photons, may carry information on the temperature of the hot and dense matter. The transverse mass spectrum of dilepton pairs in a window of its invariant mass around 1−2 GeV is expected to be most visible for the temperature of the QGP state. Background dileptons originate from pion annihilation, resonance decays and $\pi - \rho$ interaction become dominant at lower mass region, and dileptons from Drell-Yan processes exceeds the yield of thermal dileptons at higher mass region.

1.2.3 Chiral symmetry

When the deconfinement state is formed, chiral symmetry, which is always broken at lower temperature, is expected to be restored [14]. According to lattice QCD calculations, the deconfinement and the chiral symmetry restoration occur at the same critical temperature T_c. The chiral symmetry restoration results in the modification of hadronic property, and observed as decrease of effective mass (mass shift) or mass width of light vector mesons [16]. Experimentally, the measurement of enhancement of dileptons at low invariant mass region decayed from ρ meson is suggested to be one of useful tools to observe the chiral symmetry restoration, because ρ meson is a short-lived resonance and dileptons decayed from the ρ meson are not subjected to the strong final-state interactions. The CERES/NA45 experiment has measured the inclusive e^+e^- invariant-mass distribution, and reported the enhancement of e^+e^- pairs at low mass region comparing to the sum of the expected contributions from hadron decays [15].

1.2.4 Dynamics

The measurement of the space-time evolution of the hot and dense matter is an essential and a very important tool to comprehensively understand what happens in the relativistic heavy-ion collisions.

The dynamics of the system expansion is very sensitive to the pressure gradient at the initial stage of collisions, which is fully governed by the collision anisotropy. In non-central collisions, the overlap region of two colliding nuclei form an ellipsoid shape. If the QGP is formed at the very early stage of collisions in about 1 fm/c, the strong interactions would be sufficient to establish local equilibrium keeping the medium in the ellipsoid shape, resulting in a rapid pressure gradient in the short direction. This anisotropic pressure gradient produces the higher transverse momentum of hadrons emitted from the final stage in the short direction than those in the long direction, aka elliptic flow. Thus, the measurement of elliptic flow is recognized as a very important tool to investigate whether the local equilibrium due to the QGP is created in the early stage of heavy-ion collision [7]. Recently, the PHENIX and STAR experiments have presented the detailed studies of charged hadron spectra [5, 6] and elliptic flow [8, 9] at $\sqrt{s_{\mathrm{NN}}} = 200$ GeV in Au+Au collisions.

In the hadronic phase, the system is considered to expands with a finite collective flow velocity β_{T}, decreasing its temperature (energy density) until its kinetic freeze-out temperature T_f. These β_{T} and T_f are observable values through single particle spectra of hadrons, such as pion, kaon and proton, assuming the Boltzmann distribution. The measurement of Bose-Einstein correlation of an identical two-particle, aka HBT, provides the extent of the system (HBT radius) and the emission duration of particles at the freeze-out stage. In addition, the HBT measurement can be used to extract the β_{T} and T_f parameters from the pair momentum dependence of HBT radius. (Refer to the next chapter and references therein for the detailed description.)

1.3 Motivation of this study

Although some of experimental data at SPS and RHIC show some hints at an existence of the QGP state, we still have no clear insight in what happens in the system, e.g. the space-time extents of the deconfinement state and hadron gas. As described in the previous section, single particle spectrum, Bose-Einstein correlation and elliptic flow are key observable signals to investigate the space-time evolution of system, and to understand a comprehensive picture of the dynamics of expanding system from the formation of the deconfined state to hadron gas. If a hydrodynamics model will be able to reproduce those experimental signals simultaneously, we could explicitly define some macroscopic parameters of the system such as chemical freeze-out temperature T_{ch}, hadron freeze-out temperature T_f and collective flow velocity β_f, which are important values to understand its dynamics. The successful reproduction also validates the present of the deconfinement state, because the transition of equation of state is usually assumed in hydrodynamics models.

In this study, I present the measurement of Bose-Einstein correlations of like-sign pions in Au+Au collisions at $\sqrt{s_{\rm NN}} = 200$ GeV and provide the extents of produced source radius and the emission duration of particles. For this analysis, I utilize about 50 million minimum biased events taken by PHENIX detector for the second year's running at RHIC. The organization of this thesis is as follows:

In Chapter 2, the analytical method of the Bose-Einstein correlation function is explained in detail. The Bertsch-Pratt parameterization to extract multi-dimensional HBT radii is described. Also a puzzle in the measurements of the HBT radii, which has recently arisen, is briefly introduced here.

In Chapter 3, the RHIC accelerator and the experimental setup of the PHENIX detector are introduced. In particular, subsystems, which are utilized to identify charged pions for this analysis, are explained in detail.

In Chapter 4, data reduction procedure from the track reconstruction to the particle identification, is described. Also a method for identical pair assemble and corrections for two-track detection inefficiency by Monte-Carlo simulation are explained.

In Chapter 5, I focus on a new technique of the Coulomb final-state interaction correction, which is well improved from a traditional Coulomb correction used in earlier HBT analyses. For the justification of the new Coulomb correction, I also measure the two-particle correlation for unlike-sign pion pairs. In addition, studies of systematic errors are given.

In Chapter 6, 1-dimensional and 3-dimensional $\pi^+\pi^+$ and $\pi^-\pi^-$ correlation functions and resulting HBT radii are presented. To study the space-time evolution of the system, the HBT radii are measured as a function of the mean transverse momentum of pair (k_{T}) and collision centrality. Theoretical interpretations of the k_{T} dependence of the HBT radii are explained. Fits of the theoretical models provide the geometrical source size and life time of the system. These results are compared to those from earlier experimental analyses at lower energies. Also the k_{T} dependence of experimental HBT radii are compared to those of theoretical predictions from recent hydrodynamics models.

Finally, I give the conclusion of this analysis in Chapter 7.

Chapter 2

Bose-Einstein correlation

2.1 Overview

In the early 1950's, Hanbury Brown and Richard Twiss invented the technique to measure the angular diameter of stars by using intensity correlation between two photons [17]. Thus, two-particle interferometry is called as "Hanbury-Brown and Twiss" or "HBT" effect after the names of pioneers. In the field of particle physics, the HBT effect was independently discovered by G. Goldhaber, S. Goldhaber, W. Lee and A. Pais who measured the angular correlations between identical pions and extracted the extent of a source in proton-antiproton collisions at Bevatron [19]. In this case the HBT effect differs from ordinary amplitude interferometry, but which effect originates from quantum statistical effects resulting from the symmetrization of the wave function of bosons, or anti-symmetrization for fermions. The so-called "Bose-Einstein" correlation for identical boson (fermion) pairs results in the enhancement (suppression) of the two-particle coincidence rate at small relative momentum of the pair. A striking point of the measurement of the Bose-Einstein correlation is that it could provide not only the extent of the source but also the emission duration of particles using a three-dimensional analysis.

As described in the previous chapter, one possible signature from the formation of the QGP state is predicted to be the existence of a long mixed phase due to the softening of the equation-of-state in a first-order phase transition, resulting in the long emission duration of particles [18]. That's why the Bose-Einstein correlations for identical particles have widely been measured in the field of high-energy heavy-ion experiments [23, 24, 25, 26, 27, 35, 28, 29]. Moreover, the Bose-Einstein correlation analyses have been served as an important tool to measure the source profile, such as the thermal freeze-out temperature T_f, the corrective flow velocity β_f at the hadronic freeze-out of source, in conjunction with information from the measurements of single particle spectra and elliptic flow. In SPS-RHIC energies, much of efforts in Bose-Einstein correlation analyses have gone into the extraction of such characterization parameters of dynamical source because it is closely related to the property of the antecedent phase of hot and dense matter.

2.2 Two particle correlation function

The two-particle correlation function is defined by the ratio of the two particle coincidence probability density over the product of the two single particle probabilities as

$$C_2 = \frac{P(\mathbf{p}_1, \mathbf{p}_2)}{P(\mathbf{p}_1)P(\mathbf{p}_2)}, \tag{2.1}$$

where $\mathbf{p}_1$ and $\mathbf{p}_2$ denote 4-vector momenta of observed identical particles. To explain how the Bose-Einstein correlation term works in Eq. 2.1, we consider a simple model which can be described in plane wave. As shown in Fig. 2.1, identical particle 1 and 2 which have 4-momenta $\mathbf{p}_1$ and $\mathbf{p}_2$ respectively are emitted from the space-time points r_1 and r_2 in a source with the separation of R. After traveling the distance of L, they are observed by detectors located at x_1 and x_2. Since we can not distinguish the emitted points of two identical particles in the case of $R << L$, we have to consider two possible trajectories as shown by solid and dashed lines. If we assume the particles are emitted independently ("chaotic source"), the probability amplitude of detecting two identical particle is given as

$$\begin{aligned}\psi_{12} = \frac{1}{\sqrt{2}}\{&A(p_1, x_1)A(p_2, x_2)e^{-ip_1(x_1-r_1)}e^{-ip_2(x_2-r_2)} \\ &\pm A(p_1, x_2)A(p_2, x_1)e^{-ip_1(x_2-r_1)}e^{-ip_2(x_1-r_2)}\}\end{aligned} \tag{2.2}$$

where + (upper) sign stands for bosons, − (lower) sign for fermions. $A(p, x)$ is the amplitude of a particle which is emitted by a point x with momentum p, and $e^{-ip(x-r)}$

is the propagation of the particle. The corresponding probability density of two-particle momentum is obtained by an integral of the source according to the distribution function $\rho(r)$ as

$$\begin{aligned} P(p_1,p_2) &= \int d^4r_1 d^4r_2 \rho(r_1)\rho(r_2)|\psi_{12}|^2. \\ &= \frac{1}{2}\int d^4r_1 d^4r_2 \rho(r_1)\rho(r_2)\Big\{A^2(p_1,x_1)A^2(p_2,x_2) + A^2(p_1,x_2)A^2(p_2,x_1) \\ &+ A(p_1,x_1)A(p_2,x_2)A(p_1,x_2)A(p_2,x_1)e^{ir_1(p_1-p_2)}e^{-ir_2(p_1-p_2)} \\ &+ A(p_1,x_1)A(p_2,x_2)A(p_1,x_2)A(p_2,x_1)e^{-ir_1(p_1-p_2)}e^{ir_2(p_1-p_2)}\Big\} \end{aligned} \tag{2.3}$$

After r_1 and r_2 in the second to fourth terms are renamed, this equation is further rewritten as

$$\begin{aligned} P(p_1,p_2) &= \int d^4r_1 d^4r_2 \rho(r_1)\rho(r_2)A^2(p_1,x_1)A^2(p_2,x_2) \\ &+ \left| \int d^4r \rho(r)A(p_1,r)A(p_2,r)e^{-ir(p_1-p_2)} \right|^2 . \end{aligned} \tag{2.4}$$

In the case of the detection single particle, the probability amplitude is expressed as

$$\psi_1 = A(p,x)e^{-ip(x-r)}, \tag{2.5}$$

and the probability density is described as

$$P(p) = \int d^4r \rho(r)|\psi_1|^2 = \int d^4r \rho(r) A^2(p,x). \tag{2.6}$$

From Eq. 2.1-2.6, the two-particle correlation function can be described as

$$C_2 = \frac{P(\mathbf{p}_1,\mathbf{p}_2)}{P(\mathbf{p}_1)P(\mathbf{p}_2)} = 1 + \frac{\left| \int d^4r\rho(r)A(p_1,r)A(p_2,r)e^{-ir\mathbf{q}} \right|^2}{\int d^4r_1\rho(r_1)A^2(p_1,x_1)d^4r_2\rho(r_2)A^2(p_2,x_2)} \tag{2.7}$$

where $\mathbf{q}$ is the relative difference of 4-vector momentum of pair, $p_1 - p_2$. Here, we assume a Gaussian distribution for the source density as

$$\rho(r) = \frac{1}{4\pi^2R^4}\exp\left(-\frac{r^2}{2R^2}\right) \tag{2.8}$$

where R is the standard deviation (the Gaussian width). Using the Gaussian parameterization, the correlation function of Eq. 2.7 can be rewritten by using the Fourier transform of $\rho(r)$ as

$$C_2 = 1 + \exp(-R^2\mathbf{q}^2). \tag{2.9}$$

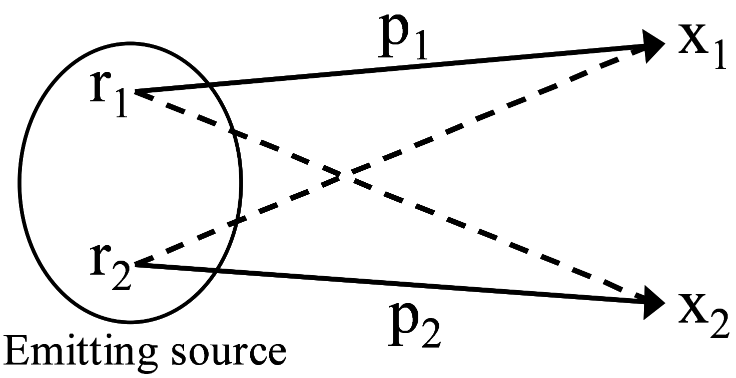

Figure 2.1: The general scheme of identical particle correlation in particle physics.

This equation is valid only for the fully "chaotic" source. However, experimentally observed correlation function is further suppressed due to several effects such as the partial coherence of the source and pairs come from the resonance decays. For the more realistic "non-chaotic" source, Eq. 2.9 is modified as

$$C_2 = 1 + \lambda \exp(-R^2\mathbf{q}^2), \tag{2.10}$$

where λ is commonly referred to as "chaoticity parameter", which is from 0 to 1.

In the one-dimensional Bose-Einstein correlation analysis, the correlation function is measured as a function of a Lorentz-invariant relative momentum q_{inv}:

$$\begin{aligned} C_2(q_{\mathrm{inv}}) &= 1 + \lambda_{\mathrm{inv}} \exp(-{R_{\mathrm{inv}}}^2 {q_{\mathrm{inv}}}^2), & (2.11)\\ \text{with} \quad q_{\mathrm{inv}} &= \sqrt{q_{\mathrm{x}}^2 + q_{\mathrm{y}}^2 + q_{\mathrm{z}}^2 - q_0^2} & (2.12) \end{aligned}$$

where R_{inv} is the 1-dimensional HBT radius, which is related to its spatial and temporal sizes as described in section 2.4.1, and λ_{inv} is the 1-dimensional chaoticity parameter. $(q_{\mathrm{x}}, q_{\mathrm{y}}, q_{\mathrm{z}})$ is the relative difference of measured momentum for each direction and q_0 is relative energy difference of pairs ($\mathbf{q}_0 = E_1 - E_2$). In this analysis, the particle energy is determined by measured momentum p and the ideal mass as $E = \sqrt{p^2 + m_{ideal}^2}$. The schematic correlation function as a function of q_{inv} is illustrated in Fig. 2.2.

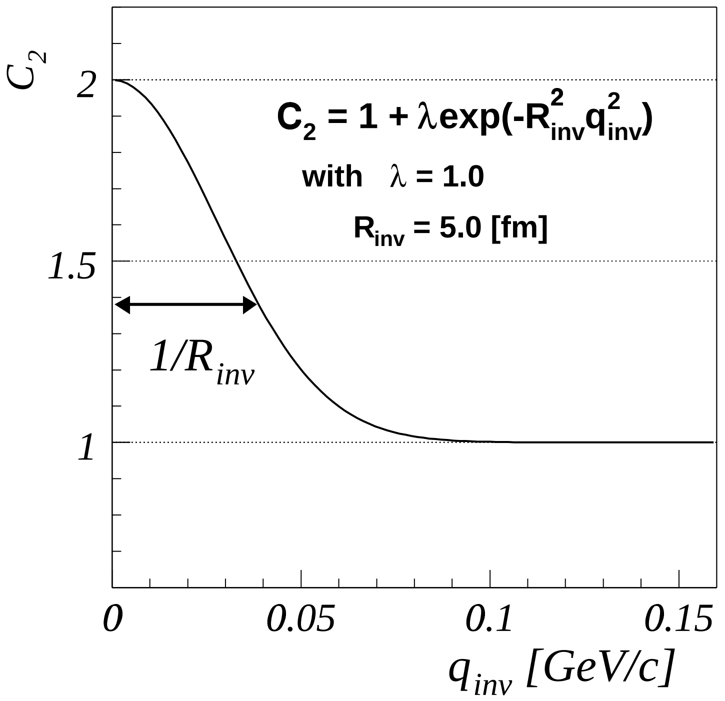

Figure 2.2: One-dimensional correlation function as a function of q_{inv} with input parameters, $\lambda_{\text{inv}} = 1.0$ and $R_{\text{inv}} = 5.0$ fm.

2.3 Two external parameters

2.3.1 Centrality dependence

Since a HBT radius represent the RMS-width of the geometrical source size at the hadronic freeze-out stage assuming a static source, it could depend on the centrality of the collision, namely the overlap region at the initial collision. It is interesting to investigate the correlation between the initial overlap region and the HBT radius in terms of the following questions:

- How the HBT radius scale to the initial overlap region?
- How many times does the overlap region increase during its evolution from the initial to final stage?

- If the QGP could be formed at a certain centrality of the nucleus-nucleus collision and the overlap region is significantly enlarged due to the first-order phase transition, which centrality it would take place at?

To investigate these dependencies, the HBT radius parameters are measured as a function the number of participants, N_{part}. The N_{part} means the number of nucleons participated in the overlap region of nucleus-nucleus collisions, namely $N_{\text{part}} = 2$ in p+p collision and $N_{\text{part}} = 394$ in Au+Au at the most central collision.

2.3.2 k_T dependence

So far I have discussed the particular case in which the source is static at its kinetic freeze-out. However, a realistic source in high-energy heavy-ion collisions is considered to expand with a finite collective flow (β_f) at the hadronic state. In such a dynamically expanding source, the particle momenta are strongly correlated with their emission points, that is commonly referred to as "space-momentum correlation" [22]. For example, particles emitted from around the surface of the expanding source tend to have larger momenta than those emitted from the center of it. The HBT radius size shrinks as the collective flow velocity increases because the correlation function measures only some partial source size through a filter of the wavelength of pair momenta, called "lengths of homogeneity". To study the space-time evolution of the source, the averaged transverse momentum of pair k_{T} is usually introduced as an independent external parameter.

The k_{T} dependence of HBT radii (Bertsch-Pratt radius parameters) have been measured by earlier experiments at $\sqrt{s_{\text{NN}}}$ ~4-5 GeV in Au+Au collisions [24, 25] at AGS, $\sqrt{s_{\text{NN}}}$ ~17 GeV in Pb+Pb collisions at SPS [26, 27], and PHENIX and STAR have recently reported the k_{T} dependence of HBT radii in Au+Au collisions at $\sqrt{s_{\text{NN}}} = 130$ GeV at RHIC [28, 29]. The top panel of Fig. 2.4 shows the k_{T} dependence of the HBT radius parameter in transverse direction at $\sqrt{s_{\text{NN}}} = 130$ GeV. These experimental results show that the transverse HBT radius apparently decreases as k_{T} increases, indicating a radially expanding source.

2.4 Bertsch-Pratt parameterization

2.4.1 HBT radius parameters

One of the advantages of the Bose-Einstein correlation measurement in relativistic heavy-ion collisions is that the measurement of multi-dimensional correlation function can provide not only the spatial size but also the temporal size of source. The Bertsch-Pratt parameterization [20, 21] has been widely employed to analyze multi-dimensional HBT radii in earlier Bose-Einstein correlation analyses. The schematic diagram of the parameterization is illustrated in Fig. 2.3. In the parameterization, the relative momentum of pair $\mathbf{q}$ is decomposed into the transverse direction q_{T}, which is perpendicular to the beam-axis, and the longitudinal direction q_{long}, which is parallel to the beam-axis (i.e. $q_{\mathrm{long}} = q_{\mathrm{z}}$), as shown by the left diagram in Fig. 2.3. Then, as shown in the right diagram, q_{T} can be decomposed into the outward direction q_{out}, which is parallel to the averaged transverse momentum of the pair, $k_{\mathrm{T}} = (p_{\mathrm{T1}} + p_{\mathrm{T2}})/2$ where p_{Ti} is the transverse momentum of each particle of the pair, and the sideward direction q_{side}, which is perpendicular to k_{T}. Using the Bertsch-Pratt parameterization, we can rewrite the correlation function as a function of 4-vector momentum as

$$\begin{aligned} C_2 &= 1 + \lambda \exp(-\mathbf{R}^2\mathbf{q}^2) \\ &= 1 + \lambda \exp(-R_{\mathrm{x}}^2 q_{\mathrm{x}}^2 - R_{\mathrm{y}}^2 q_{\mathrm{y}}^2 - R_{\mathrm{z}}^2 q_{\mathrm{z}}^2 - \sigma_{\mathrm{t}}^2 q_0^2) \\ &= 1 + \lambda \exp(-{R_{\mathrm{side}}}^2 {q_{\mathrm{side}}}^2 - {R_{\mathrm{out}}}^{*2} {q_{\mathrm{out}}}^2 - {R_{\mathrm{long}}}^2 {q_{\mathrm{long}}}^2 - \sigma_{\mathrm{t}}^2 q_0^2). \end{aligned} \tag{2.13}$$

Fitted R_{side}, ${R_{\mathrm{out}}}^*$ and R_{long} parameters, which are commonly referred to as "HBT radii", equal to the Gaussian widths of source size in q_{side}, q_{out} and q_{long} directions, not its hard sphere radius value. σ_{t} is a temporal term, which corresponds to the Gaussian width of the duration of particle emission. Assuming the longitudinal center-of-mass system (LCMS) defined as $p_{\mathrm{z1}} + p_{\mathrm{z2}} = 0$, the energy difference q_0 in Eq. 2.13 can be rewritten as

$$q_0 = E_1 - E_2 = \frac{p_1 + p_2}{E_1 + E_2}(p_1 - p_2) = \beta_{12} q_{12} \overset{LCMS}{\approx} \beta_{\mathrm{T}} q_{\mathrm{out}}, \tag{2.14}$$

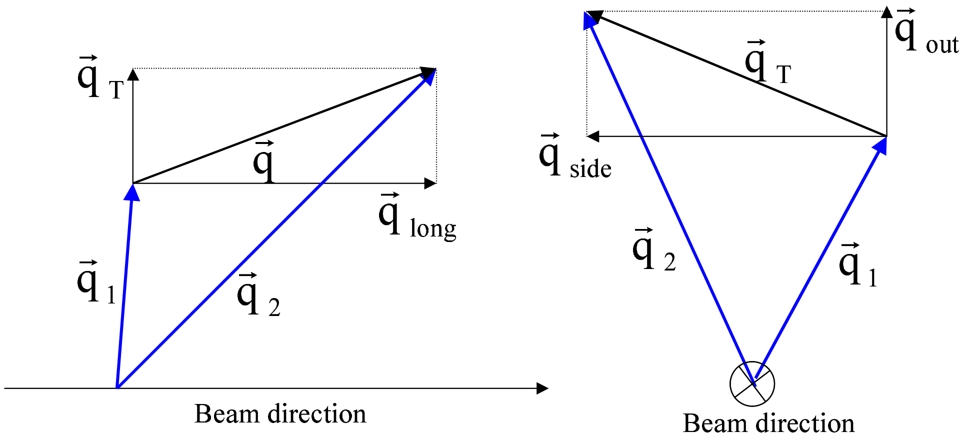

Figure 2.3: The general schematic diagrams of Bertsch-Pratt parameterization.

where β_{T} corresponds to the transverse velocity of the pair. From Eq. 2.13 and Eq. 2.14, the correlation function is reduced to a three-dimensional form as

$$\begin{aligned} C_2 &= 1 + \lambda \exp(-R_{\mathrm{side}}{}^2 q_{\mathrm{side}}{}^2 - (R_{\mathrm{out}}{}^{*2} + \beta_{\mathrm{T}} \sigma_{\mathrm{t}}^2) q_{\mathrm{out}}{}^2 - R_{\mathrm{long}}{}^2 q_{\mathrm{long}}{}^2) \\ &= 1 + \lambda \exp(-R_{\mathrm{side}}{}^2 q_{\mathrm{side}}{}^2 - R_{\mathrm{out}}{}^2 q_{\mathrm{out}}{}^2 - R_{\mathrm{long}}{}^2 q_{\mathrm{long}}{}^2). \end{aligned} \tag{2.15}$$

The fit parameter R_{out} consists of the transverse source size and the emission duration of particles. Here, if we assume a cylindrically symmetric ($R_{\mathrm{side}} = R_{\mathrm{out}}{}^*$) and static source which has a constant source size, the duration of particle emission can be observed as

$$\sigma_{\mathrm{t}} = \sqrt{R_{\mathrm{out}}{}^2 - R_{\mathrm{side}}{}^2} / \beta_{\mathrm{T}}. \tag{2.16}$$

In the Bertsch-Pratt parameterization described above, the cross-term between outward and longitudinal direction, $-2R_{\mathrm{ol}}^2 q_{\mathrm{out}}{}^2 q_{\mathrm{long}}{}^2$, is eliminated because the source is approximately symmetric about the $z = 0$ plane.

2.4.2 RHIC-HBT puzzle

In the case of static source, its emission duration of particles is evaluated by Eq. 2.16. In the realistic source in heavy-ion collisions, however, the source is considered to dynamically expands. In case, the HBT radii are parameterized in more sophisticated forms due to the effect of its corrective expansion. For the simplification, the ratio of R_{out} to R_{side} (i.e. $R_{\mathrm{out}}/R_{\mathrm{side}}$) is measured in several earlier Bose-Einstein correlation analyses to investigate the extent of a finite duration of particle emission. If the source is transparent and has a finite emission duration, the $R_{\mathrm{out}}/R_{\mathrm{side}}$ ratio could become larger than unity.

The lower panel of Fig 2.4 shows the $R_{\mathrm{out}}/R_{\mathrm{side}}$ ratios measured by PHENIX and STAR in Au+Au collisions at $\sqrt{s_{\mathrm{NN}}} = 130$ GeV from k_{T} ∼0.2 GeV/c to k_{T} ∼0.6 GeV/c. The experimental $R_{\mathrm{out}}/R_{\mathrm{side}}$ ratios are equal to or less than unity within the errors, and show a trend that the ratio slightly decreases as k_{T} increases. The $R_{\mathrm{out}}/R_{\mathrm{side}}$ ratios from recent calculations for a thermalized source with a first-order phase transition at different critical temperatures ($T_c = 160$ and 200 MeV) [30] are also given as a function of k_{T} in the figure. The ratios increase as k_{T} increases due to the hadron re-scattering at high-k_{T} region, and are between about 1.5 and 2.2 for $0.2 < k_{\mathrm{T}} < 0.6$ GeV/c. The large discrepancy between experimental and theoretical HBT radii, called "RHIC-HBT puzzle" [31], has two essences. One is a naive question that the $R_{\mathrm{out}}/R_{\mathrm{side}}$ ratio should be larger than unity. Another is the question that recent theoretical calculations are able to well reproduce single particle spectra and many-particle correlations that give rise to elliptic flow, but failed to reproduce the experimental HBT radii, especially such $R_{\mathrm{out}}/R_{\mathrm{side}} < 1$ value. Thus, the RHIC-HBT puzzle is one of the key issues on results obtained in the RHIC program.

In this analysis, I focus on further detailed centrality and k_{T} dependences of 1-dimensional and 3-dimensional (Bertsch-Pratt) HBT radii by using an abundant statistics of data which was taken in the PHENIX Year-2 running. Model fits to the experimental HBT radii as a function of k_{T} provide the information of dynamical source, such as the geometrical source size and the life time. The comparison of HBT radii for such a wide k_{T} range between the detailed measurements and recent theoretical calculations based on hydrodynamical models, could provide a strong constraints for model builders to solve the RHIC-HBT puzzle. In addition, the HBT radii are measured as a function of collision centrality in detail to investigate a relation between geometrical source sizes and the HBT radii.

I also focus on the recently developed Coulomb correction method which is suggested by Sinyukov [33] based upon a picture of core-halo structure of source [34]. In the core-halo model, a source produced in the relativistic heavy-ion collision is considered to be a superposition of a central core surrounded by an extended halo. I present the comparison of resultant HBT radii extracted with the new Coulomb correction method and the conventional *full* Coulomb correction most earlier analyses have used so far, then discuss the RHIC-HBT puzzle in terms of the Coulomb correction method.

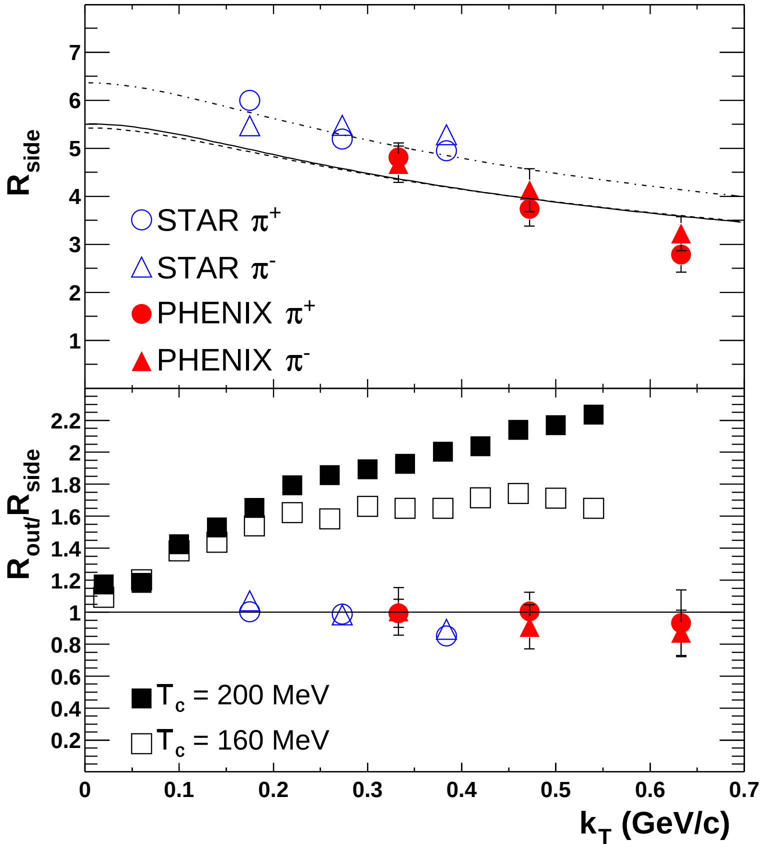

Figure 2.4: The top panel shows R_{side} for identical pions measured by STAR [28] and PHENIX [29]. The solid line is a fit of Eq. 6.8 to the PHENIX data. The dot-dashed line is tha same fit to the STAR data. The bottom panel shows the ratio $R_{\text{out}}/R_{\text{side}}$ as a function of k_T overlaid with theoretical predictions for a phase transition for two critical temperatures [30].

Chapter 3

Experimental Setup

3.1 The RHIC accelerator

The Relativistic Heavy Ion Collider (RHIC) at Brookhaven National Laboratory has a capability to accelerate and collide two types of particle species, e.g. gold-gold (Au+Au), deuteron-gold (d+Au) and polarized proton-proton (p+p) collisions [36]. A schematic diagram of the RHIC facility is shown by Fig. 3.1. In Au+Au collisions, bunches of Au-ions are provided from the Tandem Van de Graaff and accelerated up to 1 A MeV, then injected into the Booster Synchrotron to accelerated up to 192 A MeV, and then injected in the Alternating Gradient Synchrotron (AGS) ring. The AGS accelerator, which has been used for many fixed target experiments in heavy-ion collisions at the center of mass energies from 2.5 to 4.5 GeV, is used as a pre-accelerator for the RHIC ring. The bunches of Au-ions, accelerated up to 10.8 GeV by the AGS ring, are send to the AGS-To-RHIC transfer line, where a switching magnet sends the ion bunches down one of two beam lines. The two Au beams are injected into the right and left rings of RHIC, labelled yellow and blue ring, respectively. Each ring is composed of six arc sections and six insertion sections with a collision point. The injected two Au beams are accelerated by using dipoles and quadrupoles in each arc section and a pulse of radio waves up to 100 GeV/nucleon ($\gamma = 100$) in the RHIC ring, and collide at six beam interaction points. In Au+Au collisions at $\sqrt{s_{\rm NN}} = 100$ GeV, the number of bunches per ring is 56 and each bunch consists of $\sim 1\times10^{9}$ Au-ions, providing a luminosity of $\sim 2\times10^{26}$ cm^{-2}s^{-1}. Fig. 3.2 shows a diagram

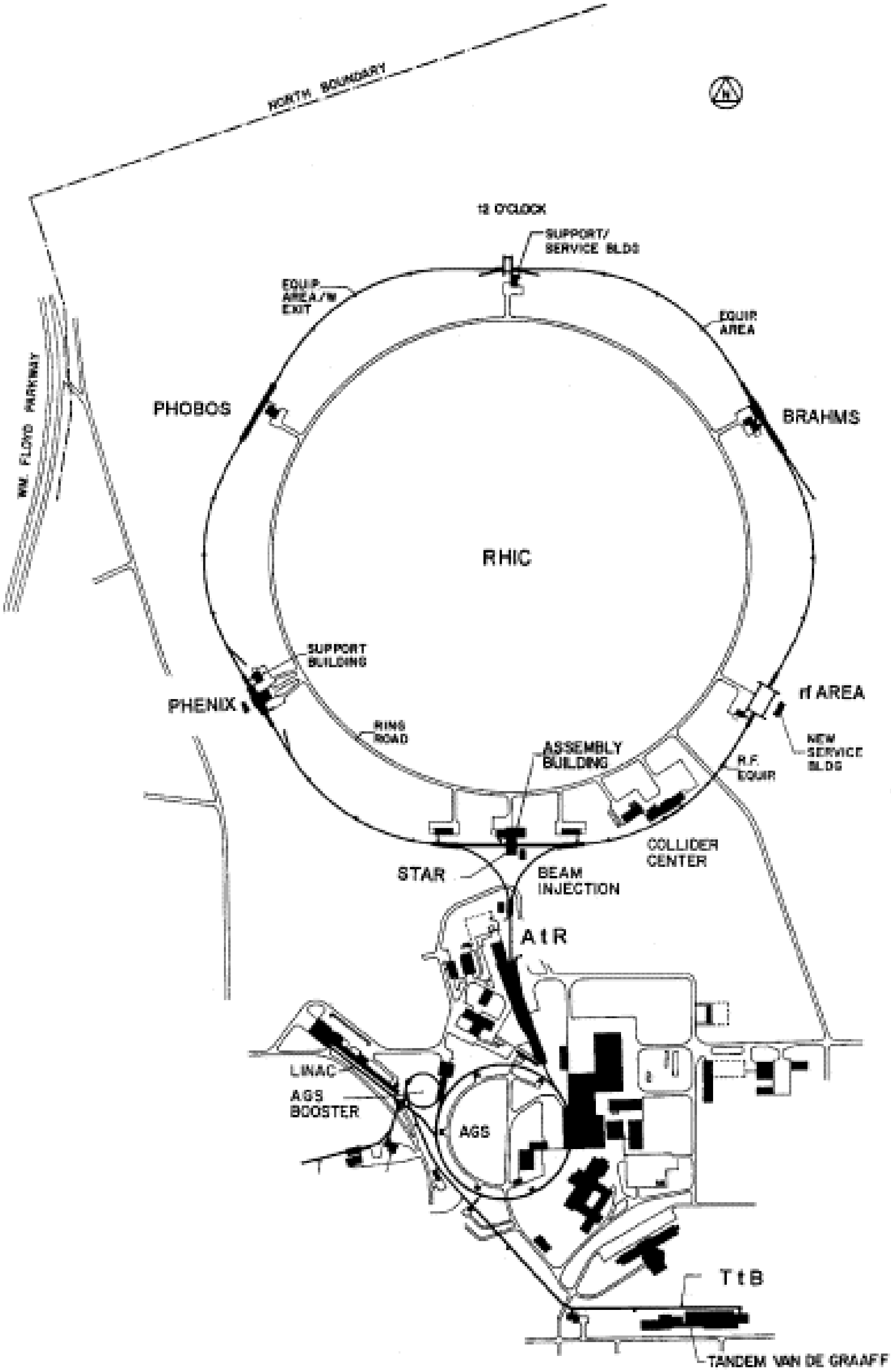

Figure 3.1: A schematic diagram of the AGS and RHIC facilities.

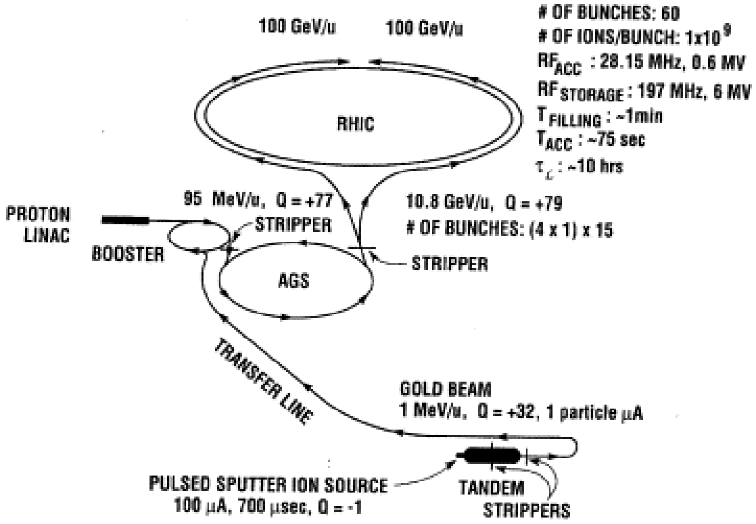

Figure 3.2: Au beam acceleration at the RHIC facility.

of Au-beam acceleration with the operating parameters.

In polarized p+p collisions, polarized proton beam is provided by the LINAC to the Booster Synchrotron and injected into AGS ring, and then injected into the two RHIC rings. The polarization of proton beams during being accelerated is maintained by Siberian Snake magnets in the AGS and RHIC rings. The Siberian Snake is constructed from four 2 m helical dipole modules, which provides a full 180° spin flip. The RHIC and Siberian Snakes are designed to accelerate the polarized proton up to 500 GeV with 70% polarization.

Four experiments are located at four of the six interaction points, i.e. PHENIX, STAR, PHOBOS and BRAHMS as shown by Fig. 3.1. Among the four experiments, PHENIX and STAR are largest detectors that are composed of lots of subsystems, designed to measure many particle species for their large acceptances, and able to study some observable signals simultaneously. On the other hand, PHOBOS and BRAHMS are designed to study a few specific topics in detail, and are smaller detectors than PHENIX and STAR.

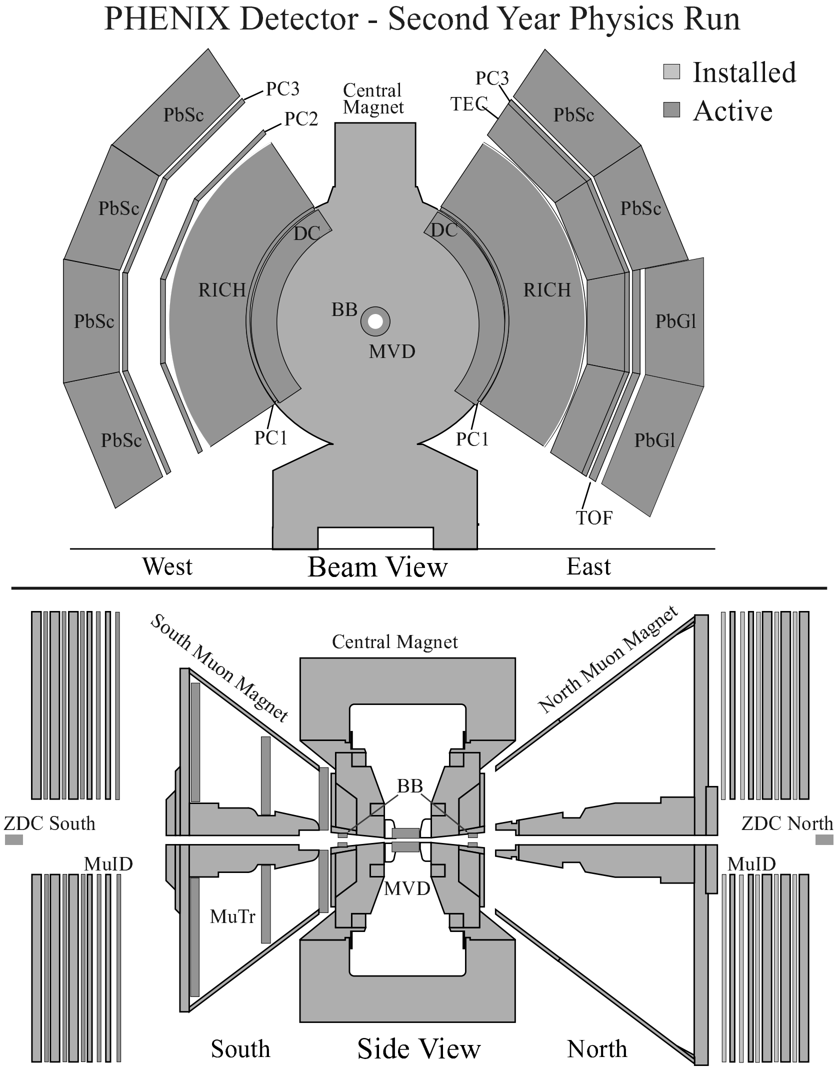

Figure 3.3: Schematic drawings of the PHENIX detector setup for Year-2 running, viewed in a cut through the collision vertex (top figure), parallel to the beam axis (bottom figure).

Subsystem	$\Delta\eta$	$\Delta\phi$ (rad)	Purposes
CM	± 0.35	2π	0.78 T·m for $\eta = 0$
MM (south)	-2.2 to -1.1	2π	0.72 T·m for $\eta = 2$
(north)	1.1 to 2.4	2π	
BBC	$\pm(3.1 - 3.9)$	2π	vertex position, start timing, LVL1-trigger.
ZDC	$\lvert\eta\rvert > 6$	2π	vertex position, LVL1-trigger.
MVD	± 2.6 mrad	2π	multiplicity ($d^2N/d\eta d\phi$).
DCH	± 0.35	$\pi/2 \times 2$	Charged particle tracking.
PC(1,2,3)	± 0.35	$\pi/2 \times 2$	Pattern recognition, tracking for non-magnetic field running.
TOF	± 0.35	$\pi/4$	Charged hadrons, $\pi/K/p$ separation.
RICH	± 0.35	$\pi/2 \times 2$	Electron detection, π/e separation.
EMCal (PbSc)	± 0.35	$\pi/2 + \pi/4$	Photon, electron, hadron detection.
EMCal (PbGl)	± 0.35	$\pi/4$	Photon, electron detection.
MuTr (south)	-2.25 to -1.15	$\pi/2$	Muon tracking.
(north)	1.15 to 2.44	$\pi/2$	
MuID (south)	-2.25 to -1.15	$\pi/2$	Muon detection, μ/π separation.
(north)	1.15 to 2.44	$\pi/2$	

Table 3.1: Summary of acceptances and purposes of the PHENIX subsystems.

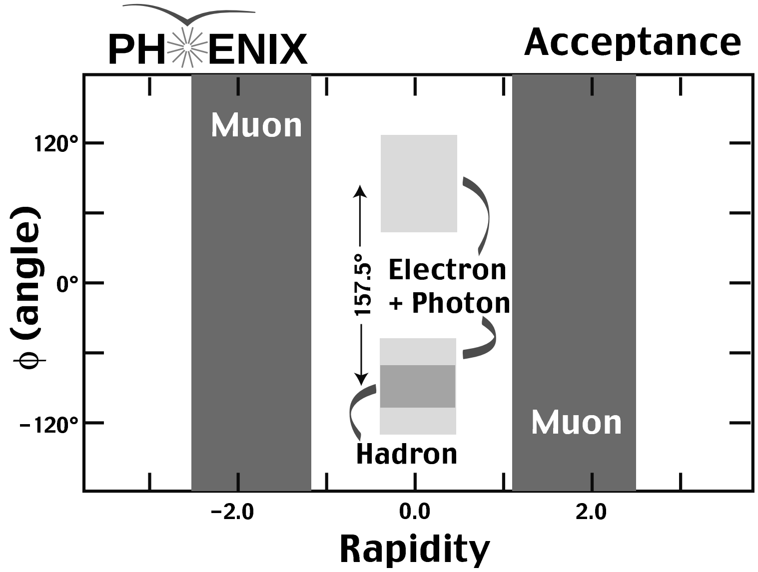

Figure 3.4: A schematic drawing of the PHENIX acceptance for leptons and hadrons in the pseudorapidity η versus azimuthal angle ϕ.

3.2 The PHENIX detector

The Pioneering High Energy Nuclear Interaction eXperiment (PHENIX) detector, located at one of the six interaction points at RHIC, is composed of global detectors for the characterization of collision events and the triggering of the data acquisition, two mid-rapidity spectrometer arms (the Central arms) and two forward spectrometer arms (the Muon arms) for the tracking and identification of particles, as shown by schematic drawings in Fig. 3.3. The purpose of the PHENIX is to provide powerful particle identification (PID) capabilities for hadrons, leptons and photons over a wide momentum range. The acceptance for these particle species is illustrated in Fig. 3.4.

3.2.1 The global detectors

The global detectors consist of the Zero-Degree Calorimeters (ZDC), the Beam-Beam Counters (BBC) and the Multiplicity Vertex Detector (MVD). A pair of ZDCs, which are located at 18.25 meters upstream and downstream of the beam crossing point, are designed to measure spectator neutrons that escape from a collision, namely free neutrons which do not participate in the collision and also not coalesce with other spectator protons. The ZDCs are able to determine a collision position along the beam axis, called as “vertex position”. A pair of BBCs, which surround the beam-pipe at 1.5 meters upstream and downstream of the beam crossing point, are designed to measure forward particles produced in a collision. The prior purpose of BBCs is to determine the vertex position and the start time of a collision.

At PHENIX, the event centrality is determined from the correlation between charge sum deposited in BBCs and energy sum deposited in ZDCs, as shown by Fig.3.5. The BBC charge sum monotonically decreases as the collision centrality decreases, while the ZDC energy sum increases as the centrality decreases due to the increases of the number of spectator neutrons. In more peripheral collisions, however, spectator neutrons tend to be bound in a deuteron or a heavier fragment, and a bigger fraction of the spectator neutrons is removed from the ZDC acceptance by magnets in front of ZDCs. Therefore, the energy deposited in ZDCs decreases in the peripheral collisions, resulting in such a boomerang shaped correlation, as shown by Fig.3.5. In this plot, the distribution is divided into centrality classes by the solid lines from a fixed point.

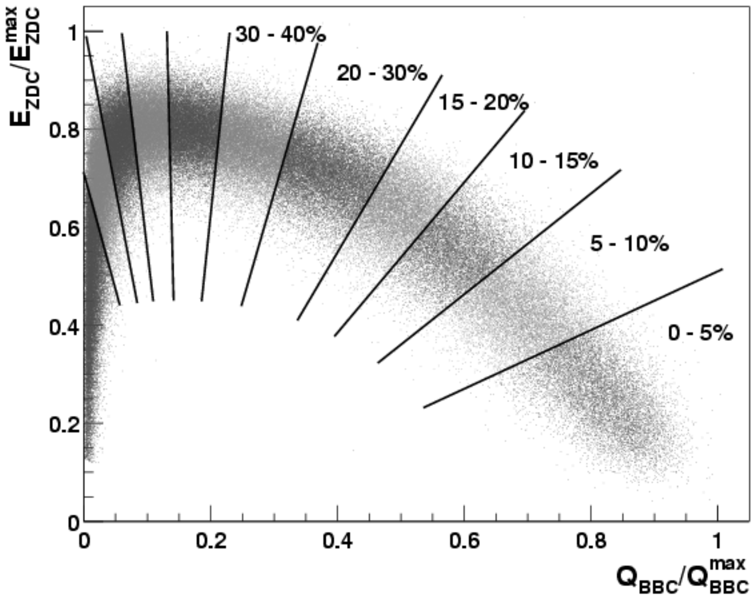

Figure 3.5: The correlation between BBC charge sum and energy deposit in ZDC.

The MVD, which consists of two concentric barrels of silicon strip detectors around the beam-pipe and two disk-shaped endcaps of silicon pad detectors, provides event characterization such as a collision vertex position and fluctuations in charged particle production.

3.2.2 The central spectrometers

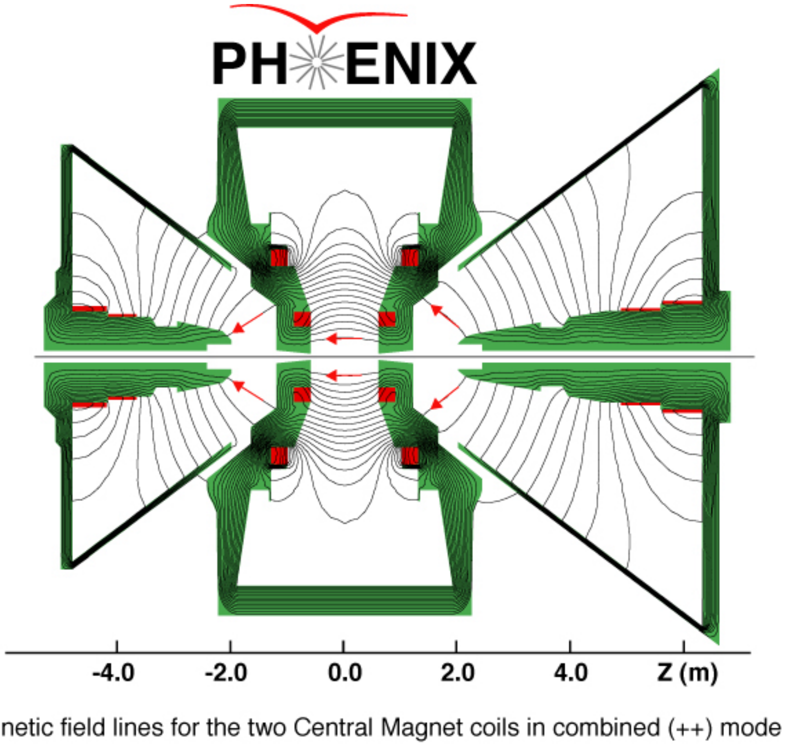

Figure 3.6: A simulation of the magnetic field lines inside the three PHENIX magnets. The arrows on the inner field lines represent the field direction.

The central spectrometers surrounds the both sides of the beam pipe as shown by the right and left detector groups in the top panel of Fig. 3.3, called as the East arm and the West arm, respectively. Each of the central arms covers the pseudorapidity region $|\eta| < 0.35$ and $\Delta\phi = \pi/2$ in azimuthal angle.

The tracking system of the central spectrometers is composed of the Drift Chambers (DCH), the Pad Chambers (PCs) and the Central Magnet (CM). The DCHs are primary tracking detectors, which are located in the region from 2 to 2.4 m from the beam axis and 1.8 m width along the beam axis in the East and West arms. Each of DCHs covers the pseudorapidity region $|\eta| < 0.35$ and $\Delta\phi = \pi/2$ in the azimuthal angle. In DCH, hit positions of charged particles are mapped by 3 types of wires, called X,U,V wires – X wire run in parallel to the beam axis and U,V wires have stereo angle about 6° to the beam axis. Using these hit positions, the 3-dimensional trajectories of charged particles are determined by a track reconstruction model.

The CM produces an axial magnetic field around the collision vertex that parallel to the beam axis by two pairs of concentric coils. The track reconstruction model is able to determines the transverse momentum of each particle from its curvature bended in the magnetic field. Fig. 3.6 illustrates a vertical cutaway view of the PHENIX magnets with the magnetic field lines. The total field integral of the CM is 0.78 T·m, and that is minimized for the radius of $R > 2$ m to avoid photo-multiplier tubes of the Ring Imaging Cherenkov Counter (RICH) and Electro-Magnetic Calorimeter (EMCal) detectors. The field covers pseudorapidity region $|\eta| < 0.35$, allowing momentum measurement of charged particles in the polar angle range $70^\circ < \Theta < 110^\circ$.

Three (two) layers of PCs are installed in the West (East) arm. The PC1, which is located at radius of ∼2.5 m between DCH and RICH detectors in both arms, is the most inner pad chamber system. The z-coordinate hit position of charged particles in PC1 is used in the track reconstruction instead of that measured by DCH. The PC2 is located at radius of 4.2 m just behind RICH only in the East arm, and PC3 are located at radius of 5.0 m in front of EMCal in both arms. All the PC layers cover the full acceptance of each arm ($|\eta| < 0.35$ and $\Delta\phi = \pi/2$) at different radial positions. The PC system provides three-dimensional space points along the straight line particle trajectories outside the magnetic field and are needed to resolve the ambiguities in the outer detectors.

In the central arms, the particle identification (PID) is carried out by three types of detectors – RICH, EMCal and the Time-of-Flight counter (TOF), in conjunction with information measured by the tracking system such as the momentum and flight length. The RICH [42] is a threshold gas Cherenkov detector which serves as the primary electron

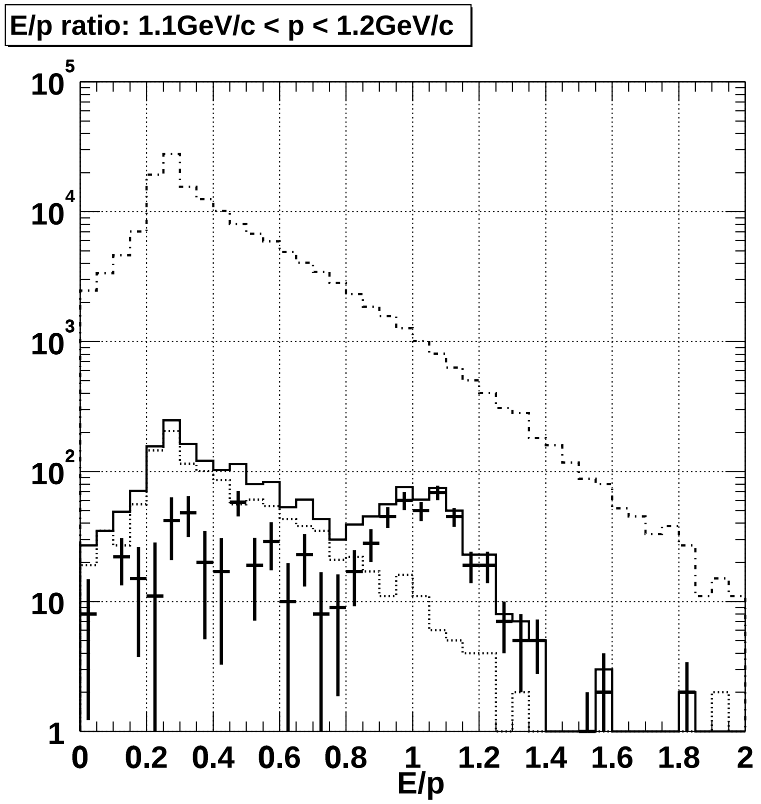

Figure 3.7: The energy/momentum ratio of tracks in the transverse momentum range $1.1 < p_{\mathrm{T}} < 1.2$ GeV/c, where the momentum is measured by DCH and the energy is measured by EMCal. The dashed-dotted line shows the distribution of all DCH tracks, and the solid line shows the tracks associated with RICH hits. The solid markers show the distribution of tracks associated with RICH hits after background (dotted line) subtraction.

identification detector. It measures Cherenkov radiation emitted by charged particles as they pass through a gas radiator with the high velocities greater than c/n, where c is the speed of light and n is the index of the refraction of gas. It provides e/π discrimination up to ~4 GeV/c where is the Cherenkov threshold of π. The RICH is located at the radial region from 2.6 to 4.1 m from the beam axis in the both east and west central spectrometers. Fig. 3.7 illustrates electron identification using the RICH detector. The dashed markers shows the ratio of energy and momentum (E/p) of charged tracks associated with a RICH hit after subtracting the background. A clear peak around E/p ~1

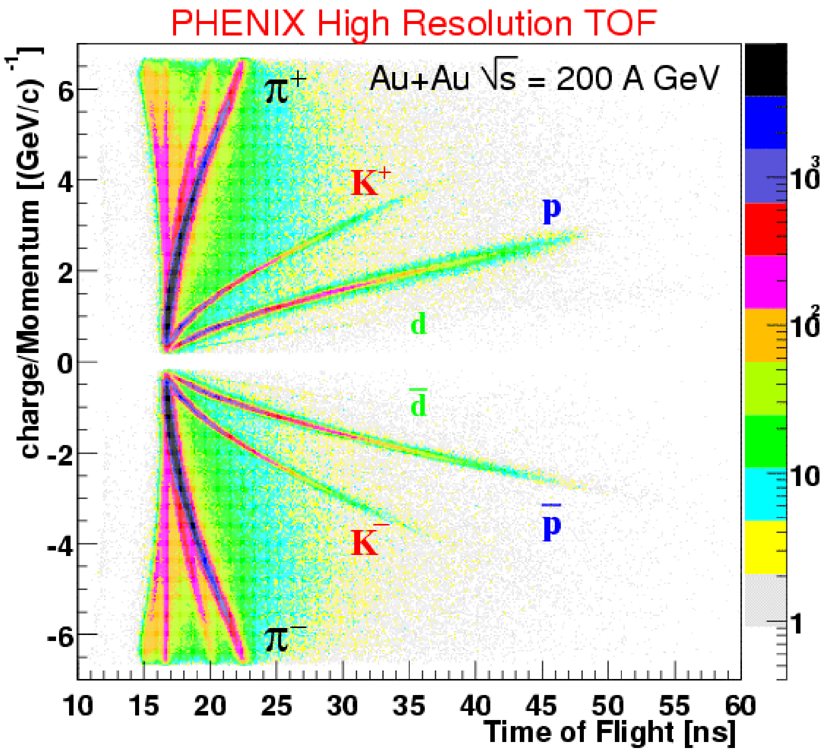

Figure 3.8: Scatter plot of the time-of-flight by TOF versus reciprocal momentum ($1/p$) in minimum bias Au+Au collisions at $\sqrt{s_{\rm NN}}$ = 200 GeV.

is the electron signal.

The TOF is the primary device to identify charged hadrons in PHENIX, which is located at the radius of ∼5.1 m from the beam axis. 960 plastic scintillation slats are arranged into 8 panels in the top sector which covers $|\eta| < 0.35$ and $\Delta\phi = \pi/4$ and 2 panels in the bottom sector which covers 1/4 of the top panel. The z-coordinate hit position (along the beam axis) is determined with the 1.5 cm width of each slat, and the x(y)-coordinate hit position (along the slat) is determined from the time difference of signals observed by readouts at the two ends by using the known velocity of light propagation in the scintillator. The hit timing of particle is determined from the averaged time of signals read out at both ends. The timing resolution of the TOF is measured in the experimental condition to be 120 psec in conjunction with the start time of collisions provided by BBC. Fig. 3.8 shows a scatter plot of the time-of-flight measured by TOF versus reciprocal

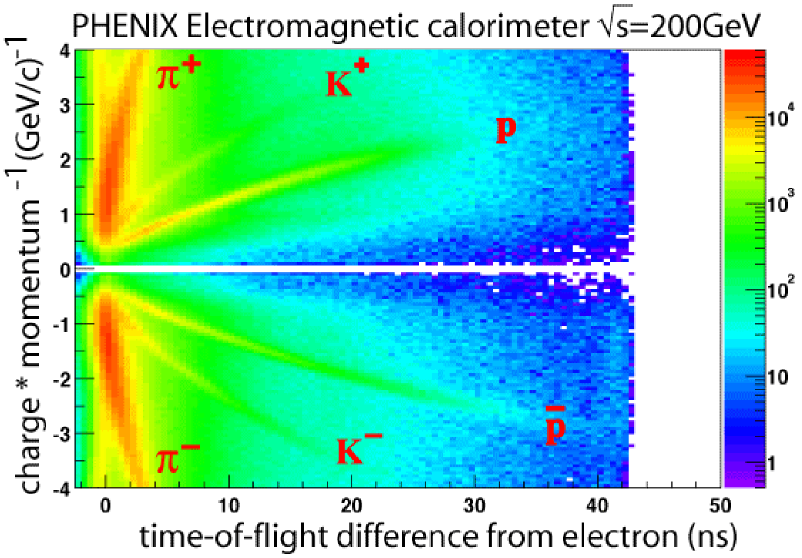

Figure 3.9: Scatter plot of the time-of-flight by EMCal (PbSc) versus reciprocal momentum ($1/p$) in minimum bias Au+Au collisions at $\sqrt{s_{\rm NN}}$ = 200 GeV.

momentum measured by DCH in minimum bias Au+Au collisions at the energy of $\sqrt{s_{\rm NN}}$ = 200 GeV. The good timing resolution allows π/K separation up to 2.4 GeV/c and K/p separation up to 4 GeV/c.

The Electro-Magnetic Calorimeter (EMCal), which is the most outer detector in the central arm, is the primary device to provide energies and spatial hit positions of photons and charged particles. The EMCal consists of 8 sectors (4 in each arm) and covers the full acceptance region of the two central arms, $|\eta| < 0.35$ and $\Delta\phi = \pi/2 \times 2$. Its front face is located at ~5.1 m from the beam axis. There are two types of EMCal detectors in the system, namely lead-scintillator sampling calorimeter (PbSc) and lead-glass Cherenkov calorimeter (PbGl). The PbSc covers 6 out of the 8 EMCal sectors, i.e. 4 sectors in the West arm and the top 2 sectors in the East arm, and the PbGl covers the remaining bottom 2 sectors in the East arm. The PbGl has been utilized by not only photon analyses but also lots of hadron analyses which need high statistics of data sample because of its large acceptance coverage. The timing resolution of charged hadrons is measured to be about 400 psec. Fig. 3.9 shows a scatter plot of the time-of-flight measured by PbSc versus reciprocal momentum measured by DCH in Au+Au collisions.

In addition to the detectors described above, the Time Expansion Chamber detector (TEC) were being developed during Run-2 operation. The TEC is placed between the DCH and the PC3 in the East arm, covering $|\eta| < 0.35$ and $\Delta\phi = \pi/2$, is capable of tracking all charged particles passing through the acceptance of RICH and the electromagnetic calorimeter in the East arm.

3.2.3 The muon spectrometers

The muon spectrometers are located at the pseudorapidity ranges of $-2.25 < \eta < -1.15$ (the South Muon Arm) and $1.15 < \eta < 2.44$ (the North Muon Arm) with the full azimuthal coverages [38]. Each Muon Arm is composed of the Muon Tracker with the Muon Magnet and the Muon Identifier. It is designed to measure vector mesons, especially dimuons from J/ψ and ψ', the Drell-Yan process and heavy quark productions.

Each Muon Tracker provides trajectories of charged particles with the resolution of 100 μm. It is comprised of three stations of cathode-strip readout tracking chambers which are stationed inside the Muon Magnet, which produces radial magnetic fields by solenoid coils, as shown by 3.6, and the total field integral is 0.72 T·m at $\Theta = 90°$. The Muon Identifier is comprised of six walls of steel absorbers interleaved with five layers of plastic proportional Iarocci tubes. The set of Iarocci tube layers provides muon identification and $\mu\pi$ separation by the amount of radiation. Only the south Muon arm is installed for Year-2 operation.

3.3 The PHENIX subsystems

For the identification of charged pions, I used the tracking system and EMCal (PbSc) at the west central arm. The details of the PHENIX subsystems, which are needed for the centrality determination and the charged pion identification, are described in this section. Acceptances and purposes of all PHENIX subsystems are summarized in Table 3.1.

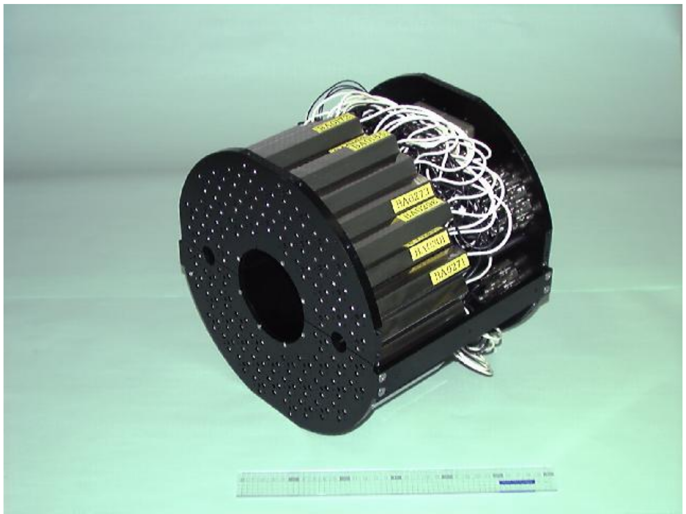

Figure 3.10: A picture of BBC array comprising 64 BBC elements.

3.3.1 Beam-Beam Counters

The PHENIX Beam-Beam Counters (BBC) [39], which are located at 1.5 m upstream and downstream of the beam crossing point and surround the beam pipe. Fig. 3.10 shows a picture of one of BBCs. Each BBC has 64 readout channels, and each channel consists of a quartz Cherenkov radiator and a mesh-dynode photo-multiplier tube (PMT) readout located behind the central magnet's return yoke. Since the magnetic field around this location is expected to be about 3kG, the BBC is designed to work in such a high magnetic field environment. The elements are closely packed into a ring surrounding the beam pipe and cover the pseudorapidity of $3 < |\eta| < 4$ and in 2π in azimuthal angle. In case of central Au+Au collisions at $\sqrt{s_{\rm NN}} = 200$ GeV, the number of charged particles per BBC element is expected to be about 15, while in case of p+p collisions, no or a few charged particles will be in the acceptance. Therefore, each element of BBCs is designed to has a large dynamic range from 1 MIP (Minimum Ionizing Particle) up to over 30 MIPs. In addition, the BBC system is designed to be radiation hard because it locates such a very forward angle where could be irradiated with an enormous amount of charged and neutral particles from collisions.

The BBC provides the start timing information of the beam-beam interaction, which

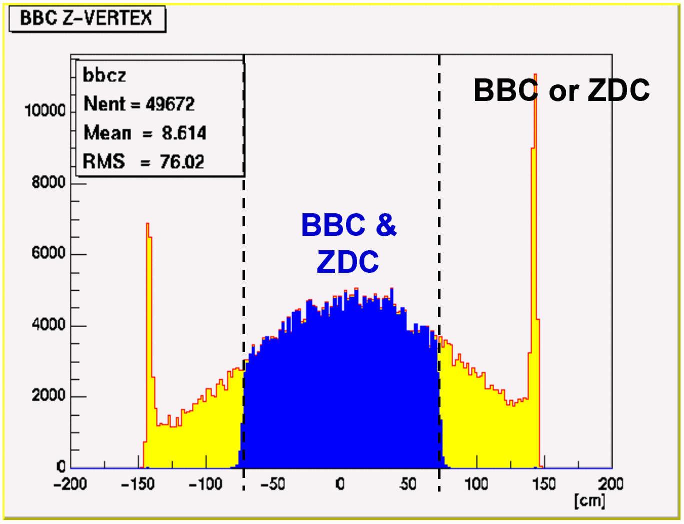

Figure 3.11: Z_{vertex} distribution measured by BBC. The blue area corresponds to events satisfying the Global Level-1 decision.

is calculated as:

$$t_{T0} = (T_1 + T_2 - 2L/c)/2, \tag{3.1}$$

where T_1 and T_2 are the observed values of arrival time for prompt particles at the each side and L is the length from the collision point to the surface of the BBC, 144 cm. Its vertex position along the beam axis is evaluated from the difference of the averaged arrival times as:

$$Z_{vertex} = (T_1 - T_2)c/2. \tag{3.2}$$

Fig. 3.11 shows the distribution of Z_{vertex} measured by BBC. The measured collision time is served as a start time for the time-of-flight measurement. The time resolution of each BBC element is evaluated to be around 52 ± 4 psec under real experimental conditions. The measured vertex position accuracy is estimated to be better than 1 cm. The information of collision time, vertex position and the number of PMT hits are sent to the LVL-1 trigger for the data acquisition system.

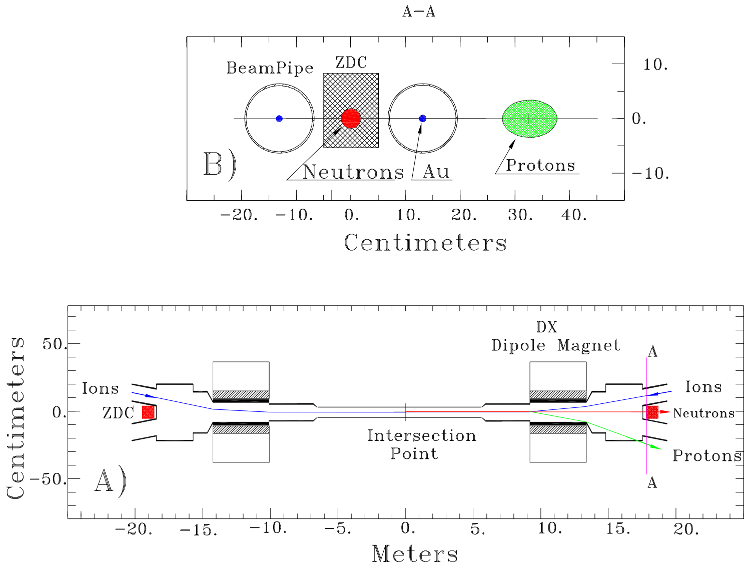

Figure 3.12: Schematic views of ZDC [40]. The bottom panel (A) shows a top view of the beam geometry and ZDC locations. The top panel (B) shows a “beam’s eye” view of the ZDC location (section A-A in the top panel).

3.3.2 Zero-Degree Calorimeters

The Zero-Degree Calorimeters (ZDC) [40] is a hadron calorimeter, which is commonly used by all RHIC experiments. In PHENIX, two ZDCs are located at 18.25 m upstream and downstream of the beam crossing point, where 3 m behind the DX dipole magnets which are used to bend beams, as shown by 3.12. At the location, charged particles emitted from collisions are also bent by the magnets so that ZDCs detect only charged free particles, i.e. spectator neutrons, traveling along the beam line left after collisions. It is designed to measure the fraction of energy deposited by spectator neutron within a 2 mrad ($|\eta| > 6$) cone around the beam direction The ZDC provides information about the vertex position and the start time of collisions from the difference of hit times between two (north and south) ZDCs. The resolution of measured vertex position is about 2 cm. The information of the number of hits on the ZDCs is sent to the LVL-1 trigger for the data acquisition system.

3.3.3 Drift Chamber detector

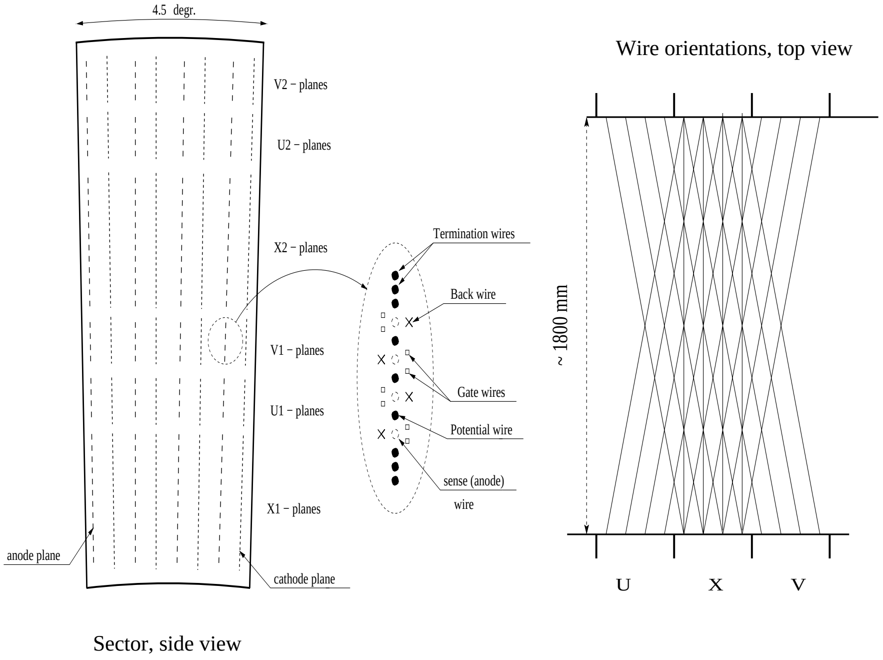

Figure 3.13: The left shows the layout of DCH's wire for one sector and the right shows a schematic diagram from top view.

Each of DCH consists of 20 sectors that are equally arrayed in the azimuthal angle, and each sector covers $\Delta\phi = 4.5°$. Each sector, which is composed of 4 cathode and 4 anode wire planes in the azimuthal direction and is filled with a 50-50% Argon-Ethane gas mixture, has six types of wire modules that are stacked radially from inside toward outside as X1, U1, V1, X2, U2 and V2. The each X wire module has 12 planes of anode wires in radial direction and those X wires are run parallel to the beam direction. Each of U and V wire modules has 4 planes of anode wires in the radial direction and those U (V) wires are tilted by about ±5° stereo angle relative to the X wires, allowing to measure z coordinate of tracks. The layout of wire position of the DCH is shown in Fig. 3.13. In the real experimental condition, hundreds of tracks come into the DCH region. The anode wires are electrically separated into two halves at the center, and signals in each side are read by independent readout channels. In case of Au+Au central collisions, the occupancy is about two hits per wire.

3.3.4 Pad Chamber detectors

The Pad Chamber (PC) [41] are multi-wire proportional chambers. At the west central arm, there are three layers of PC, called PC1, PC2 and PC3, and each layer consists of 8 sectors. Each sector is composed of a single plane of anode and field wires inside a Argon-Ethane mixture gas volume bounded by two cathode planes. One cathode is segmented into an array of pixels and another is made of solid copper plane. The charge is induced on a number of cathode pixels when a charged particle goes through the plane and starts avalanche close to anode wires. The pixels of cathode wires correct the charge with readout electronics. It provides 3-dimensional coordinates of charged tracks with the good spatial resolution and high efficiency. The hit position resolution in the z direction of PC1 is measured to be ±1.7 mm and the information is used by the offline track reconstruction model. The position resolutions of the PC1, PC2 and PC3 are summarized in Table 3.2.

3.3.5 Electro-magnetic calorimeters

For PbSc sectors fully cover the acceptance of the west central spectrometer. As shown by Fig. 3.14, each PbSc sector consists of 2592 (36×72) individual tower modules [43]. Each PbSc tower module is a shashlik type sampling calorimeter that is composed of 66 sampling cells made of alternating tiles of leads and scintillators. The surface area of each tower module is 5.5×5.5 cm^2 and the active depth is 38 cm with 18 radiation lengths. The sampling cells are optically connected by 36 longitudinally penetrating wavelength shifting fibers and collected light signals are read out by a PMT at the back of the tower. The PbSc calorimeter is specialized in identifications and measurements of total energies of photons and electrons. The energy resolution of the PbSc calorimeter is $8.1\%/\sqrt{E}[GeV]\oplus 2.1\%$ and the timing resolution is around 300 psec for photons. Because charged hadrons deposit a small fraction of those energies, PbSc also provides an arrival time of charged pions, kaons and protons. Using charged pions, the timing resolution is

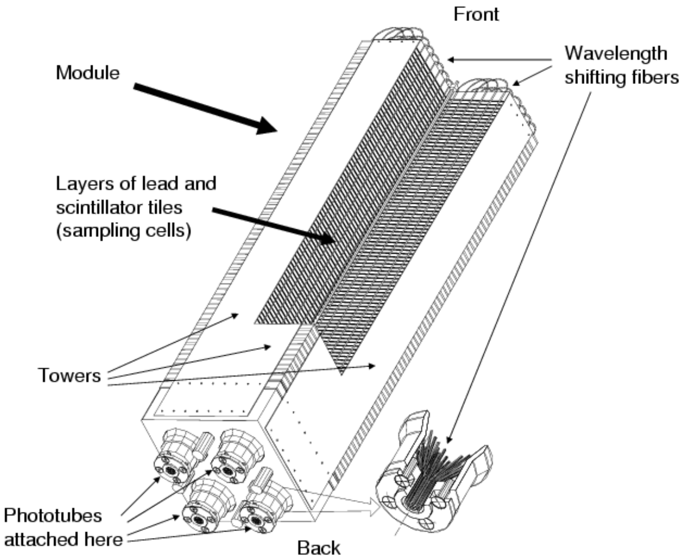

Figure 3.14: A cutaway view of lead-scintillator calorimeter module.

evaluated to be around 400 psec.

3.4 Trigger and Data acquisition system

As described above, the PHENIX detector consists of several subsystems, and each has hundreds to thousands readout channels. To handle a high rate and a large amount of data, the PHENIX data acquisition (DAQ) system is designed by using the pipeline processing technique which is performed by simultaneous triggering and readout. Fig.3.15 illustrates the block diagram of the DAQ system in detail. The PHENIX online system has two types of triggering levels, called the Level-1 (LVL1) and Level-2 (LVL2) triggers. The LVL1 trigger system is comprised of the Local Level-1 (LL1) systems which communicate with some participant detectors, and the Global Level-1 (GL1) system which provides a trigger decision according to the LL1 algorithm. If the LVL1 trigger accepts a collision event, the LVL1 trigger sends a signal to the Granule Timing Module (GTM) in conjunction with the RHIC clock provided by the the Master Timing Module. The GTM, which is equipped on each detector, requires the Front End Module (FEM) to send its

Subsystem	Resolutions
BBC	$\sigma_t 0 \sim 20$ psec, $\sigma_{zvertex} \sim 0.6$ cm
ZDC	$\sigma_{zvertex} \sim 2.5$ cm
DCH	$\sigma_\alpha \sim 1$ mrad, $\sigma_z \sim 2$ mm
PC1	$\sigma_{r\text{-}\phi} \sim 2.5$ mm, $\sigma_z \sim 1.7$ mm
PC2	$\sigma_{r\text{-}\phi} \sim 3.9$ mm, $\sigma_z \sim 3.1$ mm
PC3	$\sigma_{r\text{-}\phi} \sim 4.6$ mm, $\sigma_z \sim 3.6$ mm
TOF	$\sigma_t \sim 110$ psec
PbSc	$\sigma_E/E = 8.1\%/\sqrt{E} \oplus 2.1\%$, σ_t(photon) <300psec, σ_t(hadron) <400psec
PbGl	$\sigma_E/E = 5.95\%/\sqrt{E} \oplus 0.76\%$

Table 3.2: Summary of resolutions of the PHENIX subsystems for Year-2 running.

digitized data to the Data Correction Module (DCM). The DCM is designed to compress the large uncompressed raw data and send the data to the Event Builder (EvB). Finally, the EvB assembles the events in the final form.

The beam crossing rate of Au+Au at $\sqrt{s_{\rm NN}} = 200$ is 9.4 MHz and the Luminosities of 2×10^{26}cm^{-2}s-1. On the other hand, the maximum average of the PHENIX LVL1 trigger rate is about 25 kHz for Au+Au data taking. Therefore, the LVL2 trigger is designed to select potentially interesting events for all colliding species and to reject uninteresting events for the reduction of the data to the designed data acquisition rate.

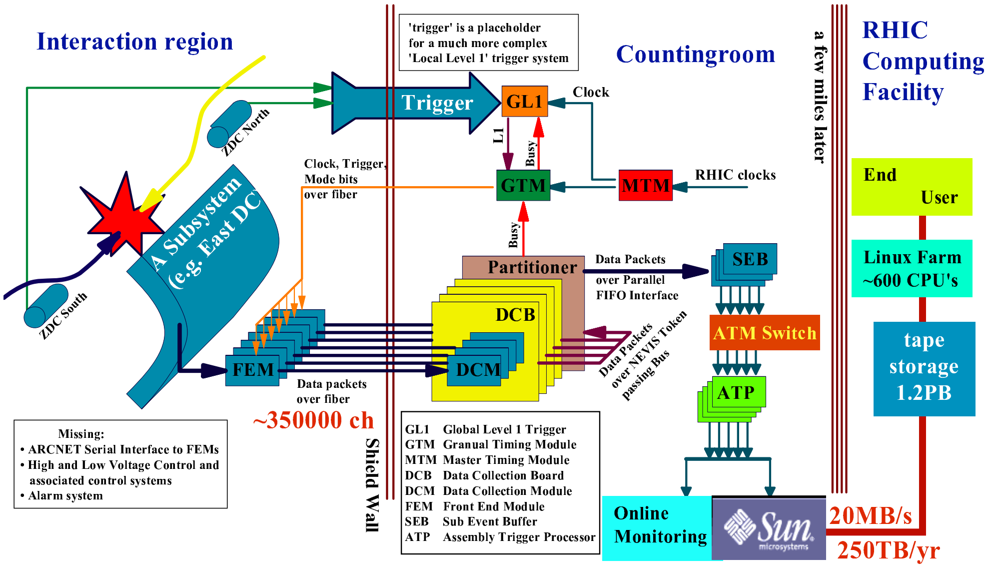

Figure 3.15: A block diagram of the PHENIX data acquisition system.

Chapter 4

Data Analysis

4.1 Run summary and event selection

In the Year-2 Au+Au running at RHIC, the PHENIX experiment took two types of physics events by the LVL-1 and LVL-2 triggers. The “minimum bias” events have been taken by the LVL-1 trigger determined by the two LL1 trigger requirements for BBC and ZDC as:

- At least two PMTs are fired in each of two (North and South) BBCs. And the collision vertex (Z_{vertex}) measured by BBC is within ± 75 cm from the center of the central spectrometers.
- At least one forward neutrons has to be registered in each of two ZDCs.

The minimum bias events include collision events from central to peripheral in 92% of the interaction cross section.

The interaction rate of the LVL-1 trigger is about 1400 Hz which corresponds to a data rate of 224 MB/s while the maximum event rate achieved by the data rate of PHENIX DAQ system during Year-2 operation is about 140 MB/s. The LVL-2 trigger is used to take only interesting physics events, which for example have high p_T particles, single electron (muon), electron (muon) pair, allowing to process all minimum bias triggers at the available maximum DAQ throughput and to reduce the data volume sufficiently so that all events accepted by the rare event triggers could be written to disk.

The PHENIX accumulated the integrated luminosity $\int Ldt \sim 24\ mb^{-1}$ which corresponds to 170 M minimum bias events in total for Year-2 Au+Au run. Fig. 4.1 shows a summary plot of luminosity measured by 4 experiments at RHIC. Out of the 170 M events, about 92 M events are taken as minimum bias events and about 14 M "rare" (about 64 M "non-interesting") events are taken (rejected) in the LVL-2 trigger. This analysis is based on about 90 M minimum biased events with the full magnetic field (0.78 T·m). In offline analysis, we required only one event selection cut to the minimum biased events as:

- The collision vertex position measured by BBC has to be $Z_{vertex} < 30$ cm.

After the above an event selection, we finally selected 23.1 M "good" events in total, which were guaranteed as high quality data enough for this analysis. The used run number is listed in table 7.1.

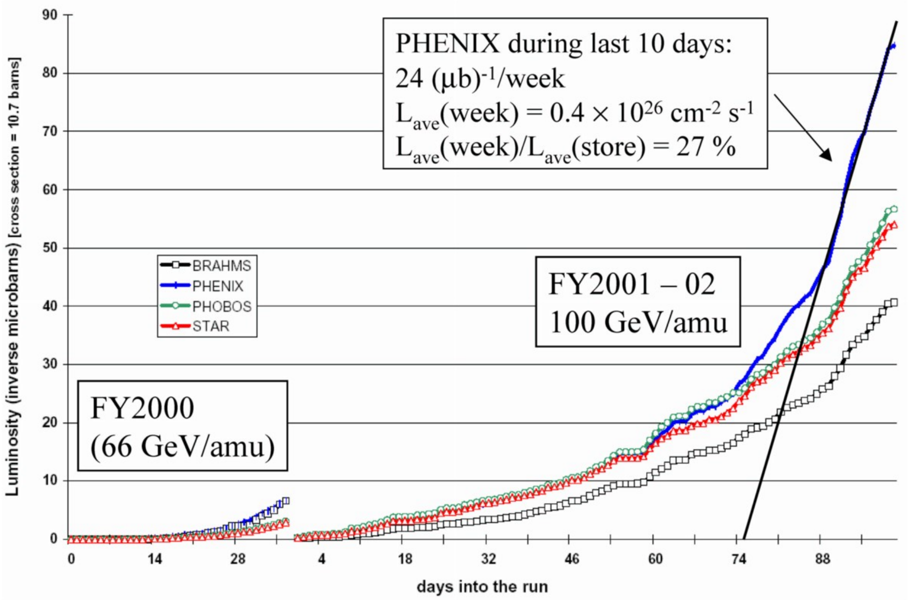

Figure 4.1: Luminosities estimated by PHENIX (blue), STAR (red), PHOBOS (green) and BRAHMS (black) for Year-2 Au+Au running.

4.2 Identical pair reconstruction

4.2.1 Track reconstruction and qualification

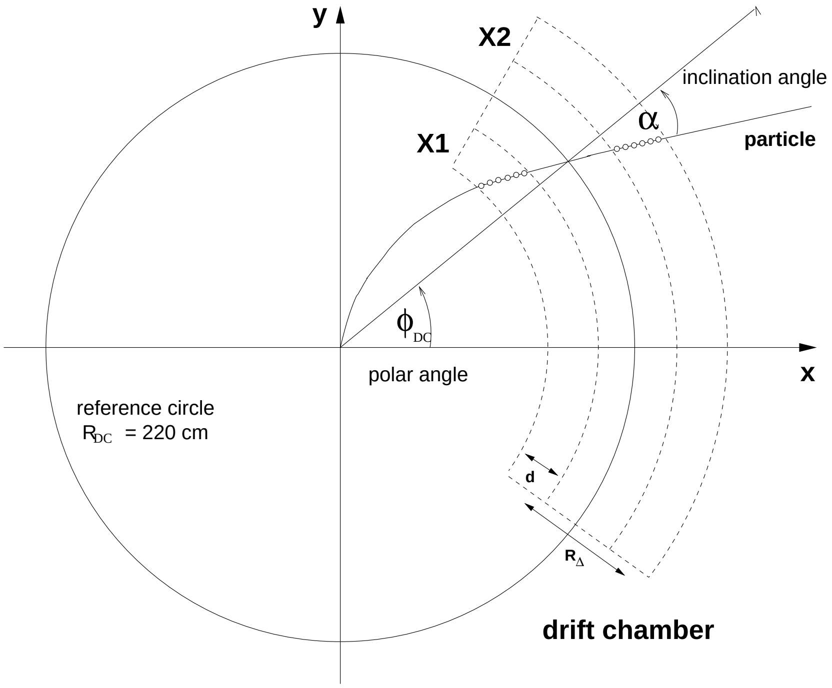

Figure 4.2: A schematic illustration of the Hough transform parameters ϕ_{DCH} and α_{DCH}.

Track reconstruction for charged particles in the central arm is performed by using its hit information at DCH and PC1. In the DCH, the track finding is performed based on the Combinatorial Hough Transform (CHT) technique [45]. In this technique, trajectories of charged particles are determined in two dimensional coordinate space from those hits on X-wires of DCH, as shown by a schematic illustration in 4.2. The two-dimensional space is defined by the polar angle ϕ_{DCH} at the intersection of the track with a radius at the mid point of the DCH ($R = 220$ cm), and the inclination angle of the track α_{DCH} at the point. The α_{DCH} is the angular deflection from a straight line of ϕ_{DCH} and proportional to the inverse of the transverse momentum in the magnetic field bend plane. The z information of charged tracks is obtained by using stereo wires, called U,V-wires, of the DCH with the resolution of σ ∼2.0 mm. In the reconstruction model used in this study, more precise z information is actually provided by PC1 with the resolution of σ ∼1.7 mm. Thus we required the projection of reconstructed track onto the PC1 has an associated cluster. In addition, we required the reconstructed track to have hit on U,V-wires also for the track qualification. The details of the CHT technique and track reconstruction at PHENIX can be found in references [44, 45].

Momentum for each charged particle is reconstructed from its azimuthal and polar angles determined by DCH and PC1, and the vertex position measured by BBC. Since the analytical determination of momentum at PHENIX central spectrometers is too complicated to solve due to its non-uniform integrated magnetic field, so a look-up table has been used to determine the momentum. In the Year-2 calibration, the momentum resolution is $\delta p/p \simeq 0.7\% \oplus 1.0\% \times p$ (GeV/c), where the first term is due to the multiple scattering before the DCH and the second term is the angular resolution of the DCH.

4.2.2 Track matching to EMCal cluster

The arrival time of particles of interest for this analysis, namely charged pions, are measured by EMCal (PbSc) at the west central spectrometer. To remove ghost tracks and also accidentally mis-identified tracks, each track is required to have an associated hit on the EMCal within an acceptable σ of the track's projection to the EMCal, where σ refers to the resolution of the projection. We call this method as "track matching" cut for the track qualification. The track matching cut is done in two directions, ϕ and z, separately defined as:

$$\begin{aligned} \Delta\phi_{match} &= \phi_{clus} - \phi_{proj} = tan^{-1}(y_{clus}/x_{clus}) - tan^{-1}(y_{proj}/x_{proj}) \quad (4.1) \\ \Delta z_{match} &= z_{clus} - z_{proj}, \quad (4.2) \end{aligned}$$

where x_{proj}, y_{proj} and z_{proj} are the projection of each track onto the EMCal surface, and x_{clus}, y_{clus} and z_{clus} are the hit position of a EMCal cluster which is nearest from the track's projection. Left two panels in Fig. 4.3 show the contour plots of $\Delta\phi_{match}$ (top) and Δz_{match} (bottom) versus signed momentum. The resolutions of track matching in ϕ (σ_ϕ) and z (σ_z) directions are evaluated by Gaussian fits of the residual distributions of track matching in each 100 MeV slice of momentum. Right two panels in Fig. 4.3

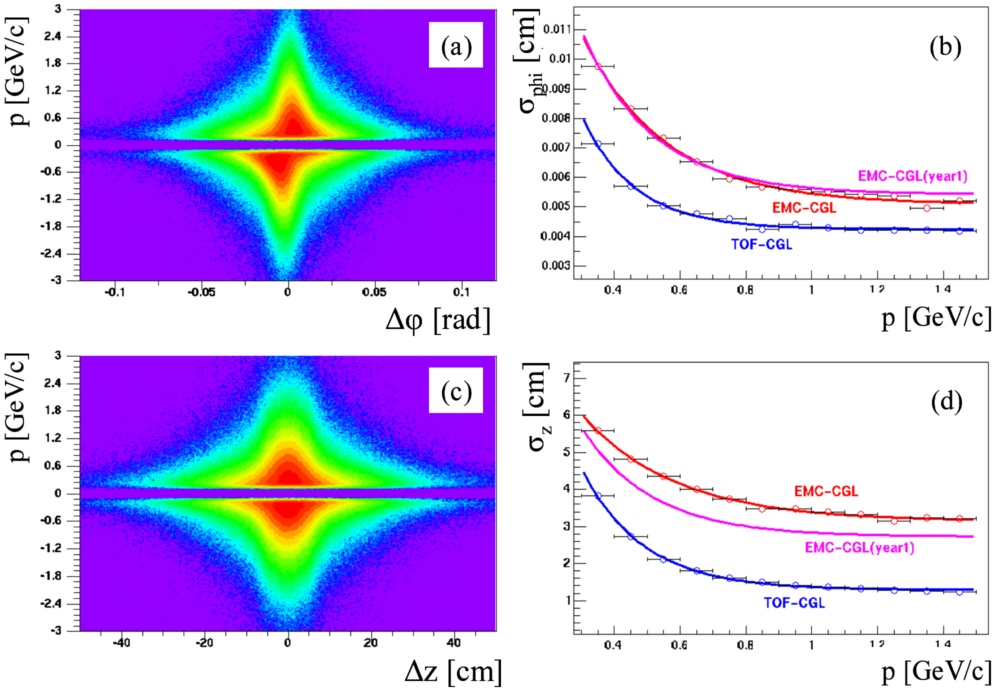

Figure 4.3: Track matching between reconstructed track and its associated cluster on EMCal. (a) and (c) show contour plots of residuals of track matching in ϕ and z direction versus signed momentum. The right panels show the momentum dependence of the matching resolution for positive charged tracks in ϕ (b) and z (d) directions. The overlaid lines are fits of an exponential function.

show σ_ϕ and σ_zs for positive charged tracks as a function of momentum. The momentum dependences of σ_ϕ and σ_z are parameterized by the fit of an exponential function, as shown by curves in Fig. 4.3, then we require tracks to be within 2-σ_ϕ and 2-σ_ϕ from the center of widths. These matching cuts are done for positive and negative charged particles, separately. Then, we finally obtained an arrival time of each associated track on EMCal.

4.2.3 Particle identification

For each track which is qualified by track selection and matching cuts described above, we measured its mass by using time-of-flight technique. The time-of-flight (T) of each

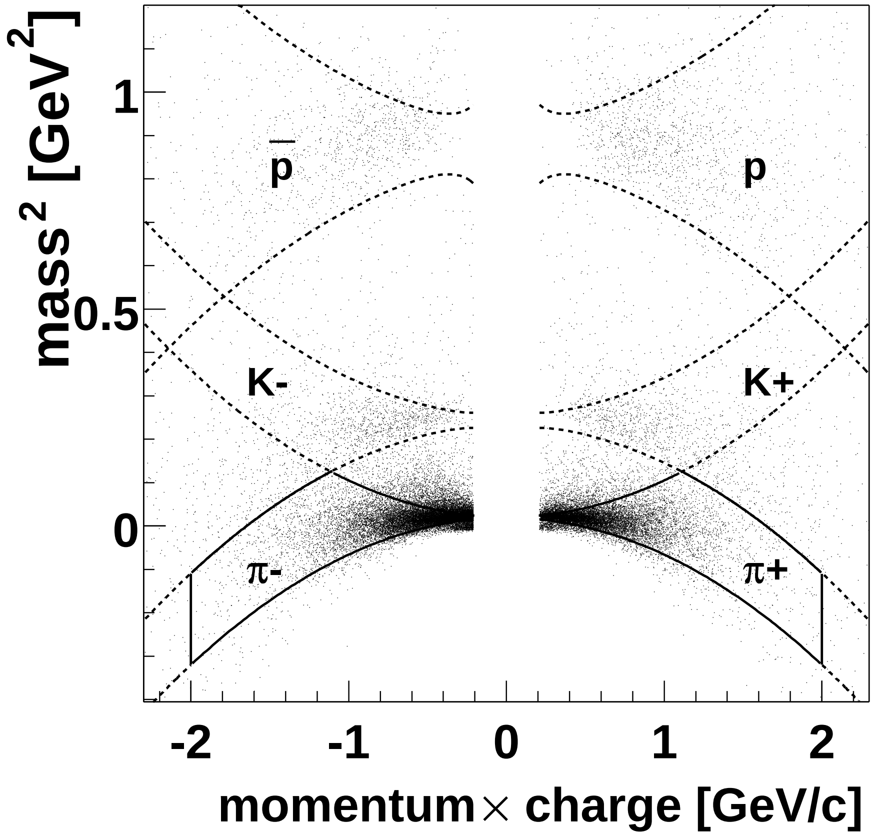

Figure 4.4: Scatter plot of signed momentum versus squared mass reconstructed using EMCal's timing information. Overlaid dashed lines mean 1.5-σ width of estimated squared mass resolution for pions, kaons and (anti-)proton. Charged tracks, in the regions within 1.5-σ from pion mass peaks and 1.5-σ away from kaon mass peak and $0.2 < |p| < 2.0$ GeV/c as shown solid lines, is identified as pions for this analysis.

particle was determined by the difference between a start time measured by BBC and an arrival time by EMCal as:

$$T = T_{\mathrm{EMC}} - t_{T0}. \tag{4.3}$$

For EMCal, run-by-run and tower-by-tower timing offsets are calibrated using photons so that the arrival time of photon is set to zero. Thus, the arrival time of each particles is determined by its arrival time plus the ideal time of flight of photon for the length from

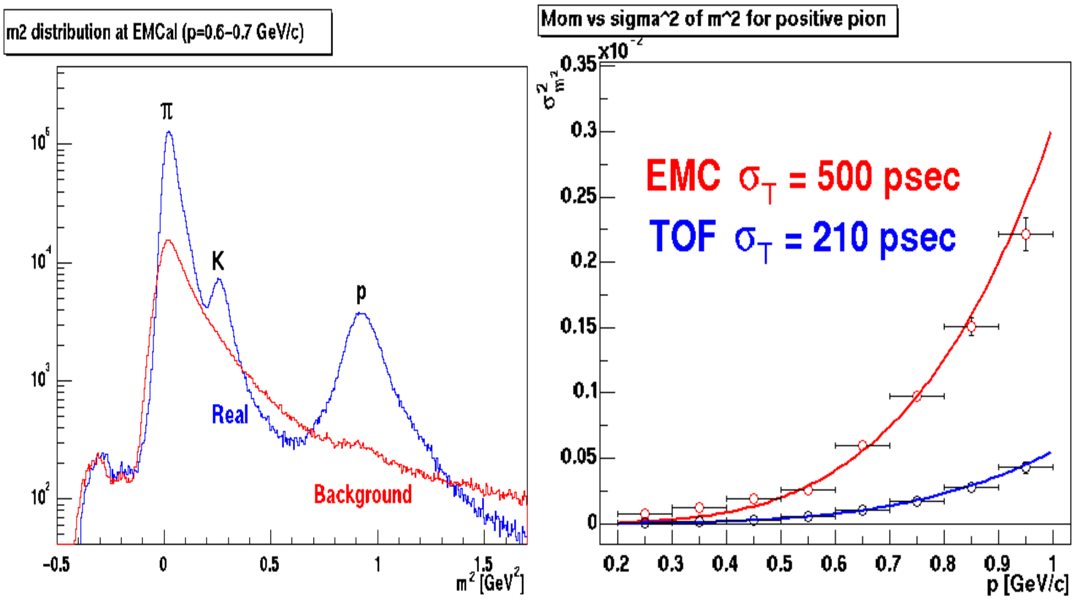

Figure 4.5: The left panel shows a squared mass distribution of positive particles in a momentum slice between $0.6 < p < 0.7$ GeV/c (left). The red and blue lines show the real and background distributions. The right panel shows squared mass resolution (σ_{m^2}) as a function of momentum.

collision vertex to the particle hit position as:

$$T_{\mathrm{EMC}} = T0_{\mathrm{EMC}} + \sqrt{x_{clus}^2 + y_{clus}^2 + (z_{clus} - Z_{vertex})^2}/C. \tag{4.4}$$

As described in the previous subsection, momentum for each particle (p) were determined from its curvature in the magnetic field by using the track model. In addition, the track model provides its flight path-length (L) from the collision vertex to the hit position on EMCal for each particle. Using these parameters, the squared mass for each particle was measured as:

$$m^2 = p(\frac{T^2c^2}{L^2} - 1). \tag{4.5}$$

A scatter plot of signed momentum versus the calculated squared mass is shown in Fig. 4.4. A squared mass distribution of positive charged particles in the slice of 0.6−0.7 GeV/c is shown by the red in the left panel in Fig. 4.5. To account for the background distribution due to the accidental hit on EMCal cluster, we use "z-flip" technique. In the technique, the projection of each track onto EMCal in z direction z_{proj} is converted to the opposite signed value, $-z_{proj}$, then applied the same 2-σ matching cut to the z-flipped track to find out an accidentally associated cluster. Using the arrival time of the cluster, the background distribution of squared mass is evaluated by Eq. 4.5, as shown by the blue in the left panel in Fig. 4.5. After subtracting the background from the real mass squared distribution, we fit pion peak with a Gaussian function to estimate the squared mass resolution as a function of momentum range, as shown in the right panel in Fig. 4.5. Assuming the error on the path-length can be neglected, the resolution of squared mass has been parameterized as:

$$\sigma_{m^2}(p) = \sqrt{\frac{\sigma_\alpha^2}{K_l^2}(4m^2p^2) + \frac{\sigma_{ms}^2}{K_l^2}[4m^4(1+\frac{m^2}{p^2})] + \frac{\sigma_t^2 c^2}{L^2}[4p^2(m^2+p^2)]}, \tag{4.6}$$

where σ_α and σ_{ms} are an angular resolution of α_{DCH} and a contribution from multiple scattering at DCH [46], which have been fixed in Run-2 to be σ_{alpha}= 0.86 mrad and σ_{ms} = 0.835 mrad, respectively. K_l^2 is an angular field kick parameter, which has been determined to be 84 $mrad/GeV$ in the previous analysis. From the fit of measured $\sigma_{m^2}(p)$ with Eq. 4.6, the timing resolution of EMCal (PbSc) σ_t is evaluated to be ~500 psec. Using the momentum dependent squared mass resolution, pions are selected by a requirement that its squared mass must be lie within 1.5-σ of their squared mass peak but 1.5-σ away from the kaon PID bands, as shown by solid curves in Fig. 4.4. After the PID qualification cut, about 45 million positive pions and 51 million negative pions are selected in a momentum range from 0.2 to 2.0 GeV/c for the most central 92% of collisions. The number of events and tracks utilized in this analysis are summarized in Table 4.1.

4.2.4 Signal and background pairs

Using identified charged pions, I assemble like-sign pion pairs. “Signal” pairs are assembled from all possible pair combination of like-sign pions in each event. For example, if one event contains 4 positive pions, this algorithm returns 6 positive pion pairs. Hence, we explicitly required each event to have 2 positive and/or negative pions at least.

(1)	Minimum biased events	$\sim$92M
(2)	"good" events	23.1M
(3)	Total num. of tracks in (2)	2751.2M
(4)	(3) + EMCal matching cut	683.7M
(5)	(4) + DCH quality cut	261M
(6)	(5) + PID cut	π^+: 84.8M ($\sim$3.7/event) π^-: 93.1M ($\sim$4.0/event)
(7)	pion pairs made from (6)	$\pi^+\pi^+$: 110.4M, $\pi^-\pi^-$: 139.8M
(8)	(7) + pair separation cut	$\pi^+\pi^+$: 109.8M ($\sim$4.8/event) $\pi^+\pi^+$: 139.1M ($\sim$6.1/event)

Table 4.1: Summary of utilized statistics of event, track and pair.

The product of two single particle probabilities, described in the dominator of Eq. 2.1, is experimentally measured by using "mixing" technique, in which pairs are assembled from different two events. We call it "background" pair hereafter. To make the background pairs, we hold a hundred events which were used for signal pair generation, then all possible event combinations are assembled with a selection cut as:

$$|Z_{vertex}(i) - Z_{vertex}(j)| < 1.0\ cm \quad (i, j = 1, 2, 3, ..., 100, i \neq j). \tag{4.7}$$

We call it "mixed event" hereafter. Then, the background pairs are assembled by the combinations of two identical pions picked up from any different two mixed events. After all possible background pairs are assembled using the first hundred events, we move on to the next hundred events.

4.3 Two-track efficiency corrections

4.3.1 Monte Carlo data reconstruction

The two-particle correlation function could be degenerated experimentally by two-track detection inefficiencies due to the finite resolution of detectors in a small relative separation. Thus the observation probability of the signal pairs for like-sign pions in low relative momentum are depend not only on the Bose-Einstein correlation and Coulomb repulsion but also on the two-track detection inefficiencies while the background pairs are independent of those effects. To correct only the effect due to the detection inefficiency from the signal pair distribution, the Monte-Carlo (MC) detector simulation is applied to estimate the correction factor for the DCH and EMCal. (Please refer to the next chapter the Coulomb correction.) For the MC study, we generated about 150M events with $Z_{vertex} = 0$ and each event contains 10 positive pions. The 10 pions were generated to reproduce pion momentum spectra measured by PHENIX at $\sqrt{s_{\mathrm{NN}}} = 200$ GeV [5], only within its acceptance for the PHENIX west-arm in the full (0.78 T·m) magnetic field. Hit responses in the detector components, such as electro-magnetic shower and Cherenkov radiation, are emulated by the GEANT simulator [48]. The detector simulator outputs the same raw data format as the real data. After reconstruction of simulated event data from the raw data set, we applied the same track quality and EMCal association cuts as those described in the previous section. Fig. 4.6 (left) shows a scatter plot of track matching defined by Eq. 4.1 evaluated by the MC ($\Delta\phi^{\mathrm{MC}}_{match}$) versus momentum of pions, and the right plot shows the resolution of track matching as a function of momentum. The momentum dependence of matching resolutions from MC simulation is in good agreement with that of the real data. We applied the same 2-σ matching cuts in ϕ and z directions to the pion tracks of MC simulation as that used to real data.

Fig. 4.7 (left) shows the scatter plot of signed momentum versus squared mass of simulated positive pions after applying the track qualification and matching cuts. Fig. 4.7 (right) shows the squared mass distribution of the simulated pions for momentum range $0.7 < p < 1.0$ GeV/c, comparing to that of charged particles of real data. We applied the same PID cut to the simulated pions as the real data, namely 1.5-σ within its pion peak for the momentum range between 0.2 to 2.0 GeV/c. After applying the PID cut, about 18 million pions remain. Then we assembled pion pairs by using the same method as that used for the real data. About 10 million simulated pion pairs are selected and used for the pair inefficiency estimate.

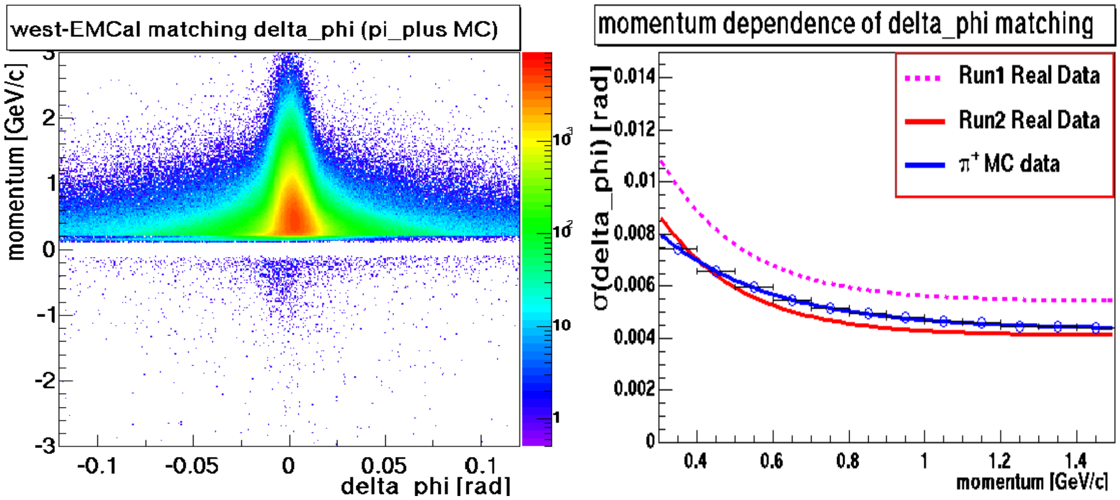

Figure 4.6: A scatter plot of $\Delta\phi_{match}$ versus reconstructed momentum of simulated positive pions (left), and the resolution of track matching as a function of momentum (right) comparing to that of real data for Year-1 and Year-2 running.

4.3.2 Two-track detection efficiency at DCH

Using MC simulation data, the two-track (pion pair) detection efficiency is defined by the intensity of signal pion pairs relative to that of background pion pairs respectively. For DCH, the efficiency is determined as a function of relative separations of the azimuthal angle ($\Delta\phi_{\rm DCH}$) and the longitudinal distance ($\Delta Z_{\rm DCH}$) of pion pairs in DCH as:

$$\varepsilon_{mix}(\Delta\phi_{\rm DCH}) = A^{\rm MC}(\Delta\phi_{\rm DCH})/B^{\rm MC}(\Delta\phi_{\rm DCH}) \times norm., \tag{4.8}$$

$$\varepsilon_{mix}(\Delta Z_{\rm DCH}) = A^{\rm MC}(\Delta Z_{\rm DCH})/B^{\rm MC}(\Delta Z_{\rm DCH}) \times norm., \tag{4.9}$$

and $A^{\rm MC}$ and $B^{\rm MC}$ are signal and background pion pair distributions of MC data, respectively. The yield of background pair distribution is normalized to that of signal pair distribution at high $\Delta\phi_{\rm DCH}$ region where the perfect pair detection efficiency is expected ($\Delta\phi_{\rm DCH} > 0.1$ rad).

Fig. 4.8 (left) shows the intensity of simulated positive pion pairs at DCH as a function of $\Delta\phi_{\rm DCH}$ and $\Delta Z_{\rm DCH}$. There is a significant enhancement and suppression of the two-track detection efficiency in small $\Delta\phi_{\rm DCH}$ and $\Delta Z_{\rm DCH}$ regions, which are due to ghost tracks and a track sharing effect, respectively. After eliminating both signal and back-

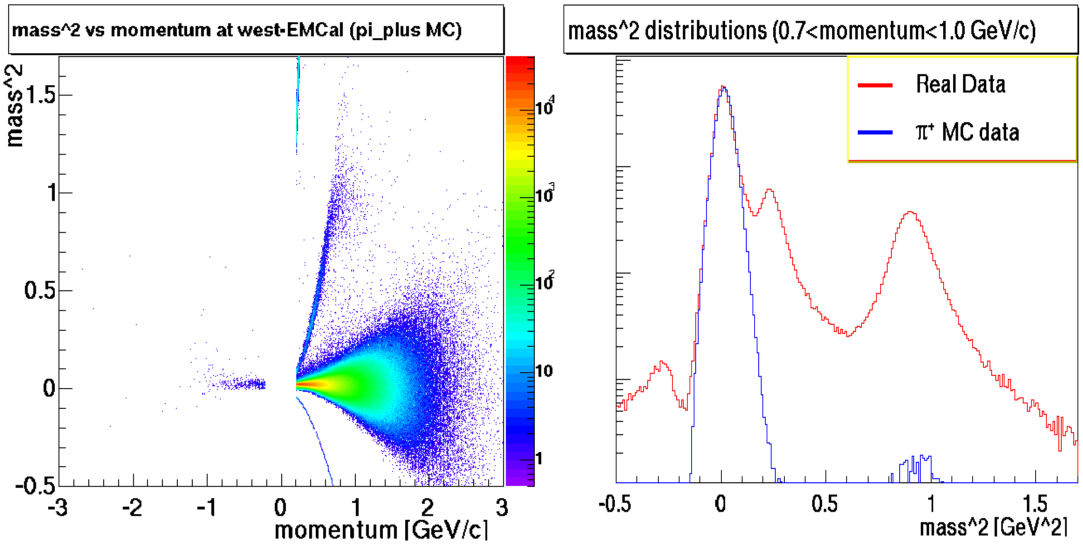

Figure 4.7: A scatter plot of signed momentum versus squared mass of simulated positive pions reconstructed by the PHENIX Monte-Carlo detector simulator (left), and a comparison of squared mass distributions between the simulated positive pion and real positive particles in a momentum range for 0.7 GeV/c $< p <$ 1.0 GeV/c (right).

ground pairs in these small relative separation regions, the two-track detection inefficiency is seen only in the small $\Delta\phi_{\rm DCH}$ while it is constant at unity in $\Delta Z_{\rm DCH}$ direction. Thus the two-track detection efficiency of DCH is defined as a function of $\Delta\phi_{\rm DCH}$, $(\varepsilon_{mix}(\Delta\phi_{\rm DCH}))$. The estimated $\varepsilon_{mix}(\Delta\phi_{\rm DCH})$ is shown in the right panel of Fig. 4.8, where we removed pairs in $\Delta Z_{\rm DCH} < 1$ cm and $\Delta\phi_{\rm DCH} < 0.06$ rad, $\Delta Z_{\rm DCH} < 5$ cm and $\Delta\phi_{\rm DCH} < 0.03$ rad to avoid the ghost tracks and track sharing effect, respectively.

4.3.3 Multiple track reconstruction efficiency

So far we have been talking about the two-track detection efficiency in a case of a low multiplicity event, as denoted as We denoted the multiplicity insensitive efficiency as $\varepsilon_{mix}(\Delta\phi_{\rm DCH})$. In a realistic experimental condition, however, the two-track detection efficiency is rather suppressed by the track multiplicity. The multiplicity dependence of the two-track detection efficiency has been estimated by using an embedding technique. In an embedding method, few simulation tracks are embedded into a minimum bias event

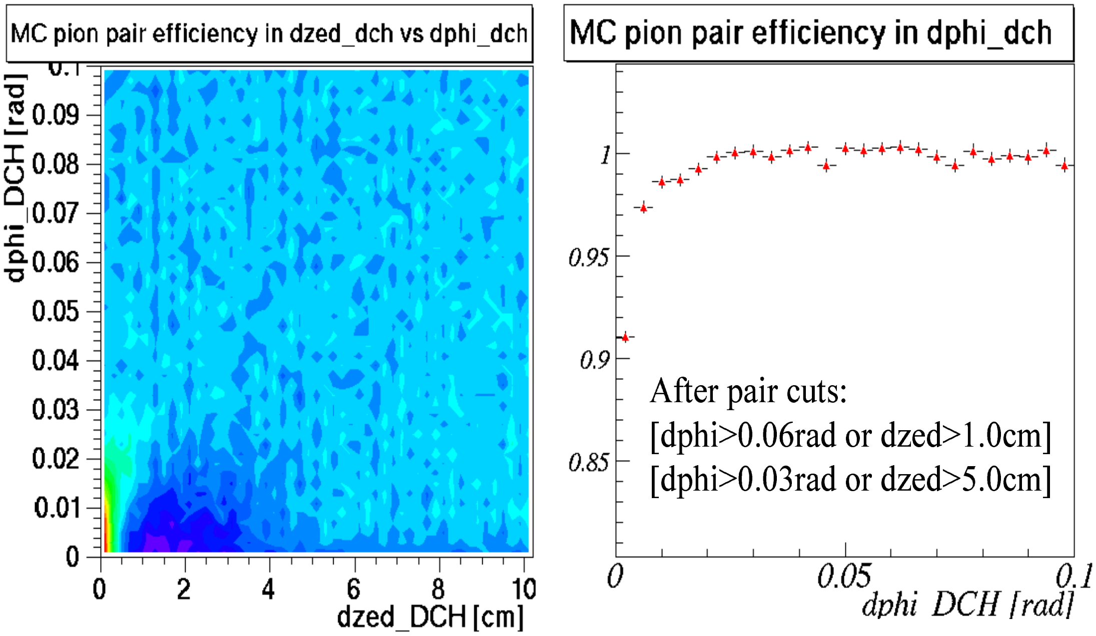

Figure 4.8: Relative separations of simulated positive pion pairs at the DCH. The pair distribution is statistically normalized by the background pair distribution. In the left panel, the horizontal axis is $\Delta Z_{\rm DCH}$ and the vertical axis is $\Delta\phi_{\rm DCH}$. The left panel shows the $\Delta\phi_{\rm DCH}$ distribution after removing pairs in ghosting and significant pair inefficient region.

of real data, then reconstructed as real tracks. In case of a high multiplicity event, some of the embedded tracks must be lost due to the finite reconstruction capability of DCH or anything else.

For the embedding, we prepared about one million minimum-biased real events in Au+Au collisions at $\sqrt{s_{\rm NN}} = 200$ GeV, and 10 million MC events, each has 5 positive pions emitted only to its acceptance region of the west central spectrometer. The pions of each MC events were embedded into a real event which was randomly selected from peripheral to central collisions, then pion pairs were assembled in the same manner as that of real data. The multiplicity dependence of the two-track detection efficiency of DCH, $\varepsilon_{multi}(\Delta\phi_{\rm DCH})$, is defined as:

$$\varepsilon_{multi}(\Delta\phi_{\rm DCH}) = \frac{A^{\rm MC}_{embed}(\Delta\phi_{\rm DCH})/A^{\rm MC}(\Delta\phi_{\rm DCH})}{B^{\rm MC}_{embed}(\Delta\phi_{\rm DCH})/B^{\rm MC}(\Delta\phi_{\rm DCH})}. \tag{4.10}$$

where $A^{\rm MC}$ and $B^{\rm MC}$ are signal and background pion pair distributions without embedding, respectively, and $A^{\rm MC}_{embed}$ and $B^{\rm MC}_{embed}$ are those after embedded into real data. The numerator $A^{\rm MC}_{embed}/A^{\rm MC}$ corresponds to the multiple track detection efficiency for signal pion pairs, and the dominator $B^{\rm MC}_{embed}/B^{\rm MC}$ corresponds to that for background pion pairs. The multiple track detection efficiencies are shown by Fig. 4.9, where MC events were embedded into real data for $0-30\%$ centrality and 2-σ matching cuts have been applied. In case of a matching to EMCal as shown by the left panel, the multiple track detection efficiency of DCH is about 0.9 and it gently decreases as $\Delta\phi_{\rm DCH}$ decreases. In two-particle analysis, a multiple track detection inefficiency for single-particle can be cancelled by dividing by its background pair distribution, $B^{\rm MC}_{embed}/B^{\rm MC}$, as described in the denominator in Eq. 4.10 and as shown by open red points in Fig. 4.9 (left).

The multiple track reconstruction efficiency, ε_{embed}, of pion pairs is shown in the right panel in Fig. 4.9. For the efficiency correction of various data set from central to peripheral collisions, we estimate the multiple track reconstruction efficiencies for 0-20%, 20-50% and 50-93% centralities, as shown in the left panel of Fig. 4.10. The efficiency $\varepsilon_{embed}(\Delta\phi_{\rm DCH})$ for 50-93% centrality is almost unity because the track multiplicity is negligibly small in the peripheral events. The total two-track detection efficiency of DCH can be determined as:

$$\varepsilon_{total}(\Delta\phi_{\rm DCH}) = \varepsilon_{mix}(\Delta\phi_{\rm DCH}) \times \varepsilon_{embed}(\Delta\phi_{\rm DCH}), \tag{4.11}$$

Fig. 4.10 right shows $\varepsilon_{total}(\Delta\phi_{\rm DCH})$ for 3 different centralities.

4.3.4 Two-track detection efficiency at EMCal

Two-track detection efficiency of EMCal was estimated in the same manner as that of DCH. For EMCal, the efficiencies are determined as a function of the relative separations of the distance ($\Delta R_{\rm EMC}$) of hit positions of pion pairs, and the total efficiency is expressed as:

$$\varepsilon_{total}(\Delta R_{\rm EMC}) = \varepsilon_{mix}(\Delta R_{\rm EMC}) \times \varepsilon_{multi}(\Delta R_{\rm EMC}), \tag{4.12}$$

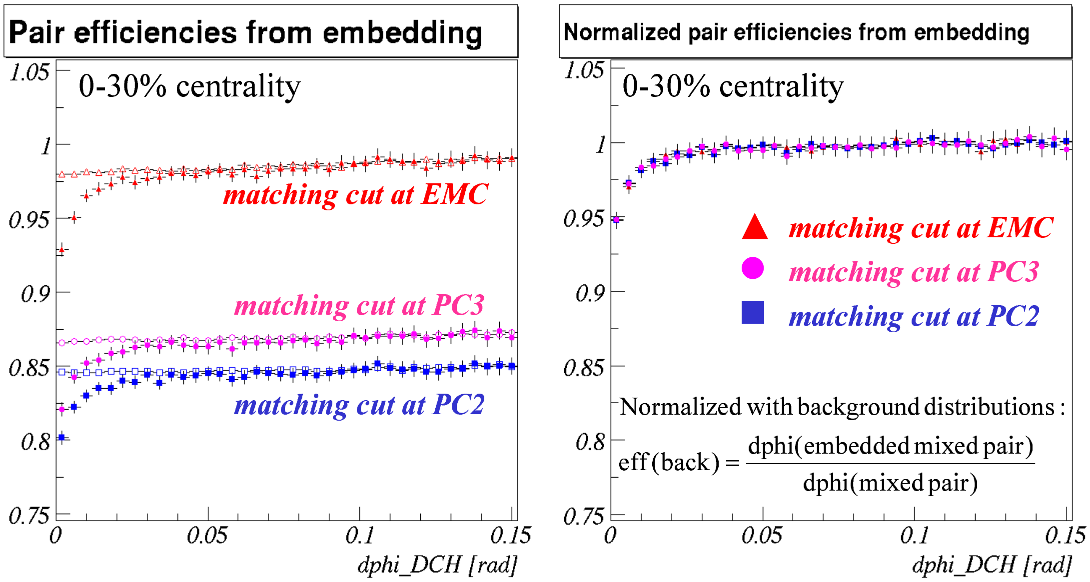

Figure 4.9: The left panel shows pair reconstruction efficiencies as a function of $\Delta\phi_{\rm DCH}$ for signal (filled symbols) and background (open symbols) pairs estimated by embedding for the top 30% centrality. The right panel shows the normalized pair reconstruction efficiencies.

where $\Delta R_{\rm EMC}$ defined as:

$$\Delta R_{\rm EMC} = \sqrt{(x_{clus1} - x_{clus2})^2 + (y_{clus1} - y_{clus2})^2 + (z_{clus1} - z_{clus2})^2}. \tag{4.13}$$

The two-track detection efficiency of EMCal in low multiplicity event $\varepsilon_{mix}(\Delta R_{\rm EMC})$ was estimated by using the same data set as one used for the estimate of $\varepsilon_{mix}(\Delta\phi_{\rm DCH})$, which is defined as:

$$\varepsilon_{mix}(\Delta R_{\rm EMC}) = A^{\rm MC}(\Delta R_{\rm EMC})/B^{\rm MC}(\Delta R_{\rm EMC}) \times norm., \tag{4.14}$$

where the background pair distribution, $B^{\rm MC}$, is normalized to the yield of the signal pair distribution, $A^{\rm MC}$, at $\Delta R_{\rm EMC} > 20$ cm.

The multiple track detection efficiency of EMCal $\varepsilon_{multi}(\Delta R_{\rm EMC})$ was estimated by using the same data set as one used for the estimate of $\varepsilon_{embed}(\Delta\phi_{\rm DCH})$, which is defined as:

$$\varepsilon_{multi}(\Delta R_{\rm EMC}) = \frac{A^{\rm MC}_{embed}(\Delta R_{\rm EMC})/A^{\rm MC}(\Delta R_{\rm EMC})}{B^{\rm MC}_{embed}(\Delta R_{\rm EMC})/B^{\rm MC}(\Delta R_{\rm EMC})}. \tag{4.15}$$

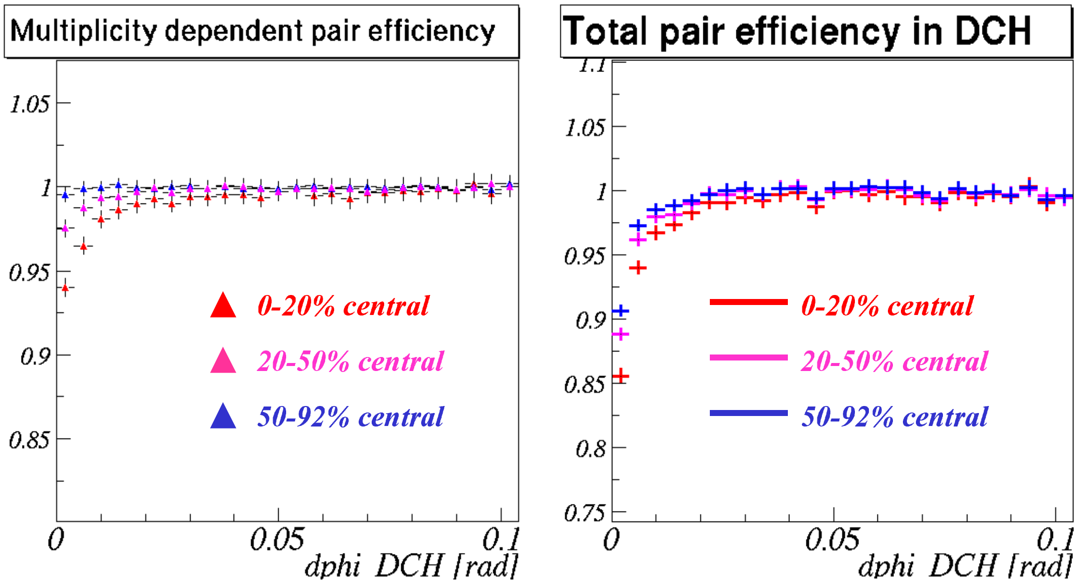

Figure 4.10: Multiplicity dependent pair reconstruction efficiencies $\varepsilon_{multi}(\Delta\phi_{\mathrm{DCH}})$ for 0-20%,20-50% and 50-93% centrality classes (left), and total pair reconstruction efficiencies $\varepsilon_{total}(\Delta\phi_{\mathrm{DCH}})$ (right).

Estimated $\varepsilon_{multi}(\Delta R_{\mathrm{EMC}})$ for different centrality classes are shown in the Fig. 4.11. Since the $\varepsilon_{multi}(\Delta R_{\mathrm{EMC}})$ doesn't show a significant inefficiency beyond its statistic error even for the central collision. we define the total two-track detection efficiency at EMCal as:

$$\varepsilon_{total}(\Delta R_{\mathrm{EMC}}) = \varepsilon_{mix}(\Delta R_{\mathrm{EMC}}). \tag{4.16}$$

Finally, the correlation function including the correction for its two-track detection inefficiency was obtained as:

$$C_2^{raw}(\Delta\phi_{\mathrm{DCH}}, \Delta R_{\mathrm{EMC}}) = \frac{C_2^{measure}(\Delta\phi_{\mathrm{DCH}}, \Delta R_{\mathrm{EMC}})}{\varepsilon_{total}(\Delta\phi_{\mathrm{DCH}}) \cdot \varepsilon_{total}(\Delta R_{\mathrm{EMC}})}. \tag{4.17}$$

4.3.5 Two-track qualification cuts

Fig. 4.12 shows the intensity of positive pions of real data normalized by the background pairs as a function of $\Delta\phi_{\mathrm{DCH}}$ and ΔZ_{DCH}. As shown by the left panel, there is a significant suppression of the detection efficiency for pion pairs in a small $\Delta\phi_{\mathrm{DCH}}$ and ΔZ_{DCH} region. Also the right panel shows a steep rise in a small $\Delta\phi_{\mathrm{DCH}}$ and ΔZ_{DCH} region due to ghost

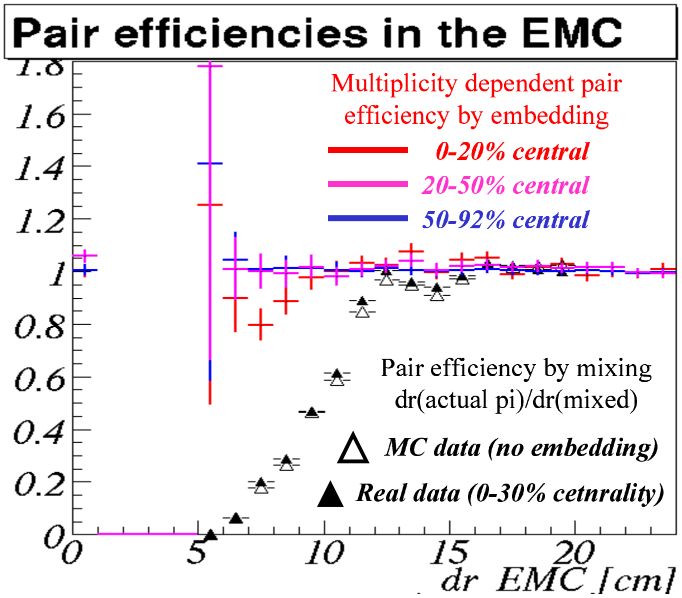

Figure 4.11: Two-track detection efficiencies of EMCal. The two-track detection efficiency in low multiplicity event ($\varepsilon_{mix}(\Delta R_{\rm EMC})$) is shown by open triangle. Multiple track detection efficiency ($\varepsilon_{multi}(\Delta R_{\rm EMC})$) of simulated pion pairs for 0-20% (red), 20-50% (purple) and 50-93% (blue) centralities. The $\Delta R_{\rm EMC}$ distribution of positive pions of real data is shown by filled triangle.

tracks. To avoid the significant suppression region and ghost tracks, we applied following two-track qualification cuts to both signal and background pairs.

$$\Delta Z_{\rm DCH} > 1.0\ cm\ \ ``OR''\ \ \Delta\phi_{\rm DCH} > 0.06\ rad, \Delta Z_{\rm DCH} > 5.0\ cm\ \ ``OR''\ \ \Delta\phi_{\rm DCH} > 0.03\ rad. \tag{4.18}$$

As described in the previous section, the two-track detection inefficiency as a function of $\Delta\phi_{\rm DCH}$ was corrected by using MC simulation. In addition to the correction, we applied a two-track qualification cut to both signal and background pairs as:

$$\Delta\phi_{DC} > 0.005\ rad. \tag{4.19}$$

because a strong suppression of the yield of signal pairs compared to that of background pairs still remains in the very small $\Delta\phi_{\rm DCH}$ region even after the inefficiency correction by MC.

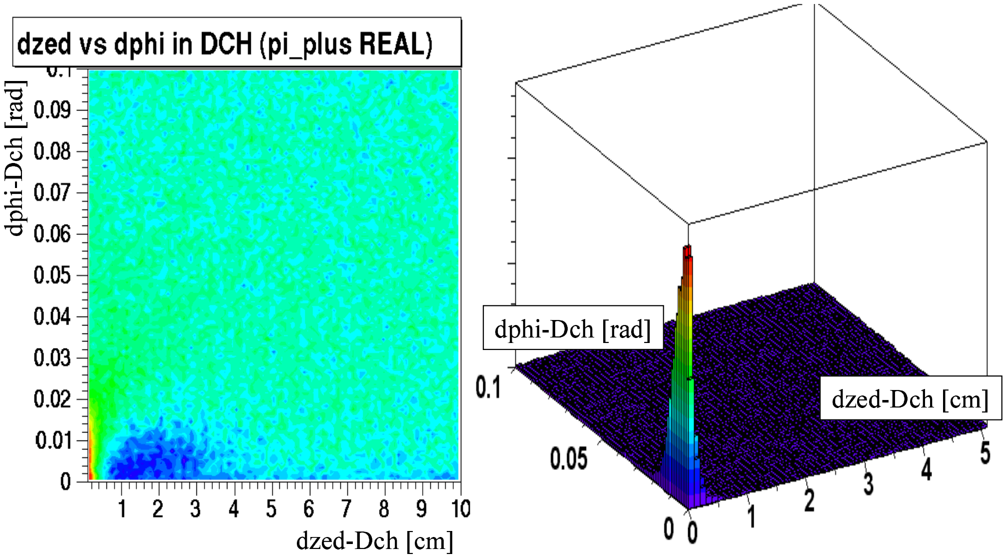

Figure 4.12: Relative separations of positive pion pairs in $\Delta\phi_{\text{DCH}}$ versus ΔZ_{DCH} (left) and its lego plot (right). The pair distribution is statistically normalized by the background pair distribution.

As shown by Fig. 4.11, the intensity of pion pairs measured by EMCal drops at a small ΔR_{EMC} less than 15 cm and is completely suppressed less than 6 cm due to the cluster sharing with nearby tracks. Although the inefficiency was corrected by using the MC simulation, in case the statistics error of MC data became significant at a small ΔR_{EMC}. To avoid such a significant statistical error, we required a two-track qualification cut to both signal and background pairs as:

$$\Delta R_{\text{EMC}} > 8.0\ cm \tag{4.20}$$

The total number of charged pion pairs utilized in this analysis are summarized in Table 4.1.

Chapter 5

Coulomb Interaction

Two different types of Coulomb corrections and fitting methods for charged pion pairs are explained. An unlike-sign correlation function ($\pi^+\pi^-$) and a simulation study for the Coulomb correction are presented. The total systematic error, mainly originates from the Coulomb and two-track detection efficiency corrections described in the last chapter, is described in the last section of this chapter.

5.1 The conventional Coulomb correction

5.1.1 Coulomb strength estimation

Any final state interactions (FSI), most likely due to Coulomb force between adjacent charged tracks, degenerate the Bose-Einstein correlation. The repulsive Coulomb force between like-sign pairs disturbs its relative momentum and strongly suppresses its yield at the relative momentum $\mathbf{q} = \mathbf{p}_1 - \mathbf{p}_2 \sim 0$, and the effect has to be removed from the Bose-Einstein correlation. Since it is too complicate to solve a multi-body Coulomb effect, we can approximately evaluate the suppression factor of pair in the relative momentum $\mathbf{q}$ based upon two-body Coulomb effect, and remove the contribution of the Coulomb effect from the correlation function.

If we know the quantum information of the particle source, we basically can calculate the Coulomb effect, but we are not able to know all the quantum information of the source in realistic methods. Therefore I assume a geometrical source volume first, and then calculate the Coulomb strength of each pair in the volume by using the Coulomb wave function integration method [49]. The detailed description of the Coulomb wave function can be found in the appendix of a text book written by Messiah [50]. In the correction method, a Gaussian source volume is assumed from HBT radius parameters, which is evaluated beforehand. Then, initial space points of each pair are randomly determined according to the Gaussian distribution. With a measured relative momentum and the initial space separation of the pair, a probability amplitude is calculated by using two-track wave function with Coulomb term, and normalized by an alternative probability amplitude calculated without the Coulomb term. For the accuracy, the probability amplitude is integrated and averaged over several points on the Gaussian distribution. The normalized probability amplitude corresponds to the suppression factor for each pair. 20 sampling points are averaged over for speeding up of the calculation but the evaluated Coulomb strength is consistent with that of 100 sampling points within 1%.

5.1.2 Outline of Coulomb correction procedure

Coulomb correction is necessary for the extraction of the HBT radius, while the calculation of the Coulomb wave function requires the HBT radius for its input parameter. To solve this issue, an "iterative" Coulomb correction method is used here. At the first process of the iterative Coulomb correction, each pair is applied to the Gamov Coulomb correction, which is the limit of the Coulomb wave function for a point-like source defined as:

$$C_{gamov} = \frac{2\pi\eta}{e^{2\pi\eta} - 1} \qquad (\eta = m\alpha/\mathbf{q}) \,, \tag{5.1}$$

where η is comprised of an ideal pion mass m, the fine structure constant, α, and the relative momentum of pair, $\mathbf{q}$. Then, the 1-dimensional and 3-dimensional Bose-Einstein correlation function with the Gamov Correction is fitted to Eq. 2.11 and Eq. 2.15, respectively, providing a roughly estimated HBT radii. At the next step, Coulomb effect on each pair is further precisely evaluated by using the Coulomb wave function assuming a finite volume, which is obtained from the previous step. The iterative Coulomb correction lasts until the output HBT radius become consistent with the input HBT radius within an acceptable accuracy.

In the traditional Coulomb correction method, which has been used over the past several years in Bose-Einstein correlation analyses, all like-sign pairs are uniformly applied to the Coulomb correction described above. The correction method is called "*full*" Coulomb correction hereafter. To compare with those results, I also utilize the *full* Coulomb correction method. This *full* Coulomb correction procedure and the calculation code used in this analysis have been built based upon the Coulomb correction algorithm used by NA44 experiment [27]. The correction method, for the 1-dimensional analysis, requires the one-dimensional HBT radius, $R_{\rm inv}$, and an invariant relative momentum, $q_{\rm inv}$. For the 3-dimensional analysis, the Bertsch-Pratt radius parameters, $R_{\rm side}$, $R_{\rm out}$ and $R_{\rm long}$, in the LCMS frame are utilized as input parameters, then calculates the Coulomb strength of each pair using corresponding 3-dimensional relative momenta, $q_{\rm side}$, $q_{\rm out}$ and $q_{\rm long}$. Fig. 5.1 shows the 1-dimensional Coulomb correlation as a function of $q_{\rm inv}$, estimated from the ratio of the $q_{\rm inv}$ distribution for $\pi^+\pi^+$ with the *full* Coulomb correction to the same distribution without any Coulomb correction. The Coulomb effect can be seen at low $q_{\rm inv}$ region less than 100 MeV/c.

For a cross check, I also used the Coulomb correction code which was developed by AGS-E866 experiment [24]. In the E866-type's *full* Coulomb correction, the Coulomb interaction of pairs is corrected in the pair center-of-mass frame, which just requires the one-dimensional parameters, $R_{\rm inv}$ and $q_{\rm inv}$. The Coulomb correction factors calculated by these two codes are quite consistent with one another, and the systematic error on the resulting HBT radius parameters depending on the correction frame is less than 1%.

5.2 New Coulomb correction

5.2.1 Contribution from Long-live particles

In RHIC energies, lots of heavier particles and resonances could be produced in collisions more than those at AGS-SPS energies, and therefore, some pions could be decay products

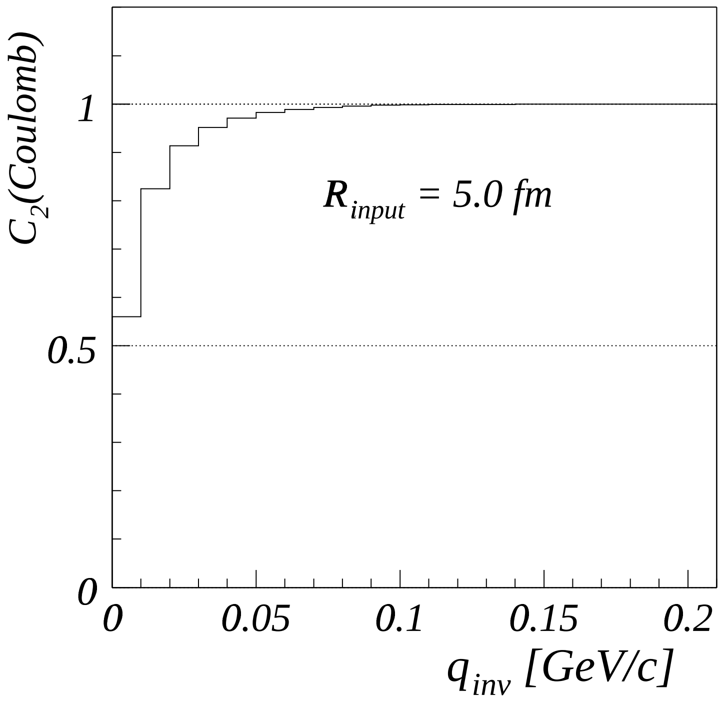

Figure 5.1: A histogram of Coulomb correlation as a function of $q_{\rm inv}$, estimated by the *full* Coulomb correction with a input source size of 5 fm using $\pi^+\pi^+$ for $k_{\rm T} = 0.2 - 2.0$ GeV.

of long-lived particles, such as η, η' and K^*. Those pions, which are produced mostly out of the HBT radius, may experience a negligibly small Coulomb force from another like-sign pions. Thus, the *full* Coulomb correction, in which all pions are assumed to be produced in a well localized source within the given HBT radius parameters, is considered to be unable to deal with the Coulomb correction properly for such long-lived particles, and could be a somewhat excessive evaluation.

To evaluate how much Coulomb strength (λ_{+-}) contribute to the correlation function in the real data, I measured the unlike-sign ($\pi^+\pi^-$) correlation function using the same data sample as the like-sign correlations. The $\pi^+\pi^-$ correlation function is expected to be affected by the Coulomb effect but not by the Bose-Einstein correlation. Fig. 5.2 shows 1-dimensional $\pi^+\pi^-$ correlation function for $k_{\rm T} = 0.2 - 2.0$ GeV/c at the most $0 - 30\%$ central collision. The overlaid histograms are Coulomb correlation functions, which are estimated in the same way as for Fig. 5.1, for 3 different partialities [%] of Coulomb correction. Here, the percentage of Coulomb correction means the proportion of the number of corrected pairs to the total pairs, namely 100% and 0% partial Coulomb correction corresponds to the *full* and no Coulomb correction.

To compare the Coulomb attractive force of the unlike-sign pion, the calculated Coulomb correlation functions are reversed around unity. A chi-square test between the $\pi^+\pi^-$ correlation function and the "reversed" Coulomb correlation functions varied from 0% to 100% partiality, yields the fraction of partial Coulomb strength λ_{+-} to be 0.50 ± 0.04 with $\chi^2/DoF = 3.0$. In this fitting test, I removed the lowest $q_{\rm inv}$ bin (<10 MeV) where the difference of Coulomb effects between like-sign and unlike-sign pairs becomes significant [33]. This evaluation indicates that the *full* Coulomb correction, in which $\lambda_{+-} = 1.0$ is assumed, could be an excessive correction method in RHIC energies.

5.2.2 Coulomb correction based on core-halo model

A new Coulomb correction based upon a picture of the "core-halo" source structure is being recently developed by Sinyukov [33] for a realistic Coulomb correction rather than the *full* Coulomb correction for charged pions in relativistic heavy-ion collisions.

Charged pions originated from long-lived particles experience negligibly small Coulomb forces comparing to pions emitted from the well localized "core" source. Also they obviously do not contribute to the Bose-Einstein correlation function of the core source. In other words, they form a "halo" structure which is much larger (e.g. ∼40 fm) than that of the core source, and the Bose-Einstein enhancement of the halo structure make a very narrow peak at $\mathbf{q} \sim 0$. Since such a narrow correlation function can not be resolved by the experimental momentum resolution, it may contribute only to the λ parameter [34]. In the picture of core-halo structure of source, the λ parameter can be parameterized [51] as:

$$\lambda = (N_c/(N_c + N_h))^2 \tag{5.2}$$

where N_c is the number of core pions which directly emitted from the source or originated

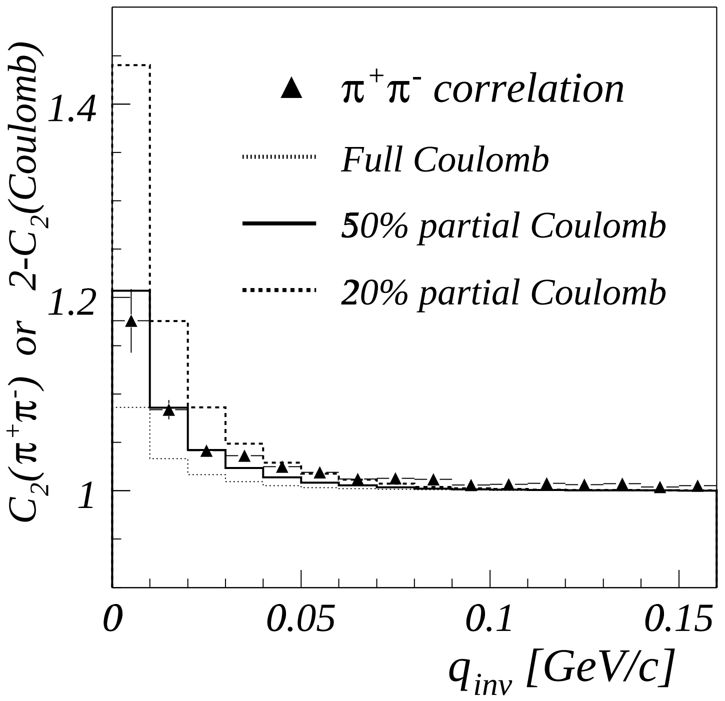

Figure 5.2: One-dimensional correlation function of unlike-sign pion pairs ($\pi^+\pi^-$) for $k_\mathrm{T} = 0.2 - 2.0$ GeV/c at the top 30% centrality. Overlaid histograms correspond to the Coulomb correlation functions for 20% (dotted) and 50% (solid) partial Coulomb corrections, and the *full* Coulomb correction (dashed), which are reversed around unity.

from short-lived resonances particles, while N_h is the number of halo pions originated from long-lived resonances and particles.

In this new Coulomb correction method, the Gaussian fit function is decomposed into the core and halo parts as defined by:

$$\begin{aligned} C_2(\mathrm{raw}) &= C_2(\mathrm{core}) + C_2(\mathrm{halo}) \\ &= [\lambda(1+G_\mathrm{BE})]F_\mathrm{coul} + [1-\lambda], \end{aligned} \tag{5.3}$$

where

$$F_\mathrm{coul} = \omega(k_\mathrm{T})(F_\mathrm{coulomb}(q_\mathrm{inv}) - 1) + 1, \tag{5.4}$$

$$\omega(k_\mathrm{T}) = \lambda_\mathrm{ideal}/\lambda \qquad \text{and} \tag{5.5}$$

$$G_\mathrm{BE} = exp(-{R_\mathrm{inv}}^2 {q_\mathrm{inv}}^2)$$

$$= \quad exp(-{R_{\mathrm{side}}}^2{q_{\mathrm{side}}}^2 - {R_{\mathrm{out}}}^2{q_{\mathrm{out}}}^2 - {R_{\mathrm{long}}}^2{q_{\mathrm{long}}}^2). \tag{5.6}$$

F_{coul} is the *full* Coulomb correction term as a function of q_{inv}, and is applied only to the core part. A complementary 3-dimensional histogram as a function of q_{side}, q_{out} and q_{long}, which contains mean q_{inv} values in each of the 10 MeV/c bins, is prepared for the correction of the 3-dimensional correlation function. The $F_{\mathrm{coulomb}}(q_{\mathrm{inv}})$ is derived from the ratio of $\pi^+\pi^+$ distribution as a function of q_{inv} with no Coulomb correction to the same histogram of $\pi^+\pi^+$ with the *full* Coulomb correction, which is just reverse of Fig. 5.1. The momentum smearing effect on the Coulomb correlation function is already taken into account in $F_{\mathrm{coulomb}}(q_{\mathrm{inv}})$. In addition, the Coulomb correlation function, which can be scaled with λ parameter, is suppressed by the finite momentum resolution on the measured λ parameter. The correction factor, $\omega(k_{\mathrm{T}})$, is evaluated from the ratio of the ideal λ parameter (λ_{ideal}) without momentum resolution to the measured λ parameter with finite momentum resolution, as defined in Eq. 5.6. In this analysis, $\omega(k_{\mathrm{T}})$ is estimated by using simulated Bose-Einstein correlation with MC detector simulation described below.

5.3 Systematic error by Coulomb correction

The new Coulomb correction would cause systematic errors on resulting HBT radii due to a momentum resolution effect on the λ parameter and a contribution from intermediate-lived particles such as ω. These systematic errors can be estimated by using MC simulation and an alternative Coulomb correction method.

5.3.1 Momentum resolution effect

The new Coulomb correction defined by Eq. 5.3 requires the ideal λ parameter, λ_{ideal}, which does not suffer from any experimental resolution. In a realistic experimental condition, however, the λ value is slightly suppressed by a finite momentum resolution. The correction factor, $\omega(k_{\mathrm{T}})$, incorporated in the new Coulomb correction as defined by Eq. 5.6, can be estimated by using MC detector simulator.

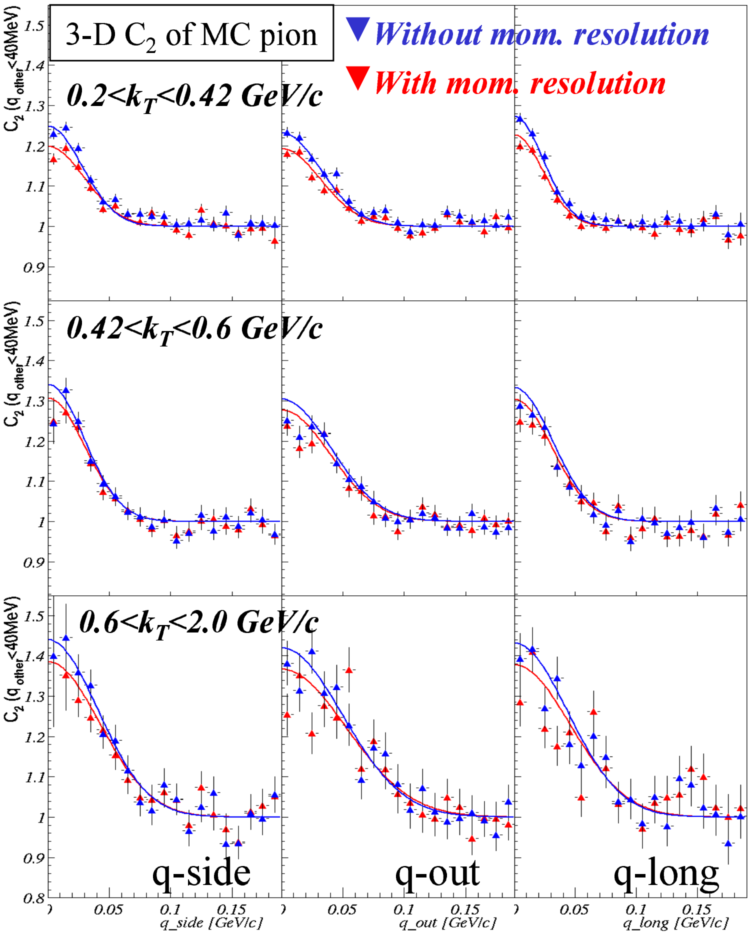

Figure 5.3: Simulated Bose-Einstein correlation functions of MC positive pion pairs for 3 different k_{T} bins, 0.20−0.42 GeV/c (top), 0.42−0.60 GeV/c (middle) and 0.60−2.00 GeV/c (bottom), as a function of q_{side} (left), q_{out} (center) and q_{long} (right). The red and blue points are obtained with and without a finite momentum resolution.

I used the same simulation data sample as one used for the pair efficiency correction, described in section 4.3, for $\omega(k_{\mathrm{T}})$ estimate. Since the momentum resolution essentially gets worse as k_{T} increases, the $\omega(k_{\mathrm{T}})$ might depend on k_{T} accordingly. To investigate the k_{T} dependence of $\omega(k_{\mathrm{T}})$, I divide the data sample of pion pairs into 3 different k_{T} bins, 0.20−0.42, 0.42−0.60 and 0.60−2.00 GeV/c. Each pion pair is weighted by the Bose-Einstein enhancement, which is approximately evaluated based on Eq. 2.11 with its relative momentum $\mathbf{q}$ and an input HBT radius parameter. The input HBT radius parameter is obtained from the fit of the correlation function of real data measured in

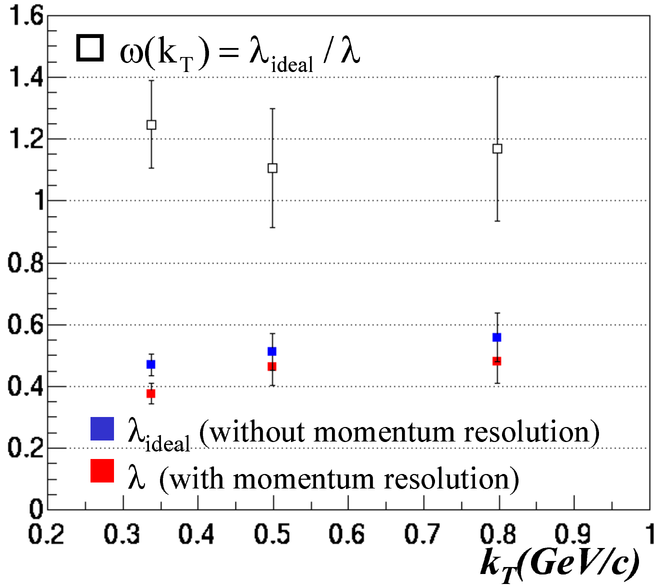

Figure 5.4: Fitted λ parameters with and without a finite momentum resolution for 3 different k_T bins. The correction factor $\omega(k_\mathrm{T})$, which is defined as the ratio of these λ parameters, is shown by open square.

similar k_T region. Fig. 5.3 shows the 3-dimensional Bose-Einstein correlation function of positive pion pairs obtained from the MC simulation for the 3 k_T bins. The 3-dimensional correlation function is projected onto q_side, q_out and q_long directions for the orthogonal components less than 40 MeV/c. Compared to the ideal correlation function without finite momentum resolution (blue symbol), the correlation functions after reconstructed by the detector simulator with a finite momentum resolution is slightly suppressed (red symbol).

Fig. 5.4 shows the fitted λ parameters w/o the momentum resolution as a function of k_T. The suppression factor $\omega(k_\mathrm{T})$, which is estimated from the ratio of those λ parameters, is about 1.2 and less sensitive to k_T in the measured momentum range owing to the good momentum resolution at PHENIX. The $\omega(k_\mathrm{T})$ derived from the MC simulation is still consistent with unity within the statistical error. Therefore, the $\omega(k_\mathrm{T})$ is set to 1 in this analysis and the contribution from the finite the momentum resolution is included as a systematic error due to the new Coulomb correction, which is evaluated from differences of resulting HBT radii between with ($\omega(k_{\mathrm{T}}) \sim 1.2$) and without ($\omega(k_{\mathrm{T}}) = 1$) the momentum resolution.

5.3.2 Another new idea of Coulomb correction

The new Coulomb correction based on a core-halo structure assumes that Coulomb effects for pairs in the halo part are negligibly small. In order to test the underlying hypothesis of the new Coulomb correction, I fit the strength of the Coulomb interaction (λ_{+-}) to the unlike-sign correlation function and obtained a value for $\lambda_{+-} \sim 0.50$, as described above. This value is clearly inconsistent with the *full* strength Coulomb correction, but it is also significantly greater than the value of λ. I attribute this difference to the ω resonance, which is sufficiently long-lived to be unresolved with Bose-Einstein correlations, but may contribute significantly to the Coulomb interaction.

To account for this contribution, I suggest an alternative formula to Eq. 5.3, in which the total Coulomb strength is fixed at $\lambda_{+-} = 0.5$, but the fraction of pairs which contribute to both Bose-Einstein and Coulomb effects are allowed to vary to fit the data, as defined by:

$$\begin{aligned} C_2(\mathrm{raw}) &= C_2(\mathrm{core}) + C_2(\mathrm{Coulomb-only}) + C_2(\mathrm{halo}) \\ &= [\lambda(1+G_{\mathrm{BE}})]F_{\mathrm{coul}} + [\lambda_{+-} - \lambda]F_{\mathrm{coul}} + [1-\lambda_{+-}] \end{aligned} \tag{5.7}$$

In applying this formula, I still calculate the additional Coulomb fraction using the Bertsch-Pratt source of approximately 5 fm, rather than estimating the larger source distribution for the ω decay products. Therefore I use this formula to provide an upper bound on the effect of the additional Coulomb interaction.

The difference of resultant HBT radius parameters obtained from fits to Eq. 5.3 and Eq. 5.7 are included as a systematic error of the partial Coulomb correction.

5.4 Total systematic error

Here, I explain the remaining systematic errors except the systematic error due to the Coulomb correction, and the corresponding total systematic errors. Any other final-state strong interaction except for the Coulomb effect is not corrected because it is expected to be negligibly small compared to the Coulomb interaction [52]. Each and the total systematic errors on the HBT radius parameters are summarized in Table 5.1. For its detailed study, the total systematic errors are estimated for each of nine k_{T} and nine centrality classes, as shown by 5.5.

- **Pair separation cuts.**

  The uncertainty of the resultant radius parameters originated by pair separation cuts is not negligible. Since the reconstruction inefficiency of pairs basically appears at its low relative separation region in which the HBT effect also significant, the separation cuts for pairs at low relative separation obviously degenerates the Bose-Einstein enhancement. I evaluate the systematic errors due to the pair separation cuts by varying the cut conditions.

  For example, the applied nominal separation cut for EMCal is $\Delta R_{EMC} > 8.0\ cm$. In case, I apply a separation cut which is twice as large as the nominal separation pair cut, as defined by $\Delta Z_{EMC} > 16.0\ cm$. Then, the systematic errors of HBT radii due to the pair separation cut are estimated from the differences of resultant HBT radii between above two cuts. Also a similar estimate of the systematic error is performed for the pair separation cuts at DCH.

- **MC corrections.**

  The inefficiencies of two-track detection with DCH and EMCal have been corrected by using GEANT-based MC simulation. Due to the finite statistics of MC data, however, those inefficiency corrections also have statistical uncertainties. I account the statistical uncertainty of the the two-track detection inefficiency corrections

systematics [%]	λ_{inv}	R_{inv}	λ	R_{side}	R_{out}	R_{long}	$R_{\text{out}}/R_{\text{side}}$
Mom. resolution on λ	6.35	1.15	5.38	2.02	0.92	1.66	2.93
Intermediate resonance	13.32	2.03	5.49	1.71	1.80	1.72	3.52
Pair cut for DCH	6.85	3.66	6.77	1.60	3.13	4.33	1.85
Pair cut for EMCal	4.18	1.68	3.13	1.33	0.86	1.69	1.15
MC correction for DCH	2.13	1.99	1.02	1.57	3.25	3.94	4.82
MC correction for EMCal	1.13	0.24	1.05	0.28	0.33	0.75	0.61
Residual HBT effect	0.55	1.35	0.36	1.57	1.66	1.55	0.30

Table 5.1: Systematic errors of the one-dimensional and three-dimensional (Bertsch-Pratt) radius parameters in the LCMS. Errors are expressed as a percentage of the measured radius parameters.

by MC as a systematic error. I artificially varied the correction factors within the statistical errors, then the systematic errors is evaluated from the maximum differences of resulting HBT radii obtained in the variation.

- **Residual HBT effect.**

  In case of a small acceptance detector, a residual Bose-Einstein correlation effect in each single track is not negligible [23], and it contaminates each track of the background pairs. In NA44's analysis [27], the residual HBT effect was estimated and corrected by applying HBT weight to background pairs randomly by using real event. Also in this analysis, I estimated the residual HBT effect by using the same algorithm as NA44's method, and the systematic error of residual HBT is estimated from the difference of resultant radius parameters between w/o the residual correction code.

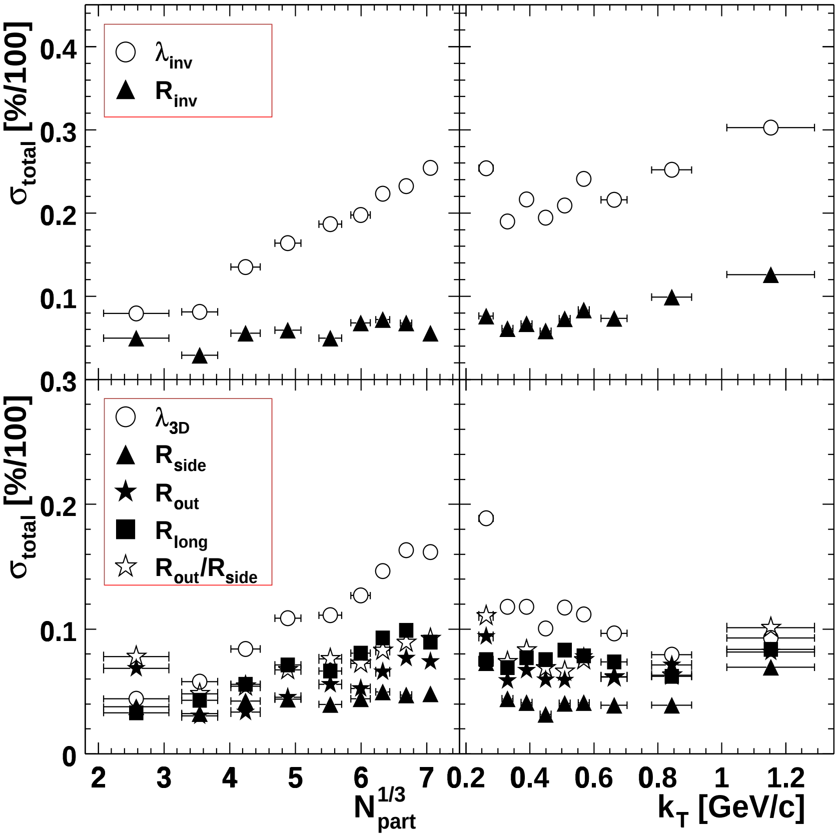

Figure 5.5: Total systematic errors on one-dimensional radius parameters (top) and Bertsch-Pratt radius parameters (bottom) as a function of ${N_{\mathrm{part}}}^{1/3}$ (left) and k_{T} (right).

Chapter 6

Results and discussions

In this chapter, results of one-dimensional and three-dimensional HBT radii for $\pi^+\pi^+$ and $\pi^-\pi^-$ at $\sqrt{s_{\rm NN}} = 200$ GeV in Au+Au collisions are shown as a function of three external independent parameters, the mean transverse momentum of pair, $k_{\rm T}$, and the number of participants, $N_{\rm part}$. In addition, the comparison of the HBT radii with those of earlier experiments shows those collision energy dependence. The detailed description on the systematic errors of the HBT radii are in the last section.

6.1 Collision energy dependence

I present one-dimensional and three-dimensional correlation functions and the resulting HBT radii. The three-dimensional HBT radii are compared to those of earlier experimental results to investigate the collision energy dependence. All of the HBT radii presented in this section are obtained with the traditional *full* Coulomb correction.

6.1.1 One-dimensional correlation function

The Bose-Einstein correlation function is experimentally measured by the ratio of the two-particle inclusive cross section to the product of the two single particle cross sections. In case of pion pair, the correlation function is defined as:

$$C_2(\mathbf{p}_1, \mathbf{p}_2) \;\; = \;\; N\left(\sigma_\pi \frac{d^6\sigma_\pi}{d^3p_1 d^3p_2}\right) \Big/ \left(\frac{d^3\sigma_\pi}{d^3p_1}\frac{d^3\sigma_\pi}{d^3p_2}\right)$$

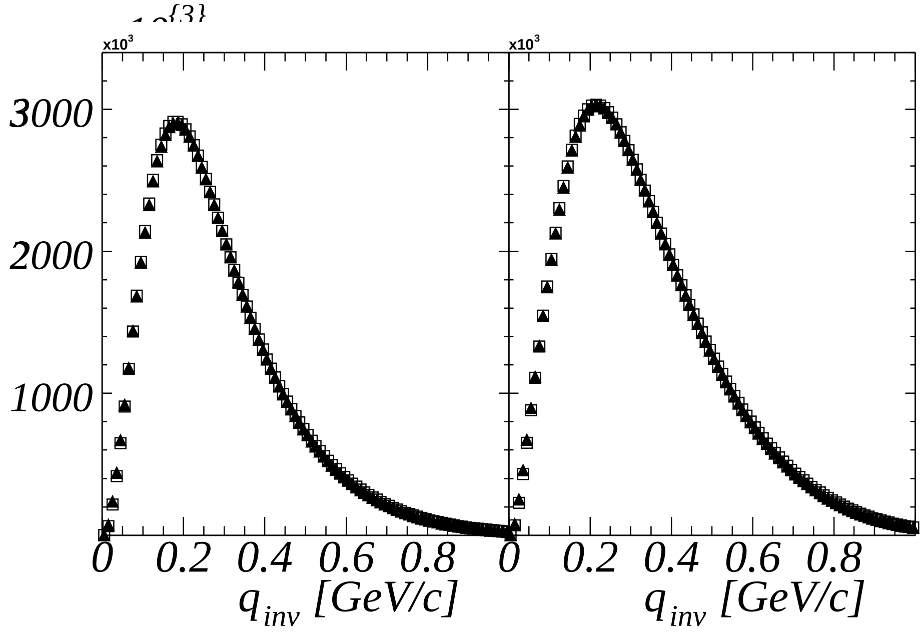

Figure 6.1: q_{inv} distributions of signal pairs (filled triangle) and background pairs (open square) for $\pi^+\pi^+$ (left) and $\pi^-\pi^-$ (right) with no Coulomb correction. Each distribution of background pairs is normalized to the yield of its signal pairs.

$$= \frac{A(\mathbf{q})}{B(\mathbf{q})} \tag{6.1}$$

where N is the normalization factor and $A(\mathbf{q})$ is the intensity of signal pairs at a relative 4-vector momentum, $\mathbf{q}$ $(= \mathbf{p}_1 - \mathbf{p}_2)$, and $B(\mathbf{q})$ is the background pair distribution obtained from mixed events. The detailed procedure to make signal and background pairs has been described in section 4.2.4. Here, I introduce a Lorentz-invariant relative momentum, q_{inv}, given by Eq. 2.12, for the analysis of the one-dimensional correlation function. Fig. 6.1 shows q_{inv} distributions of signal pairs (filled symbols) and background pairs (open symbols) for $\pi^+\pi^+$ (left) and $\pi^-\pi^-$ (right) pairs. The background pair distribution is normalized to the yield of signal pairs at the large q_{inv} region ($q_{\text{inv}} > 0.2$ GeV/c) where Bose-Einstein and Coulomb effects are negligible. The correction factors for the finite resolution of two-track reconstruction, which were evaluated by using MC detector simulation described in section 4.3, are subjected to the signal pair distributions. The ratio of the distribution of signal pairs to that of background pairs corresponds to the correlation function.

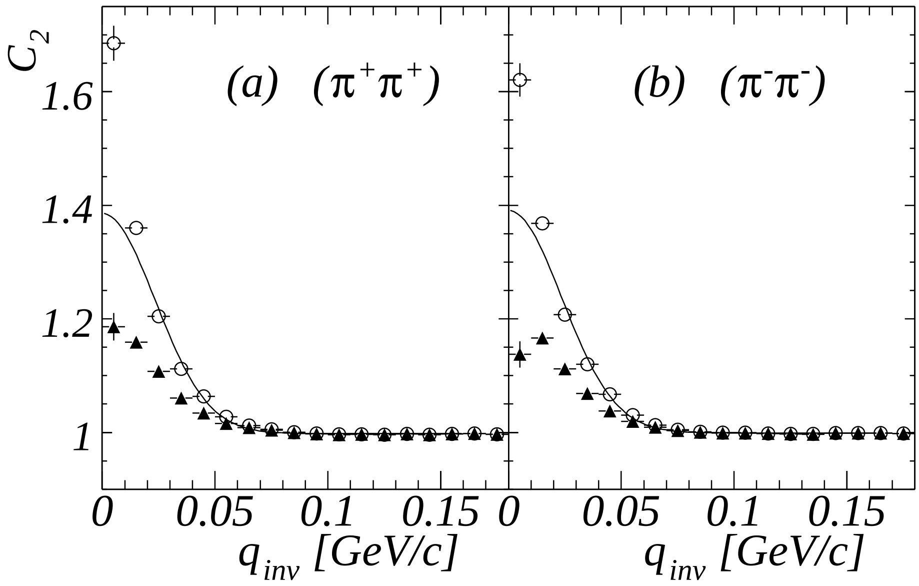

Figure 6.2: One-dimensional correlation functions of $\pi^+\pi^+$ (left) and $\pi^-\pi^-$ (right) as a function of $q_{\rm inv}$ for $k_{\rm T} = 0.2-2.0$ GeV/c ($\langle k_{\rm T}\rangle \sim 0.46$ GeV/c) for the top 30% centrality. The filled triangles show correlation functions with pair efficiency corrections but without any Coulomb correction, and the open circles show ones after the *full* Coulomb correction. The error bars are statistical only. The lines overlaid on the open circles correspond to fit of Eq. 2.11.

Fig. 6.2 shows the one-dimensional correlation functions of $\pi^+\pi^+$ (left) and $\pi^-\pi^-$ (right) pairs as a function of $q_{\rm inv}$, for the "semi-inclusive" $k_{\rm T}$ range from 0.2 to 2.0 GeV/c for the 0−30 % centrality of collisions. The mean $k_{\rm T}$ is estimated to be $\langle k_{\rm T}\rangle \sim 0.45$ GeV/c. Eq. 2.11 is utilized to fit one-dimensional correlation functions, yielding HBT radius parameters $\lambda_{\rm inv}$ about 0.4 and $R_{\rm inv}$ about 6 fm. The fit parameters are given in Table 6.1.

6.1.2 Three-dimensional correlation function

As described in chapter 2, I choose the Bertsch-Pratt parameterization for three-dimensional analysis, in which the relative momentum $\mathbf{q}$ is decomposed into sideward ($q_{\rm side}$), outward ($q_{\rm out}$) and longitudinal ($q_{\rm long}$) directions. Fig. 6.3 shows the three-dimensional correlation function as a function of $q_{\rm side}$ (left), $q_{\rm out}$ (center) and $q_{\rm long}$ (right) for $\pi^+\pi^+$ (top) and

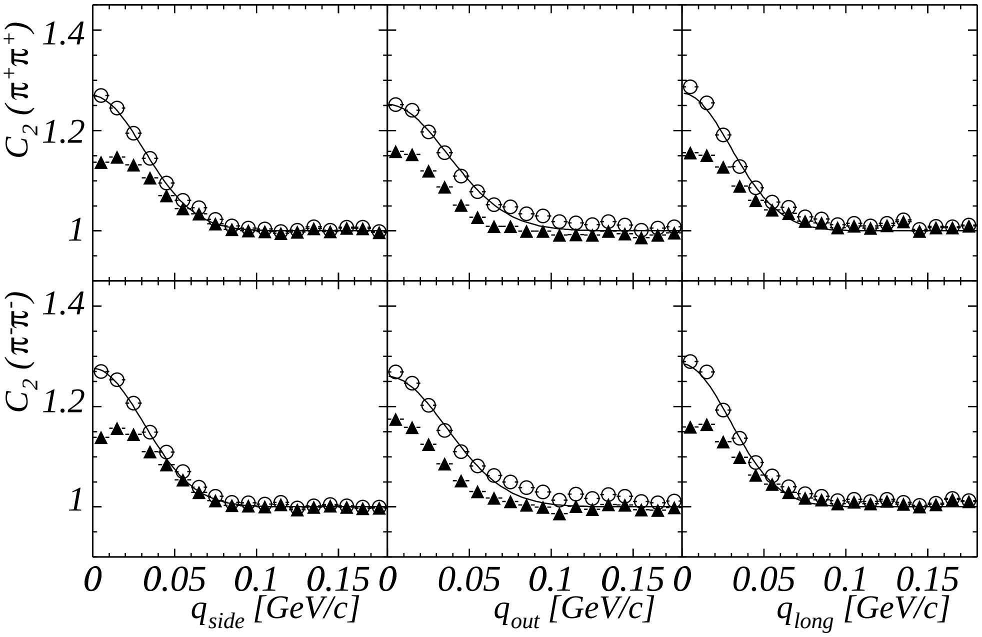

Figure 6.3: Three-dimensional correlation functions of $\pi^+\pi^+$ (top) and $\pi^-\pi^-$ (bottom) projected onto each direction, $q_{\rm side}$ (left), $q_{\rm out}$ (center) and $q_{\rm long}$ (right), for the orthogonal components of $\mathbf{q}$ less than 40 MeV/c. $k_{\rm T}$ is between 0.2 GeV/c and 2.0 GeV/c ($\langle k_{\rm T}\rangle \sim$ 0.46 GeV/c) for $0-30\%$ centrality. The filled triangles show correlation functions with pair efficiency corrections but without Coulomb correction, and the open circles show ones after the *full* Coulomb correction. The error bars are statistical only. The curves overlaid on the open circles show the 3-dimensional fit (Eq. 2.15) which is projected onto each direction, as well.

$\pi^-\pi^-$ (bottom) pairs at $k_{\rm T} = 0.2$–2.0 GeV/c for the 0–30 % centrality of collision. The projections of the 3-D correlation functions are averaged over the lowest 40 MeV in the orthogonal directions. For example, in case of the correlation function as a function $q_{\rm side}$, the other two variables, $q_{\rm out}$ and $q_{\rm long}$ are projected on $q_{\rm side}$ if $|q_{\rm out}|, |q_{\rm long}| < 40$ MeV/c. The filled triangles show the correlation functions with detector inefficiency corrections but without any Coulomb correction, and the open circles show those with the *full* Coulomb correction.

Eq. 2.15 is used to fit the three-dimensional correlation functions, yielding HBT (Bertsch-Pratt) radius parameters λ, $R_{\rm side}$, $R_{\rm out}$ and $R_{\rm long}$. The Bertsch-Pratt HBT radii, $R_{\rm side}$, $R_{\rm out}$ and $R_{\rm long}$ are around 4–5 fm, as shown by Table 6.2.

pair	$\lambda_{\rm inv}$	$R_{\rm inv}$	χ^2/DoF
$\pi^-\pi^-$	0.390±0.007	5.96±0.05	460/16
$\pi^+\pi^+$	0.394±0.007	5.91±0.05	364/16

Table 6.1: One-dimensional fit parameters by Eq. 2.11 for $\pi^+\pi^+$ and $\pi^-\pi^-$ for $k_{\rm T}$ = 0.2-2.0 GeV/c at the top 0-30% centrality. All radii are in fm, and errors are statistical only.

pair	λ	$R_{\rm side}$	$R_{\rm out}$	$R_{\rm long}$	χ^2/DoF
$\pi^+\pi^+$	0.423±0.007	4.50±0.06	3.81±0.06	4.71±0.07	6196/4096
$\pi^-\pi^-$	0.441±0.007	4.50±0.06	3.87±0.06	4.80±0.07	6200/4096

Table 6.2: Three-dimensional (Bertsch-Pratt) fit parameters by Eq. 2.15 for $\pi^+\pi^+$ and $\pi^-\pi^-$ for $k_{\rm T} = 0.2 - 2.0$ GeV/c at the top $0 - 30\%$ centrality. All radii are in fm, and errors are statistical only.

6.1.3 Collision energy dependence of HBT radii

A source size at hadronic freeze-out stage is theoretically expected to become significantly large due to the formation of QGP. To investigate the collision energy dependence of the source size, hopefully searching for the formation of QGP, the HBT radii are compared with those measured by earlier experiments at lower collision energies. Fig. 6.4 shows the HBT radii measured from $\sqrt{s_{\rm NN}}$ =2 GeV to 200 GeV in central Au+Au (AGS and RHIC) and Pb+Pb (SPS) collisions [24, 25, 27, 28, 29]. The measured pair momentum range is $k_{\rm T}$ =0.3−0.5 GeV/c. The results by AGS-E895 between $\sqrt{s_{\rm NN}} \sim 2-4$ GeV show a rapid decrease of $R_{\rm side}$. The decrease is considered to be originated from the increase of a transverse flow with the energy of collisions. As was reported in [54], the transverse flow velocity steeply rises in the AGS energies, where the thermal energy goes into kinetic degrees of freedom, and saturates at $\sim$ 4 GeV. The HBT radii are less sensitive to the collision energy above the saturation point of transverse flow up to the RHIC energy of 200 GeV; $R_{\rm side}$ and $R_{\rm out}$ are constant at about 4 fm, but $R_{\rm long}$ is slightly increased from about 4 fm to 5 fm. This excitation functions of HBT radii suggest that the transverse

HBT radius is less sensitive to collision energy, while the longitudinal HBT radius looks sensitive to the collision energy. If assuming that QGP is formed at RHIC at $\sqrt{s_{\mathrm{NN}}} =$ 200 GeV but not at lower AGS energies at $\sqrt{s_{\mathrm{NN}}} = 2$ GeV, these results are obviously contrary to a naive theoretical expectation. Furthermore, the fact that the HBT radii are less sensitive to collision energy is a striking result comparing to the fact that the charged multiplicity increases from hundreds to thousands between AGS-SPS energy region.

6.2 Centrality dependence

I study the centrality dependence of one-dimensional and three-dimensional correlation function and resulting HBT radii. The centrality of collisions is expressed in terms of the number of participant, evaluated by the Glauber calculation. The HBT radii are measured as a function of the cubic root of the number of participants. The Bertsch-Pratt HBT radii are also measured with new Coulomb corrections based on the core-halo structure.

6.2.1 Determination of the number of participants

Collision events are triggered by hit information on both ZDC and BBC as described in chapter 3. Each event centrality is determined from the correlation between charge sum deposited in BBC and energy sum deposited in ZDC, as shown by Fig.3.5, and the trigger includes about $92 \pm 3\%$ of the total inelastic cross section of 6.8 b [55]. A simulation of the BBC and ZDC responses with a Glauber model [56, 57] is used to evaluate the number of participating nucleons, N_{part}, in these event centrality classes. I divide the centrality for $0-92\%$ into nine different centrality classes, as listed in Table 6.3 where the averaged number of participants, $\langle N_{\mathrm{part}} \rangle$, with systematic error and the number of pairs in each of those subdivided centrality classes are given. $\langle N_{\mathrm{part}} \rangle$ reaches 351.4 ± 2.9 for the top 5% centrality and 17.1 ± 3.3 at the most peripheral collision for $65-92\%$ centrality. The cubic root of the number of participants $\langle N_{\mathrm{part}} \rangle^{1/3}$, which is proportional to one-dimensional geometrical size if three-dimensional volume is assumed to be uniformly comprised of N_{part}, is also give in Table 6.3. The k_{T} range is 0.2$-$2.0 GeV/c with $\langle k_{\mathrm{T}} \rangle \sim 0.45$ GeV/c

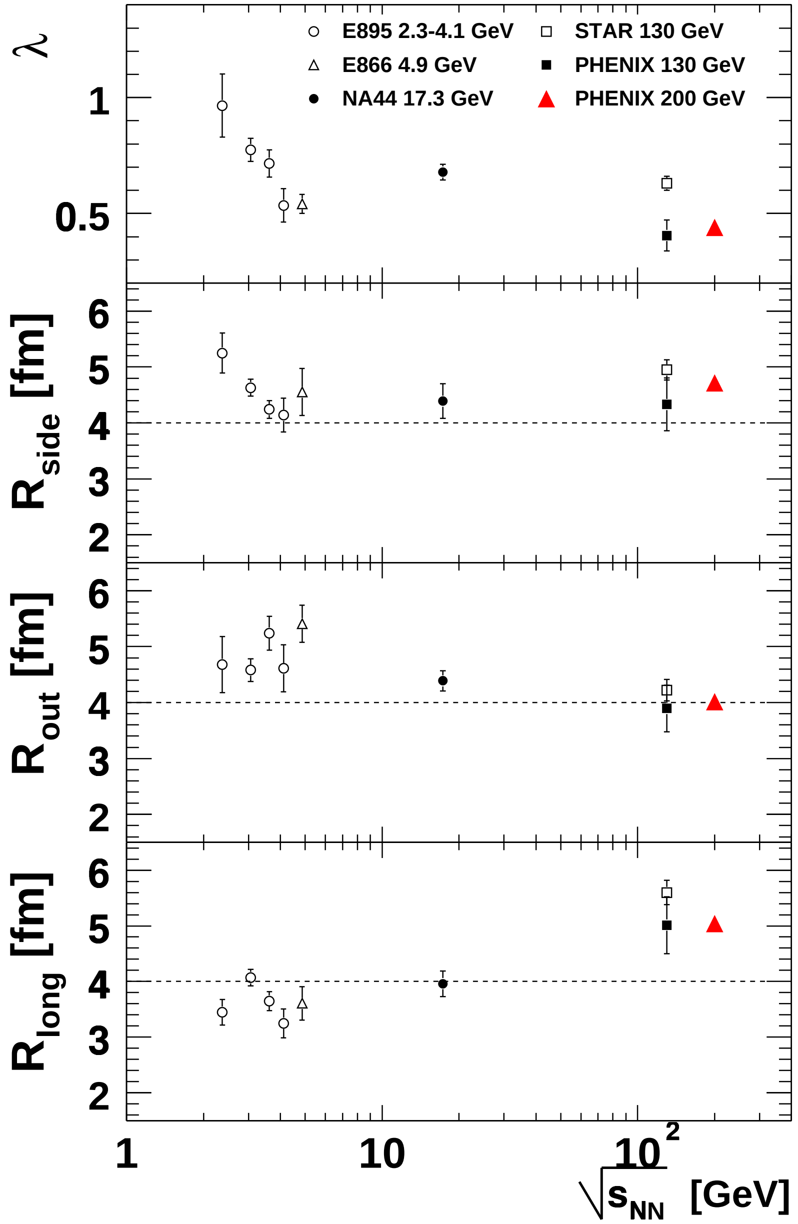

Figure 6.4: Excitation functions of one-dimensional and Bertsch-Pratt HBT radii for central nucleus-nucleus collisions. All HBT radii are measured for $\pi^-\pi^-$ in Au+Au collisions, except for NA44 which is for $\pi^+\pi^+$ in Pb+Pb collision. Error bars are statistical only.

for all of the centrality classes.

class	cent. [%]	$\langle N_{\mathrm{part}} \rangle$	sys.err.	$\langle N_{\mathrm{part}} \rangle^{\frac{1}{3}}$	sys.err.	stat.($\pi^+\pi^+$)	stat.($\pi^-\pi^-$)
inc.	0-92	109.1	4.1	4.78	0.18	108.52 M	137.48 M
semi	0-30	280.6	4.0	6.55	0.09	98.56 M	124.80 M
1	0- 5	351.4	2.9	7.06	0.06	32.64 M	40.80 M
2	5-10	299.0	3.8	6.69	0.09	23.21 M	29.24 M
3	10-15	253.9	4.3	6.33	0.11	16.81 M	21.39 M
4	15-20	215.3	5.3	5.99	0.15	12.10 M	15.51 M
5	20-30	169.3	5.3	5.53	0.17	13.80 M	17.86 M
6	30-40	116.7	4.7	4.89	0.20	6.14 M	8.01 M
7	40-50	76.4	4.0	4.24	0.22	2.44 M	3.20 M
8	50-65	44.5	3.4	3.54	0.27	0.97 M	1.28 M
9	65-92	17.1	3.3	2.58	0.50	0.14 M	0.19 M

Table 6.3: The definition of the inclusive, semi-inclusive and nine subdivided centrality classes. The k_{T} range is 0.2–2.0 GeV/c for all centrality classes. The mean of the number of participant ($\langle N_{\mathrm{part}} \rangle$) in each centrality class is calculated based upon the Glauber model [56]. The number of $\pi^+\pi^+$ ($\pi^-\pi^-$) pairs, analyzed for each of the nine centrality classes, are given in million.

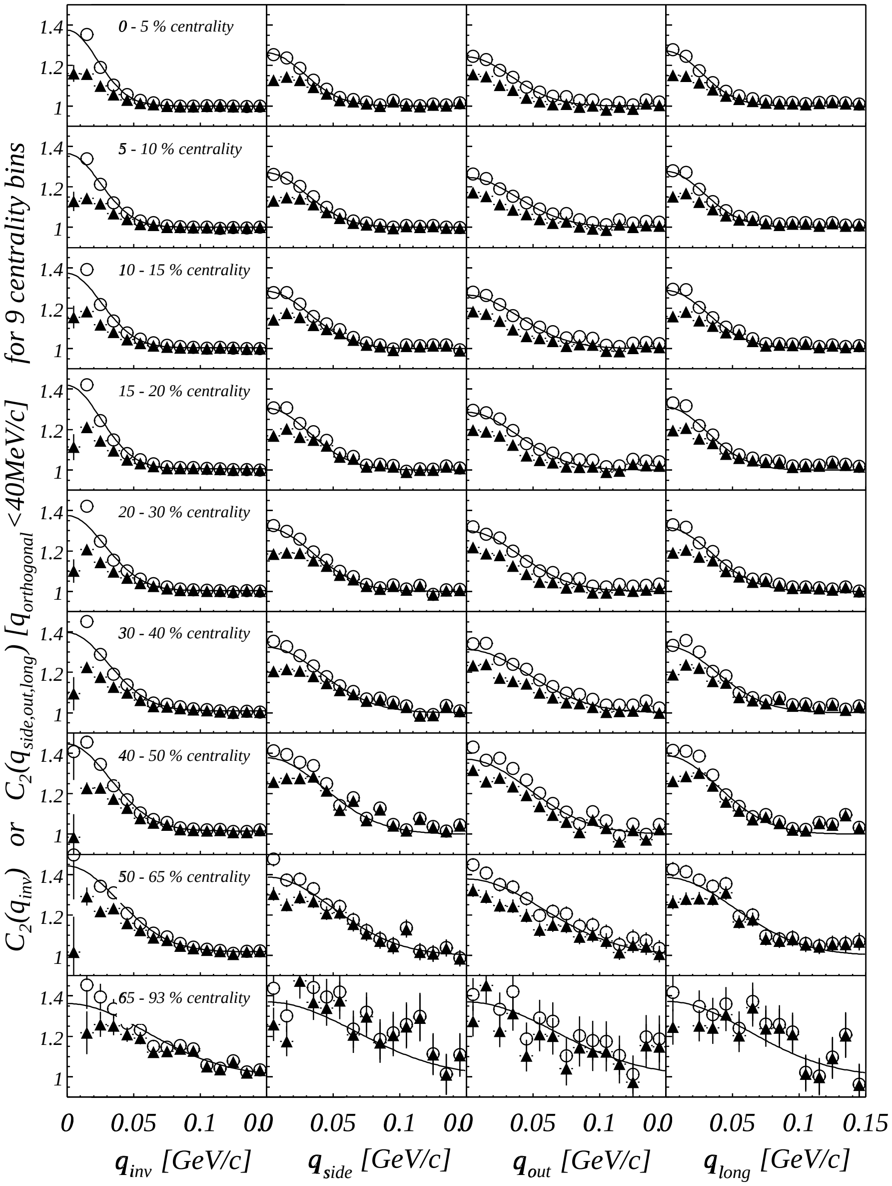

Figure 6.5: One-dimensional and three-dimensional correlation functions of $\pi^-\pi^-$ for nine centrality classes, as defined in Table 6.3, with the *full* Coulomb correction (open circle) and without Coulomb correction (filled triangle). The projections of the three-dimensional correlation functions are averaged over the lowest 40 MeV in the orthogonal directions.

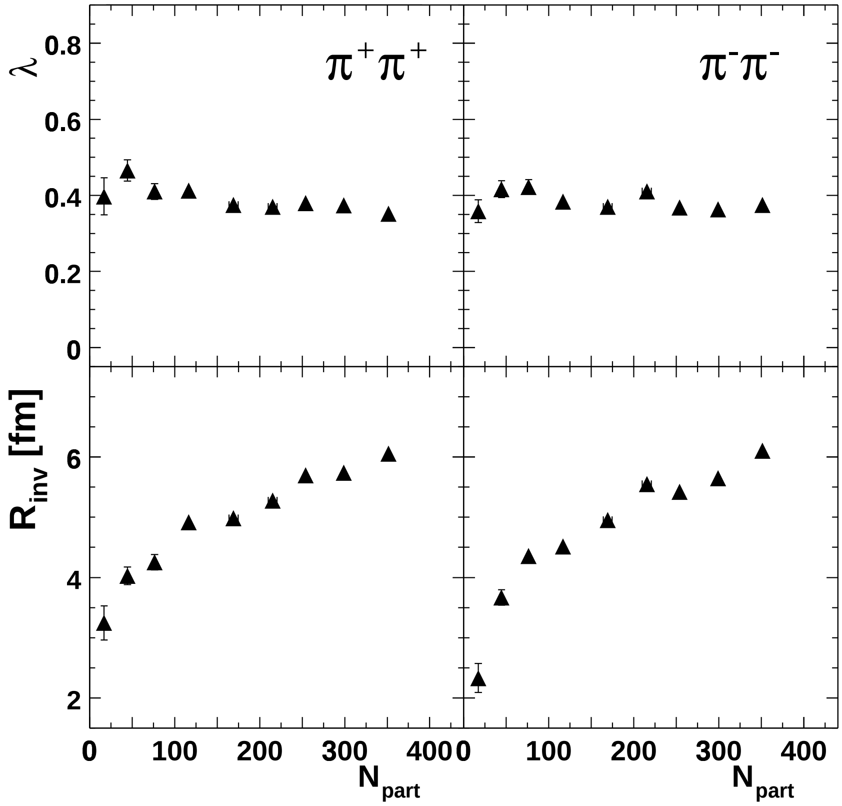

Figure 6.6: One-dimensional radius parameters as a function of the number of participants ($N_{\rm part}$) for $\pi^+\pi^+$ (left) and $\pi^-\pi^-$ (right), for $k_{\rm T}$ = 0.2–2.0 GeV/c ($\langle k_{\rm T}\rangle \sim$ 0.45 GeV/c). The results are obtained with the *full* Coulomb correction and fit of Eq. 2.11. The error is statistical only.

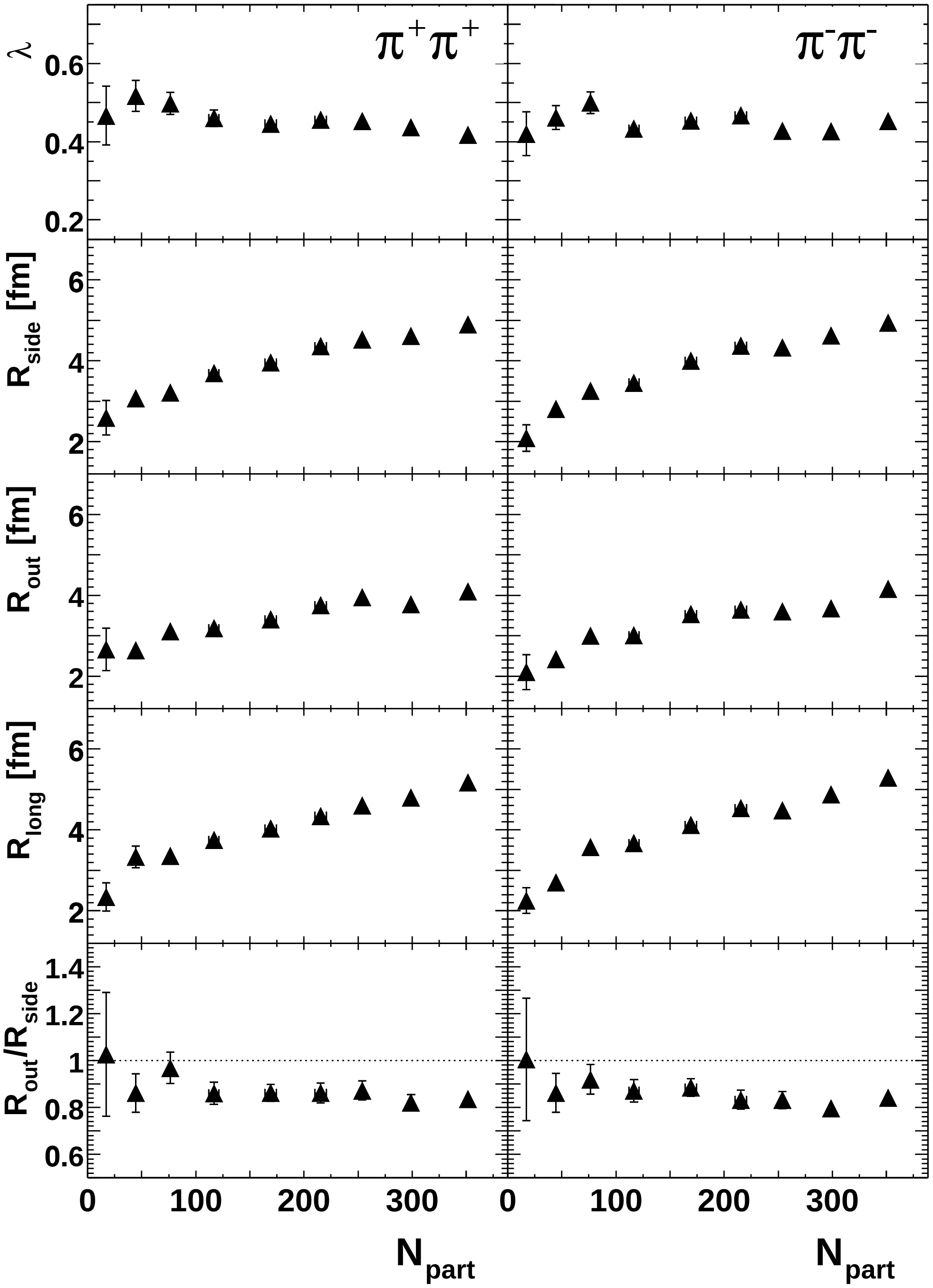

Figure 6.7: Bertsch-Pratt radius parameters as a function of the number of participants (N_{part}) for $\pi^+\pi^+$ (left) and $\pi^-\pi^-$ (right), for $k_{\mathrm{T}} = 0.2$–2.0 GeV/c ($\langle k_{\mathrm{T}} \rangle \sim 0.45$ GeV/c). All radii are obtained with the *full* Coulomb correction and fit of Eq. 2.15, and the error is statistical only.

6.2.2 Centrality dependence of HBT radii

The Bose-Einstein correlation functions for $\pi^+\pi^+$ and $\pi^-\pi^-$ are measured for the nine subdivided centrality classes. Fig. 6.5 shows the one-dimensional and three-dimensional correlation functions of $\pi^-\pi^-$ for the centralities. Each of the nine one-dimensional correlation functions are fitted by Eq. 2.11. Fig. 6.6 shows the fitted one-dimensional HBT radius parameters, $R_{\rm inv}$ and $\lambda_{\rm inv}$, as a function of $N_{\rm part}$ for $\pi^+\pi^+$ (left) and $\pi^-\pi^-$ (right). $R_{\rm inv}$ increases from $\sim 2-3$ fm to ∼6 fm as $N_{\rm part}$ increases from about 17 to 352. On the other hand, $\lambda_{\rm inv}$ is less sensitive to the centrality and constant at ∼0.5 for all centrality classes within the statistical errors.

Fig. 6.7 shows the three-dimensional HBT radii $R_{\rm side}$, $R_{\rm out}$, $R_{\rm long}$ and λ (Fit of Eq. 2.15) with the *full* Coulomb correction, as a function of $N_{\rm part}$ for $\pi^+\pi^+$ (left) and $\pi^-\pi^-$ (right). All of the HBT radii show increase with $N_{\rm part}$, while the chaoticity parameters, λ, are less sensitive to the centrality class.

The bottom of Fig. 6.7 shows the $R_{\rm out}/R_{\rm side}$ ratio as a function of $N_{\rm part}$, which indirectly denotes the centrality dependence of the emission duration of pions. For all measured centrality classes, however, the ratio is less than unity and constant at ∼0.8 within the errors.

6.2.3 Characteristics of $N_{\rm part}$ dependence

The $N_{\rm part}$ denotes the source volume at the initial stage of collisions, while the HBT radius denotes the source volume at the final stage of collisions. The relation between those volumes is one of interesting characteristics of the space-time evolution of source. To investigate the $N_{\rm part}$ dependence of the Bertsch-Pratt radius parameters, I fit with a linear function as:

$$0.5 + p_1 \times {N_{\rm part}}^{p_2}. \tag{6.2}$$

Here, "0.5" means a finite HBT radius observed in earlier analyses in $p-\bar{p}$ collisions [58, 59]. In those studies, the multiplicity dependence of HBT radius has been measured

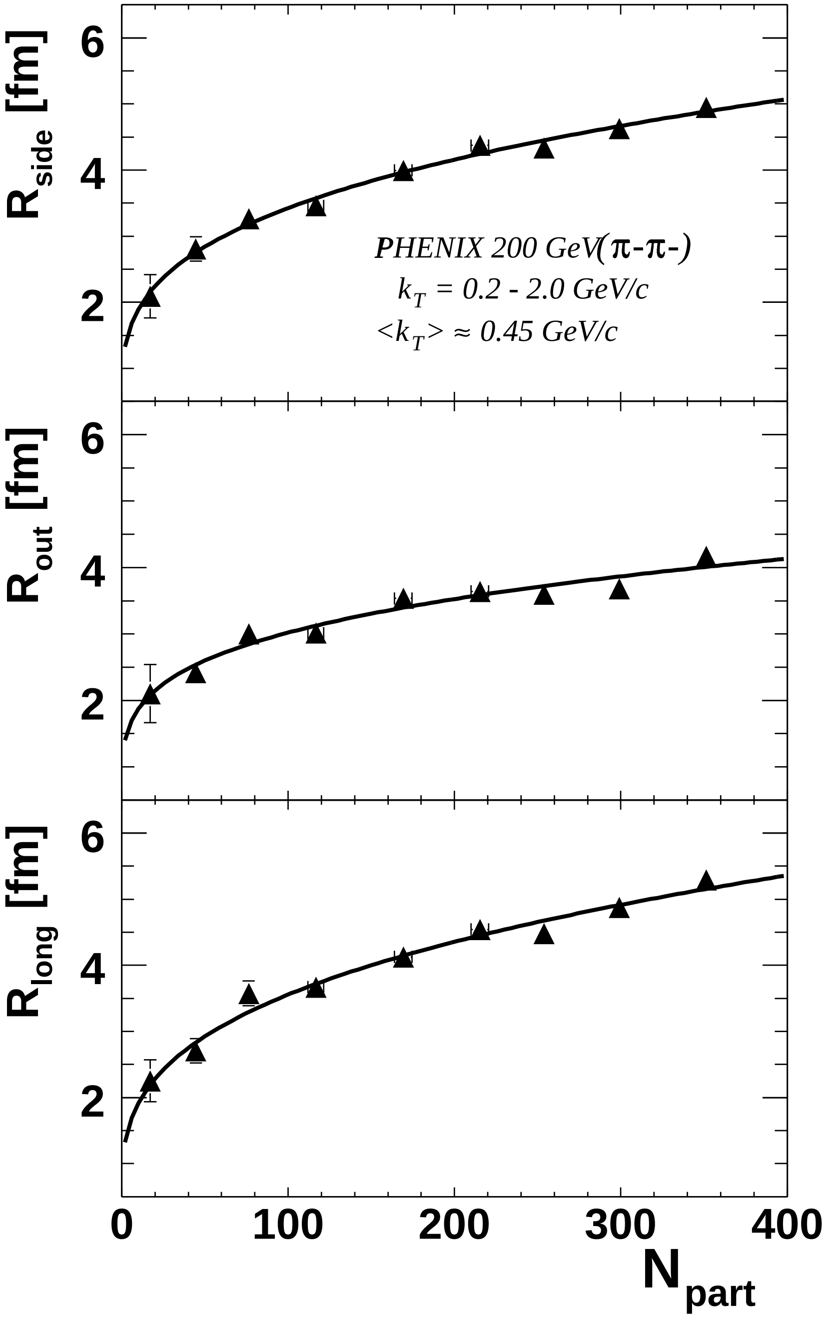

Figure 6.8: Bertsch-Pratt radius parameters versus the cubic root of the number of participants for $\pi^-\pi^-$ with the *full* Coulomb correction (Eq. 2.15), for $k_\mathrm{T} = 0.2\text{--}2.0$ GeV/c with $\langle k_\mathrm{T} \rangle \sim 0.45$ GeV/c. The error is statistical only. The solid curves overlaid on the filled circles show fit lines by $0.5 + p_1 \times {N_\mathrm{part}}^{p_2}$. Fitted p_1 and p_2 values are given in Table 6.4.

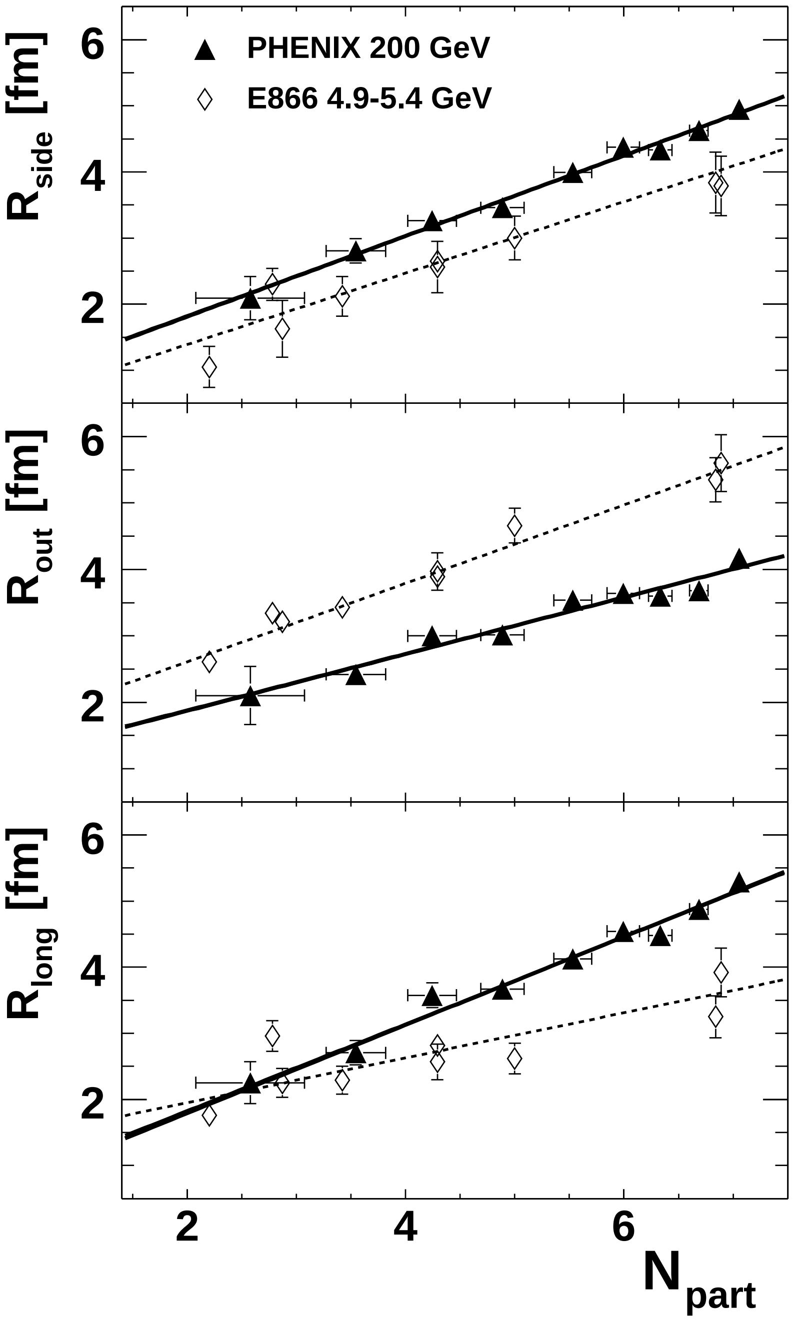

Figure 6.9: Bertsch-Pratt radius parameters as a function of the cubic root of the number of participants for $\pi^-\pi^-$ with the *full* Coulomb correction (Eq. 2.15), for $k_\mathrm{T} = 0.2{-}2.0$ GeV/c with $\langle k_\mathrm{T} \rangle \sim 0.45$ GeV/c. The error is statistical only. The solid lines overlaid on the filled circles show fits to $p_0 + p_1 \times {N_\mathrm{part}}^{1/3}$. Fitted p_0 and p_1 values are given in Table 6.5. Open lozenges show results measured at $\sqrt{s_\mathrm{NN}} = 4.9$ Au+Au and $\sqrt{s_\mathrm{NN}} = 5.4$ GeV Si+Au collisions [24], with the linear fit of $p_0 + p_1 \times {N_\mathrm{part}}^{1/3}$, as shown by dashed lines.

and the extrapolation of the HBT radius to zero multiplicity yields a finite size of 0.5 fm. Fig. 6.8 shows the Bertsch-Pratt radius parameters for $\pi^-\pi^-$ as a function of Np with fitted lines, and resulting fit parameters, p_1 and p_2, are summarized in Table 6.4. The multiplier factor, p_2, is found to be consistent with 1/3 with respect to $R_{\rm side}$ and $R_{\rm long}$ within the errors. Assuming a cylindrical source, this fit result implies the following relation:

$$V_{freeze-out} \approx \text{const.} \times {R_{\rm side}}^2 \times R_{\rm long} \propto N_{\rm part}, \approx V_{initial}, \tag{6.3}$$

where $V_{initial}$ and $V_{freeze-out}$ denote source volumes at initial and hadronic freeze-out stages of collisions. Namely, this results indicates that the overlapping region at final stage is uniformly proportional to its initial stage from peripheral to central collisions. In addition, it looks like that the HBT radii at $N_{\rm part}$ ~2 is around 0.5 which is consistent within errors with those measured $p-\bar{p}$ collisions. If assuming that a phase transition takes place at a certain volume size but not in $p-\bar{p}$ collisions, this intriguing result suggests that the final source volume are not sensitive to the phase transition, which contradicts to a naive picture of the first-order phase transition.

Then, assuming $p_2 = 1/3$, I fit the $N_{\rm part}$ dependence with a linear function as:

$$p_0 + p_1 \times {N_{\rm part}}^{1/3}. \tag{6.4}$$

and compare the result with at a lower collision energy. In Fig. 6.9, filled triangle shows the Bertsch-Pratt radius parameters for $\pi^-\pi^-$ as a function of Np with fitted lines, and resulting fit parameters, p_0 and p_1, are summarized in Table 6.5. $R_{\rm side}$ and $R_{\rm long}$ show similar $N_{\rm part}$ dependencies with one another, while $R_{\rm out}$ has a slightly smaller $N_{\rm part}$ dependence. The open symbols in Fig. 6.9 shows a similar study on the centrality dependence of the Bertsch-Pratt radii measured at $\sqrt{s_{\rm NN}}$ = 4.9 GeV Au+Au and $\sqrt{s_{\rm NN}}$ = 5.4 GeV Si+Au collisions [24]. The fits of $p_0 + p_1 \times {N_{\rm part}}^{1/3}$ are shown by dashed lines. At peripheral collisions, measured $R_{\rm long}$ are similar for the energy region from ~ 5 to 200 GeV, while at central collisions, $R_{\rm long}$ at 200 GeV is significantly larger than that at ~5 GeV. In other words, the $N_{\rm part}$ dependence of $R_{\rm long}$ at $\sqrt{s_{\rm NN}}$ = 200 GeV shows a steep rise rather than the result measured at ∼5 GeV, while, that dependence of transverse HBT radii, R_{side}, is similar to that at the lower energy.

6.2.4 Results with new Coulomb corrections

The conventional *full* Coulomb correction method, which has been used so far in many earlier analyses, seems to be an excessive correction because of pions decays from long-lived particles, as was assessed in chapter 5. To solve the issue, the new (called "*partial*") Coulomb correction, which is expressed by Eq. 5.3, is applied to measure the HBT radii in the assumption of the core-halo structure of source. In case of the correlation functions with the *full* Coulomb correction, as shown by open circles in Fig 6.5, were fitted to Eq. 2.15. On the other hand, in the *partial* Coulomb correction, "raw" correlation functions, namely with detector efficiency corrections but no Coulomb correction, are fitted to the core-halo parameterization including the Coulomb correction term defined by Eq. 5.3.

Fig. 6.10 shows the ${N_{\mathrm{part}}}^{1/3}$ dependences of Bertsch-Pratt HBT radii for $\pi^+\pi^+$ and $\pi^-\pi^-$ with the *partial* Coulomb correction (filled triangle) comparing to those with the *full* Coulomb correction (open circle). Total systematic errors of the HBT radii, including the systematic errors due to the *partial* Coulomb correction, are given by two solid lines that mean the upper and lower bounds of the systematic error. The chaoticity parameter, λ, and R_{out} are significantly changed from those with the *full* Coulomb correction, especially at central collisions.

The investigation of the N_{part} dependences of HBT radii is done by fitting of Eq. 6.2 and Eq. 6.4 to the radii with the *partial* Coulomb correction. The fitted parameters are given in Table 6.4 and 6.5. The fit of Eq. 6.2 provides in a similar result as the *full* Coulomb correction that the centrality dependences of HBT radii are well described by linear functions of ${N_{\mathrm{part}}}^{1/3}$. The dashed lines in Fig. 6.10 show the fits of $p_0 + p_1 \times {N_{\mathrm{part}}}^{1/3}$ to the N_{part} dependence of HBT radii with the *partial* Coulomb correction. With respect to the N_{part} dependences of R_{side} and R_{long}, the fit results are not changed and equal to those of the *full* Coulomb correction within the statistical errors. On the other hand, the

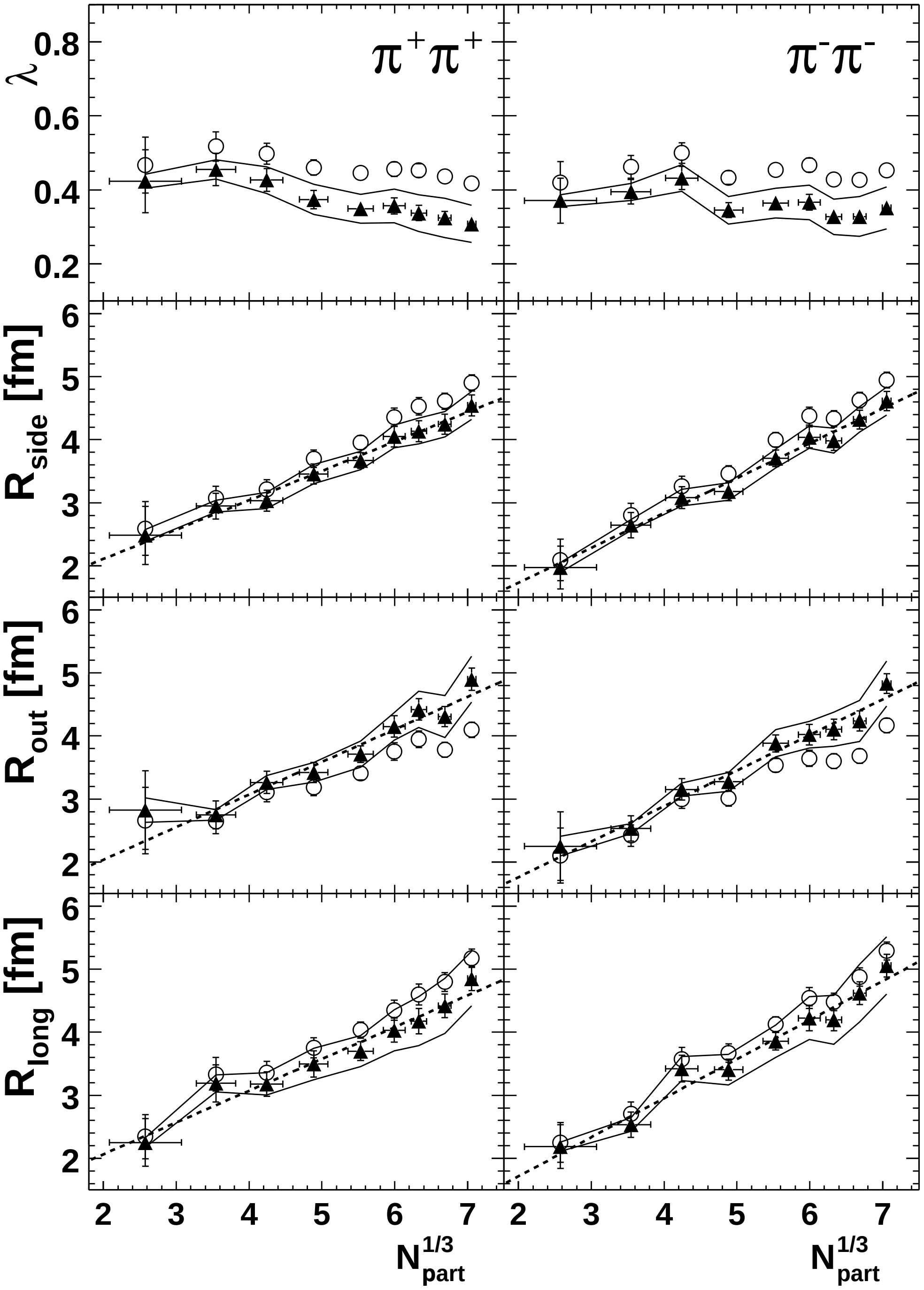

Figure 6.10: Bertsch-Pratt radius parameters as a function of ${N_{\mathrm{part}}}^{1/3}$ for $\pi^+\pi^+$ and $\pi^-\pi^-$, for $k_{\mathrm{T}} = 0.2 - 2.0$ GeV/c with $\langle k_{\mathrm{T}} \rangle \sim 0.45$ GeV/c. Filled triangles show results from fits to a core-halo structure by Eq. 5.3, with statistical error bars and systematic error bands. Dashed lines show fits of $p_0 + p_1 \times {N_{\mathrm{part}}}^{1/3}$. Fitted p_0 and p_1 values are given in Table 6.5. Open circles show the results from the *full* Coulomb correction (Eq. 2.15) with statistical error bars.

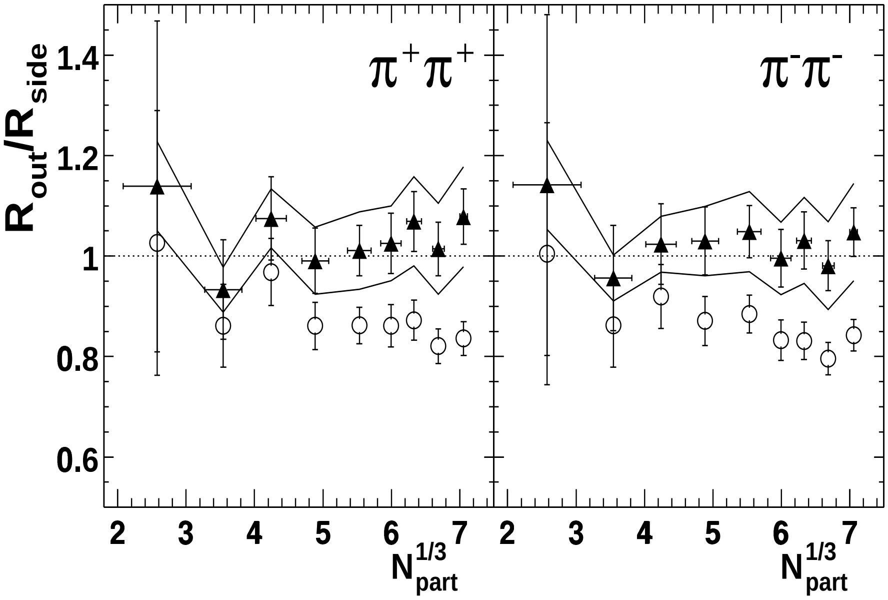

Figure 6.11: Centrality (${N_{\rm part}}^{1/3}$) dependence of $R_{\rm out}/R_{\rm side}$ for $\pi^+\pi^+$ (left) and $\pi^-\pi^-$ (right) pairs for $k_{\rm T} = 0.2 - 2.0$ GeV/c with $\langle k_{\rm T}\rangle \sim 0.45$ GeV/c. Filled triangles show results from fits to a core-halo structure with statistical error bars and systematic error bands. Open circles show the results from the *full* Coulomb correction with statistical error bars.

fit result on $R_{\rm out}$ changes significantly and come to close with the dependences of $R_{\rm side}$ and $R_{\rm long}$. As a result, all Bertsch-Pratt HBT radii from the *partial* Coulomb correction are consistent with a linear increase with ${N_{\rm part}}^{1/3}$, and all radii also show similar ${N_{\rm part}}^{1/3}$ dependencies.

Fig. 6.11 shows $R_{\rm out}/R_{\rm side}$ ratios for $\pi^+\pi^+$ (left) and $\pi^-\pi^-$ (right) pairs as a function of $N_{\rm part}$ measured with the two Coulomb corrections. While $R_{\rm out}/R_{\rm side}$ ratios with the *full* Coulomb correction are ∼0.8 especially at central collisions, $R_{\rm out}/R_{\rm side}$ ratios with the *partial* Coulomb correction are approximately constant at unity over the entire centrality range. The difference seems to be prominent at the most central collisions, where the $R_{\rm out}/R_{\rm side}$ of the *partial* Coulomb is about 20% larger than that of the *full* Coulomb correction and the difference is apparently larger than the total error, ∼ 10%.

	Radius		p_1	p_2	χ^2/DoF
full Coulomb Eq.2.15	$\pi^+\pi^+$	R_{side}	0.82±0.12	0.28±0.03	2.55/7
		R_{out}	0.92±0.15	0.23±0.03	5.38/7
		R_{long}	0.78±0.13	0.30±0.03	3.83/7
	$\pi^-\pi^-$	R_{side}	0.66±0.09	0.32±0.03	3.01/7
		R_{out}	0.75±0.12	0.26±0.03	9.36/7
		R_{long}	0.65±0.10	0.33±0.03	5.85/7
partial Coulomb Eq.5.3	$\pi^+\pi^+$	R_{side}	0.83±0.14	0.27±0.03	2.18/7
		R_{out}	0.70±0.13	0.30±0.03	6.19/7
		R_{long}	0.78±0.16	0.28±0.04	4.44/7
	$\pi^-\pi^-$	R_{side}	0.61±0.11	0.32±0.03	3.07/7
		R_{out}	0.61±0.11	0.33±0.03	5.68/7
		R_{long}	0.58±0.11	0.34±0.03	5.76/7

Table 6.4: Fit parameters by $0.5 + p_1 \times {N_{\text{part}}}^{p_2}$ for the measured Bertsch-Pratt radius parameters with the *full* and *partial* Coulomb correction.

	Radius		p_0	p_1	χ^2/DoF
full Coulomb Eq.2.15	$\pi^+\pi^+$	R_{side}	1.00±0.31	0.55±0.05	1.57/7
		R_{out}	1.39±0.28	0.38±0.05	4.53/7
		R_{long}	0.86±0.35	0.59±0.06	2.75/7
	$\pi^-\pi^-$	R_{side}	0.60±0.31	0.61±0.05	2.19/7
		R_{out}	1.03±0.28	0.43±0.05	7.96/7
		R_{long}	0.46±0.34	0.67±0.06	4.40/7
partial Coulomb Eq.5.3	$\pi^+\pi^+$	R_{side}	1.12±0.33	0.48±0.06	1.43/7
		R_{out}	0.78±0.37	0.56±0.06	5.07/7
		R_{long}	0.96±0.39	0.52±0.07	3.52/7
	$\pi^-\pi^-$	R_{side}	0.58±0.33	0.56±0.06	2.37/7
		R_{out}	0.55±0.35	0.58±0.06	4.75/7
		R_{long}	0.39±0.37	0.64±0.06	4.67/7

Table 6.5: Fit parameters by $p_0 + p_1 \times {N_{\text{part}}}^{1/3}$ for the measured Bertsch-Pratt radius parameters with the *full* and *partial* Coulomb corrections.

6.3 k_{T} dependence

To study the characteristics of dynamical source, the Bose-Einstein correlation functions are measured as a function of the mean transverse momentum of pairs, k_{T}. Model fits of the k_{T} dependence of Bertsch-Pratt HBT radii provide the geometrical size and life time of the source. Comparisons with the earlier experimental results and recent theoretical predictions are also presented.

6.3.1 Definition of k_{T} class

The data sample for the inclusive k_{T} range from 0.2 to 2.0 GeV/c is divided into nine data samples for different k_{T} range as shown by Fig. 6.12. The mean k_{T} values and errors are summarized in Table 6.6 with statistics available. In the estimate of the mean k_{T}, I used only pairs at low relative momentum region $q_{\mathrm{inv}} < 2/R_{\mathrm{inv}}$, where R_{inv} is the measured one-dimensional HBT radius for each k_{T} range, because pairs in the region carry information on the source dimensions [24]. In Table 6.6, $\langle k_{\mathrm{T}} \rangle$ shows the restricted mean k_{T} and $\langle k_{\mathrm{T}} \rangle^*$ shows the simple mean k_{T}, which is estimated by using all pairs in the k_{T} range. The both mean k_{T} are quite same values except for the inclusive k_{T} range. $\langle k_{\mathrm{T}} \rangle$ at the lowest k_{T} class is 0.27±0.02 GeV/c, and reaches 1.15±0.18 GeV/c at the highest k_{T} class.

6.3.2 Results: k_{T} dependence of HBT radii

The Bose-Einstein correlation functions of $\pi^+\pi^+$ and $\pi^-\pi^-$ are measured in each of the nine different k_{T} ranges, in Table 6.6. Fig. 6.13 shows the one-dimensional and the three-dimensional correlation functions of $\pi^-\pi^-$ for the nine k_{T} classes for $0-30\%$ centrality of collisions.

Fig. 6.14 shows one-dimensional HBT radius parameters, R_{inv} and λ_{inv}, and Fig. 6.15 shows the three-dimensional Bertsch-Pratt radius parameters, R_{side}, R_{out}, R_{long} and λ, as a function of k_{T}. Here, the k_{T} values in x-axis correspond to $\langle k_{\mathrm{T}} \rangle$ for the nine k_{T} classes. and results are obtained with the *full* Coulomb correction. All of the measured

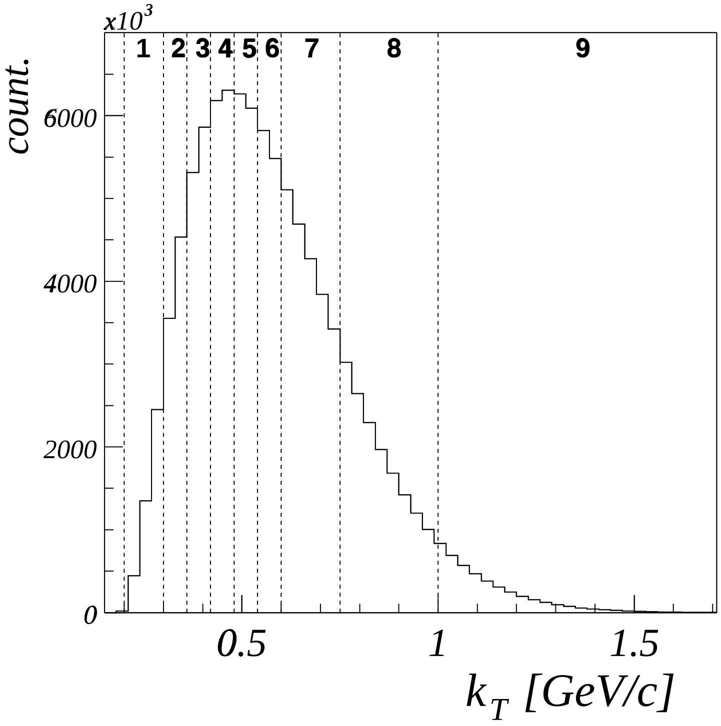

Figure 6.12: The k_{T} distribution of $\pi^+\pi^+$ pairs, divided into nine k_{T} classes as shown by dashed lines. The numbering of each class corresponds to that in Table 6.6.

HBT radii, R_{side}, R_{out} and R_{long}, decrease by a factor of $\sim 2-3$ as k_{T} increases from $\sim$0.2 to $\sim$1.2 GeV/c. Bottom panels in Fig. 6.15 show the k_{T} dependence of $R_{\mathrm{out}}/R_{\mathrm{side}}$ ratios. The $R_{\mathrm{out}}/R_{\mathrm{side}}$ ratio is apparently less than unity, and systematically decreases as k_{T} increases.

6.3.3 Results with *partial* Coulomb correction

In the study of centrality dependence of HBT radii in the previous section, discrepancies of HBT radii between the *full* and *partial* Coulomb corrections can be clearly seen at central collisions. Here, I study the k_{T} dependence of HBT radii with *partial* Coulomb correction by Eq. 5.3, at the central collisions. The Bertsch-Pratt radius parameters and the $R_{\mathrm{out}}/R_{\mathrm{side}}$ ratio for $\pi^+\pi^+$ and $\pi^-\pi^-$ with *partial* Coulomb correction are shown in Fig. 6.16 and 6.17, respectively, comparing to those of the *full* Coulomb correction. The total systematic errors on the HBT radius parameters for the nine k_{T} classes are shown

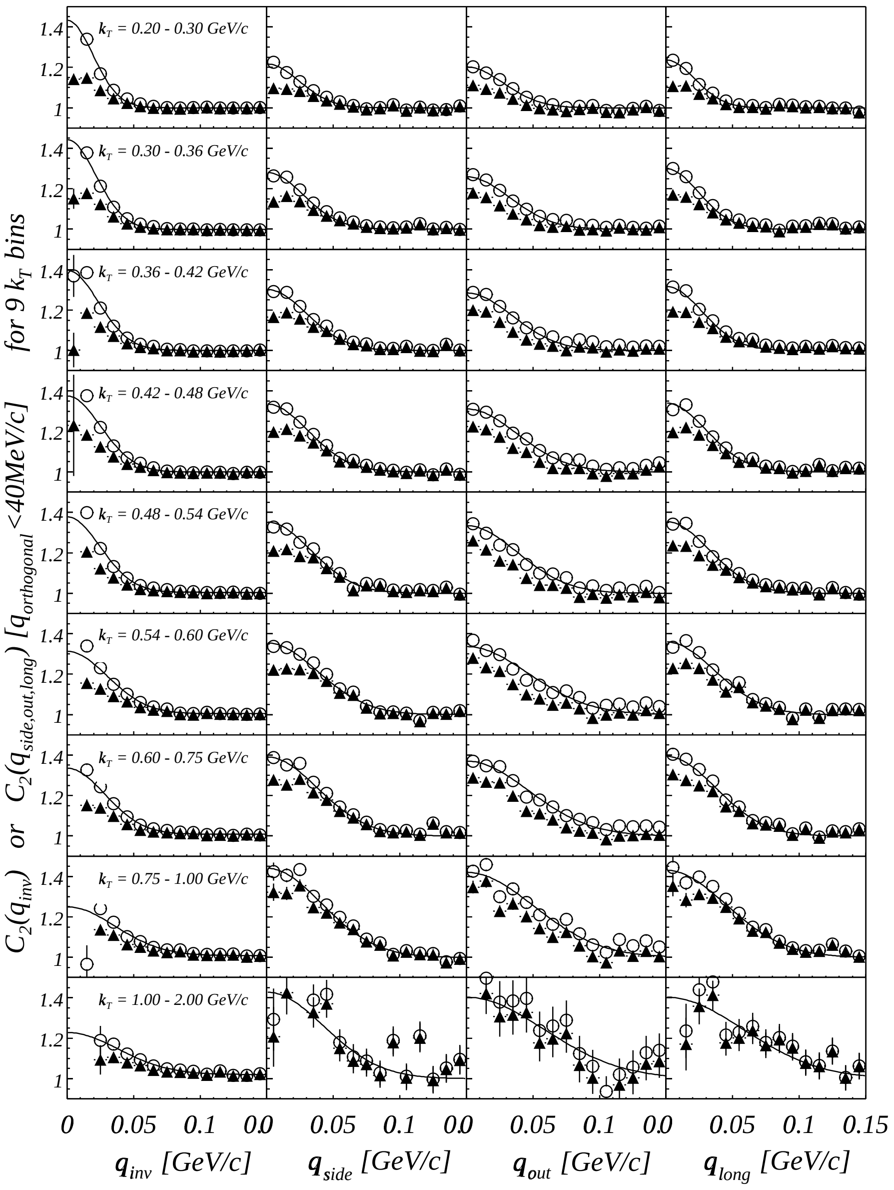

Figure 6.13: One-dimensional and three-dimensional correlation functions of $\pi^-\pi^-$ for nine k_{T} classes as defined by Table 6.6, with the *full* Coulomb correction (open circle) and without Coulomb correction (filled triangle), for 30% centrality of collisions. The projections of the three-dimensional correlation functions are averaged over the lowest 40 MeV in the orthogonal directions.

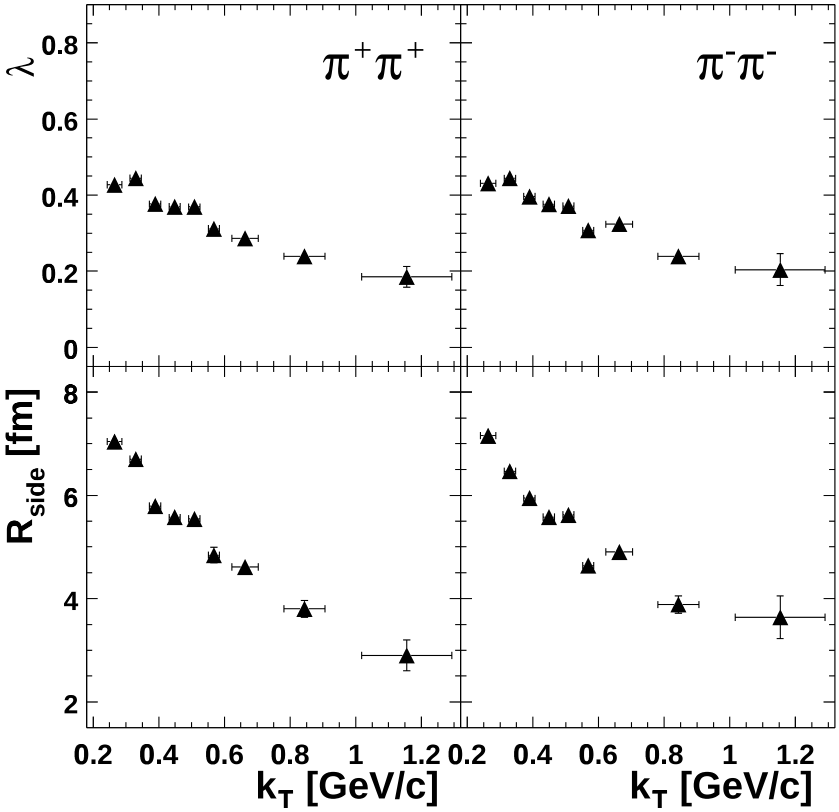

Figure 6.14: The k_{T} dependence of λ_{inv} and R_{inv} for $\pi^+\pi^+$ (left) and $\pi^-\pi^-$ (right) pairs with *full* Coulomb correction (Eq. 2.11) for 0-30% centrality. The error is statistical only.

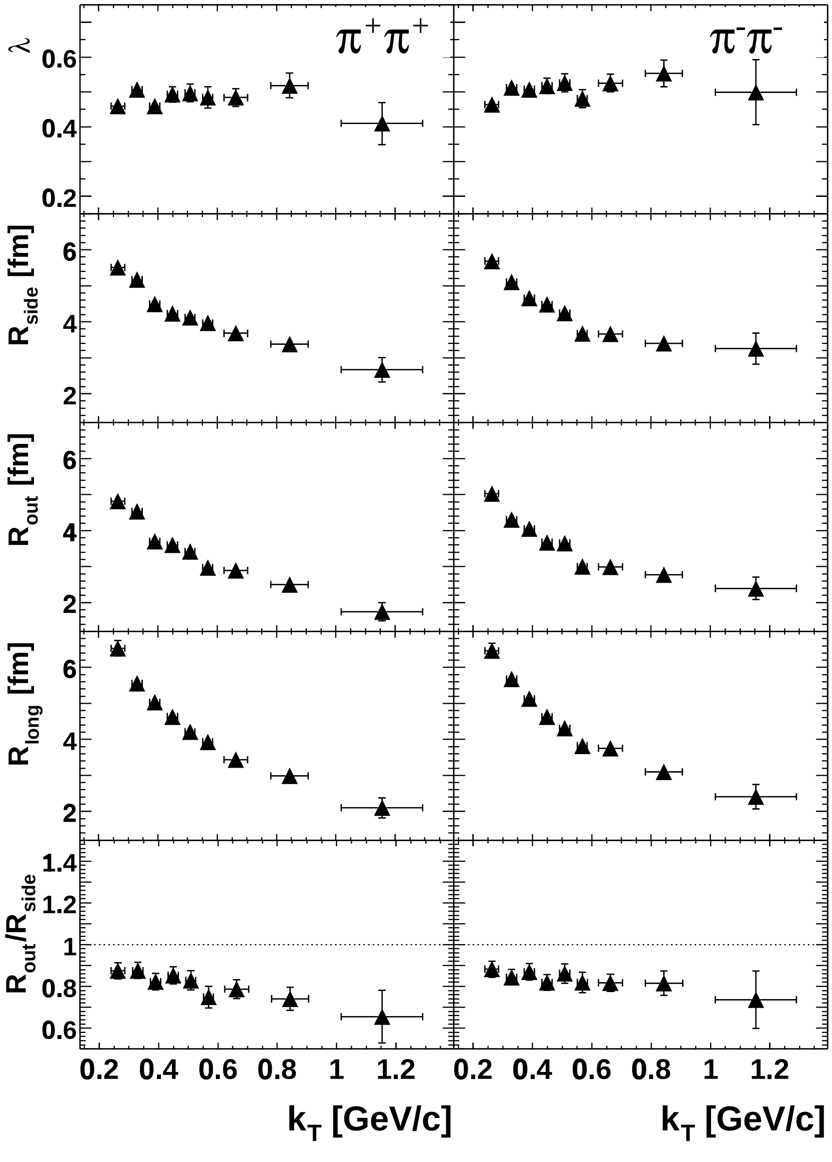

Figure 6.15: The k_T dependence of λ, R_{side}, R_{out} and R_{long} for $\pi^+\pi^+$ (left) and $\pi^-\pi^-$ (right) pairs with *full* Coulomb correction (Eq. 2.15) for 0-30% centrality. The error is statistical only.

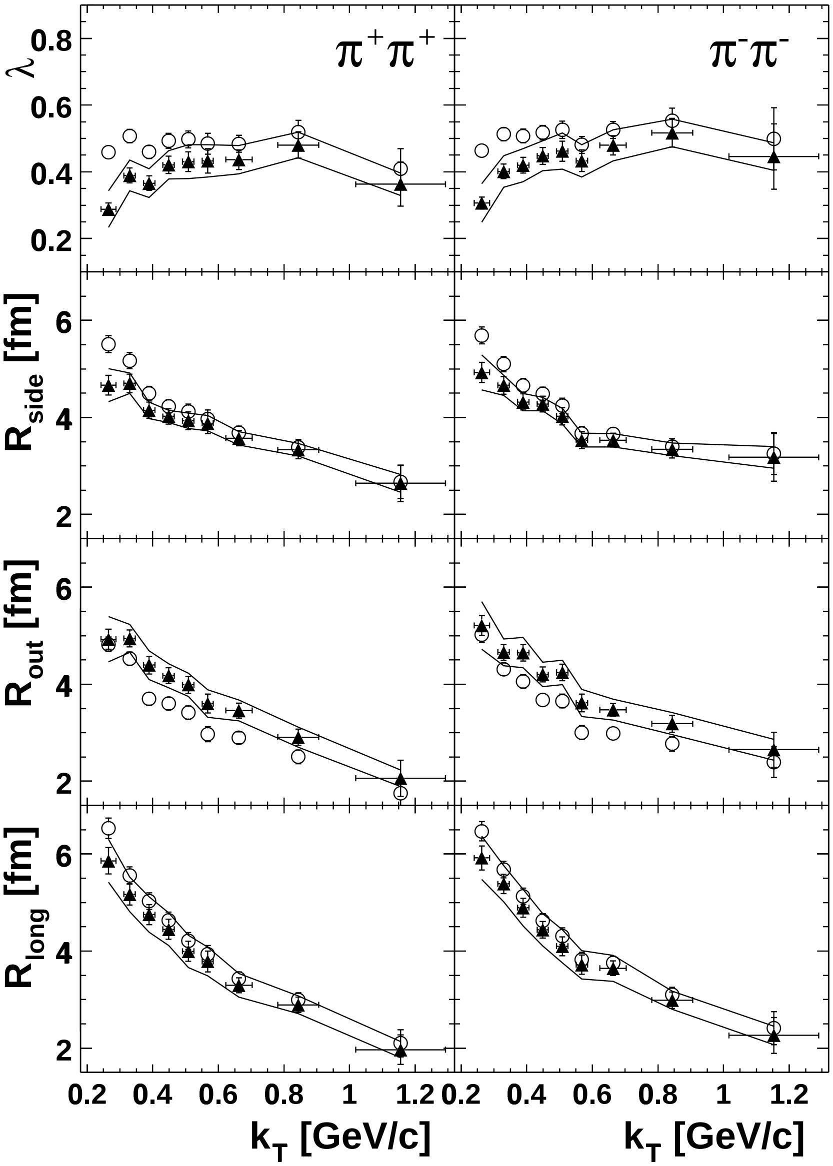

Figure 6.16: The k_{T} dependence of the λ, R_{side}, R_{out} and R_{long} for $\pi^+\pi^+$ (left) and $\pi^-\pi^-$ (right) pairs for 0-30% centrality. Filled triangles show results with *partial* Coulomb correction by fits to a core-halo structure (Eq. 5.3), with statistical error bars and systematic error bands. Open circles show results with the *full* Coulomb correction (Eq. 2.15) with statistical errors.

class	$k_{\rm T}$ range	$\langle k_{\rm T}\rangle$	r.m.s	$\langle k_{\rm T}\rangle^*$	r.m.s	stat.($\pi^+\pi^+$)	stat.($\pi^-\pi^-$)
inc.	0.20−2.00	0.446	0.167	0.582	0.206	98.56 M	124.80 M
1	0.20−0.30	0.265	0.023	0.270	0.022	4.04 M	6.63 M
2	0.30−0.36	0.330	0.017	0.330	0.017	6.72 M	8.52 M
3	0.36−0.42	0.389	0.017	0.389	0.017	7.22 M	8.63 M
4	0.42−0.48	0.448	0.017	0.448	0.017	6.53 M	7.65 M
5	0.48−0.54	0.508	0.017	0.508	0.017	5.37 M	6.25 M
6	0.54−0.60	0.568	0.017	0.568	0.017	4.16 M	4.80 M
7	0.60−0.75	0.663	0.040	0.663	0.039	7.67 M	9.04 M
8	0.75−1.00	0.844	0.063	0.845	0.061	5.26 M	6.07 M
9	1.00−2.00	1.156	0.137	1.180	0.156	1.76 M	1.97 M

Table 6.6: The definition of the inclusive and nine subdivided $k_{\rm T}$ classes. The restricted mean $\langle k_{\rm T}\rangle$ and simple mean $\langle k_{\rm T}\rangle^*$ (see text) are given for each of the $k_{\rm T}$ ranges, with root mean square values of the $k_{\rm T}$ distributions. All $k_{\rm T}$ values are in GeV/c. The pair statistics in each class is also given.

in the right panel of Fig. 5.5, and given as systematic error bands in those figures.

The chaoticity parameters, λ, with the partial Coulomb correction are significantly decreased from that of with the *full* Coulomb correction in the low $k_{\rm T}$ regions. Also $R_{\rm side}$ and $R_{\rm long}$ show a similar trend for the Coulomb corrections that results from *partial* Coulomb correction clearly decrease from those of the *full* Coulomb correction at low $k_{\rm T}$ region. On the other hand, $R_{\rm out}$ significantly increase for entire measured $k_{\rm T}$ range. Due to the opposite effect on $R_{\rm side}$ and $R_{\rm out}$, the $R_{\rm out}/R_{\rm side}$ ratio is found to be very sensitive to the strength of Coulomb correction. We found that the $R_{\rm out}/R_{\rm side}$ ratio is 0.8-1.1 with the partial Coulomb correction for the measured $k_{\rm T}$ range, which is about 20% larger than that with the *full* Coulomb correction, which is 0.7-0.9. In any case, the $R_{\rm out}/R_{\rm side}$ ratio shows a similar trend that gently decreases as $k_{\rm T}$ increases.

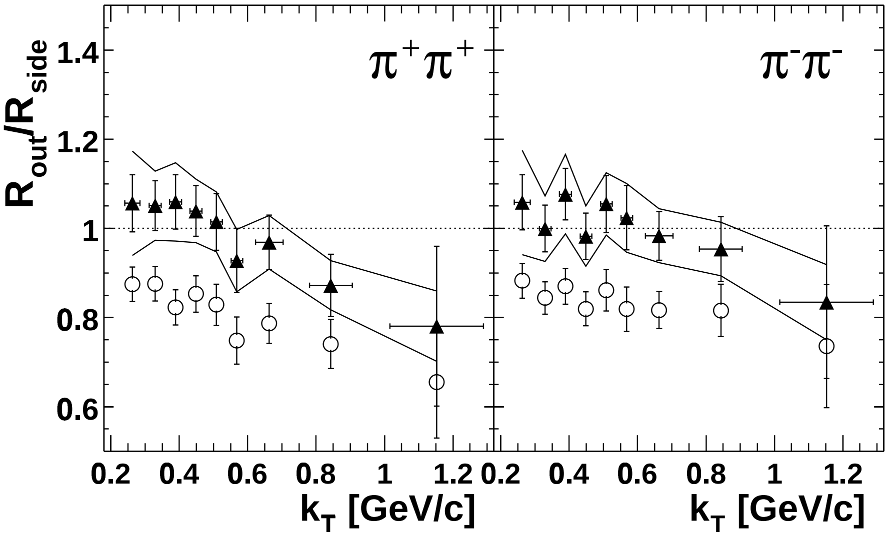

Figure 6.17: The $k_{\rm T}$ dependence of $R_{\rm out}/R_{\rm side}$ for $\pi^+\pi^+$ (left) and $\pi^-\pi^-$ (right) pairs for 0-30% centrality. Filled triangles show results with *partial* Coulomb correction by fits to a core-halo structure (Eq. 5.3), with statistical error bars and systematic error bands. Open circles show results with the *full* Coulomb correction (Eq. 2.15) with statistical errors.

6.3.4 Model fit on $k_{\rm T}$ dependence

As described in Chapter 2, HBT radius is considered to decrease as $k_{\rm T}$ increases due to "length of homogeneity" in the expanding source. Fig. 6.18 shows the $k_{\rm T}$ dependence of the HBT radii evaluated by numerical calculations [60]. As shown in the top two panels, $R_{\rm side}$ is constant with $k_{\rm T}$ in the case without transverse flow, and the slope becomes steeper as transverse flow increases, and $R_{\rm out}$ is slightly larger than $R_{\rm side}$ because of the additional term of the emission duration of particles. In theoretical approximation, the Bose-Einstein correlation function can be expressed as:

$$C_2(\mathbf{q},\mathbf{k}) = 1 + \left| \frac{\int d^4x S(x,k) e^{-ix\cdot q}}{\int d^4x S(x,k)} \right|^2 \tag{6.5}$$

where $\mathbf{k} = (\mathbf{p}_1 + \mathbf{p}_2)/2$ is the mean of the momentum of pair. The emission function $S(x, K)$ is an effective single-particle Wigner phase-space density of the particles in the emitting source. Assuming a azimuthally symmetric Gaussian source, longitudinal boost-invariant and no resonance contribution, the emission function is analytically expressed

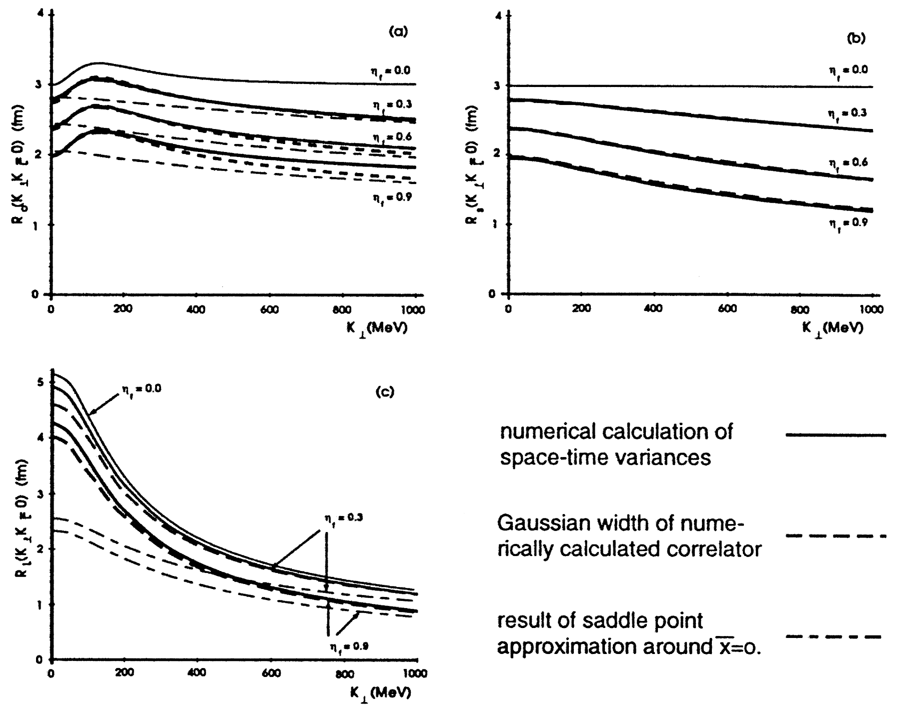

Figure 6.18: k_{T} dependence of the HBT radii R_{out} (a), R_{side} (b) and R_{long} (c) for different collective flow velocities (η_f) [60], where a linear transverse flow rapidity profile $\eta_t(r) = \eta_f(r/R_{\mathrm{geom}})$ is assumed. The solid and dashed lines are numerically calculated from space-time variances and Gaussian widths, respectively. The dash-dotted lines show results of saddle point approximation around x_μ, while the true saddle point $\bar{x}_\mu$ for finite η_f is shifted in the outward direction.

as:

$$S(x,k) = \frac{\tau_0 m_{\mathrm{T}} \cosh(\eta - Y)}{(2\pi)^3\sqrt{2\pi(\Delta\tau)^2}} \exp\left[-\frac{k\cdot u(x)}{T_f} - \frac{r^2}{2{R_{\mathrm{geom}}}^2} - \frac{\eta^2}{2(\Delta\eta)^2} - \frac{(\tau-\tau_0)^2}{2(\Delta\tau)^2}\right] \tag{6.6}$$

where T_f is a constant freeze-out temperature and τ_0 is the proper time of the freeze-out, $m_{\mathrm{T}}(=\sqrt{{k_{\mathrm{T}}}^2 + m^2})$ is the transverse mass momentum of pair, $r = \sqrt{x^2+y^2}$, $\eta = \frac{1}{2}\ln[(t+z)/(t-z)]$ is the space time rapidity and $\tau = \sqrt{t^2 - z^2}$ is the longitudinal proper time. R_{geom} and $\Delta\eta$ denote the transverse and longitudinal Gaussian widths of the source, and $\Delta\tau$ is a Gaussian width of a finite emission duration of particles. The flow field $u(x)$ can be decomposed in the form

$$u^{(}x) = (\cosh\eta\cosh\beta_t, \frac{x}{r}\sinh\beta_t, \frac{y}{r}\sinh\beta_t, \sinh\eta\cosh\beta_t). \tag{6.7}$$

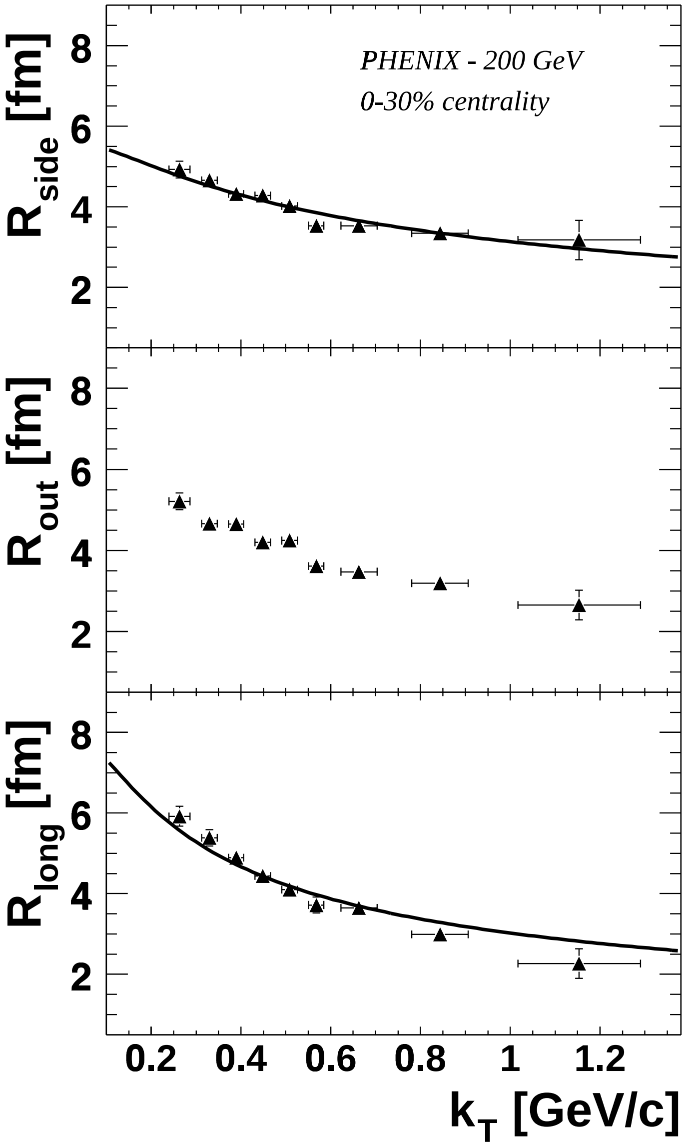

Figure 6.19: k_{T} dependence of 3-dimensional HBT radii for $\pi^-\pi^-$ at the top 30% centrality of collisions. The radii are obtained with the *partial* Coulomb correction. The solid lines in the top and bottom panels are fits of Eq. 6.8 and Eq. 6.10, respectively. The fitted parameters, R_{geom} and τ_0, are given in Table 6.7.

With the emission function and assuming transverse and longitudinal motion can be decoupled, the k_{T} dependence of transverse HBT radius, R_{side}, can be parameterized [60] as:

$$R_{\mathrm{side}}{}^{2}(m_{\mathrm{T}}) \;=\; R_{\mathrm{geom}}{}^{2} \Big/ \left(1+\beta_f^2 \frac{m_{\mathrm{T}}}{T_f}\right) \tag{6.8}$$

where its transverse flow is linearly expressed as $\beta_{\mathrm{T}}(r) = \beta_f(r/R_{\mathrm{geom}})$.

Thus, the fit of Eq. 6.8 to the k_{T} dependence of R_{side} yields the geometrical Gaussian width of transverse source radius, R_{geom}, at the kinetic freeze-out stage. Fig. 6.19 top shows the fit of Eq. 6.8 to the k_{T} dependence of R_{side} measured using $\pi^-\pi^-$ data with the *partial* Coulomb correction. The fit gives $R_{\mathrm{geom}} \sim 7.1 \pm 0.1$ with $\chi 2$/DoF $\sim$5.6/8. Here, we assumed T_f = 120 MeV and $\beta_T = 0.70$, which have been determined using charged pion spectra at central collisions measured by PHENIX at $\sqrt{s_{\mathrm{NN}}}$ = 200 GeV [5, 63]. The fit for $\pi^+\pi^+$ result yields the consistent value within the error, as summarized in Table 6.7. The size is significantly larger than the comparable geometrical size, namely the Gaussian width of Au nuclei, $R_{\mathrm{geom}}(Au) = 3.07$ fm.

The bottom figure of Fig. 6.18 shows a theoretical calculation of the k_{T} dependence of R_{long}, which shows much stronger k_{T} dependence than those of transverse HBT radii because the source expands predominantly in the beam direction and pairs at high-k_{T} tend to be less affected by the longitudinal expansion. In the longitudinal boost-invariant system, R_{long} is independent of longitudinal flow β_L. The k_{T} dependence of R_{long} is approximately expressed as:

$$R_{\mathrm{long}}{}^{2}(m_{\mathrm{T}}) \;\approx\; \tau_0^2 \frac{T}{m_{\mathrm{T}}} \left(1+\left(\frac{1}{2}+\frac{1}{1+\beta_f^2\frac{m_{\mathrm{T}}}{T}}\right)\frac{T}{m_{\mathrm{T}}}\right). \tag{6.9}$$

where τ_0 is the proper time that means the life time of source from collision to the kinetic freeze-out [61]. In relativistic heavy-ion collisions, where $\frac{T}{m_{\mathrm{T}}} << 1$, Eq. 6.9 can be reduced to the leading order approximation without transverse flow [62] as,

$$R_{\mathrm{long}}{}^{2}(m_{\mathrm{T}}) \;\approx\; \tau_0^2 \frac{T_f}{m_{\mathrm{T}}}. \tag{6.10}$$

Eq. 6.10 has been widely used to fit earlier experimental results, and well described those R_{long} dependencies.

	Fit to Eq.6.8		Fit to Eq.6.10	
	$R_{\rm geom}$ (fm)	χ^2/DoF	τ_0 (fm/c)	χ^2/DoF
full Coulomb				
$\pi^+\pi^+$	7.5±0.1	16.6/8	9.0±0.1	26.6/8
$\pi^-\pi^-$	7.6±0.1	23.9/8	9.2±0.1	18.6/8
partial Coulomb				
$\pi^+\pi^+$	7.0±0.1	2.9/8	8.5±0.2	13.8/8
$\pi^-\pi^-$	7.1±0.1	5.6/8	8.8±0.2	9.4/8

Table 6.7: Model fits parameters, $R_{\rm geom}$ by Eq. 6.8 and τ_0 by Eq. 6.10 for results with the *full* and *partial* Coulomb corrections, where $T_f = 120$ MeV and $\beta_f = 0.7$ [63].

Fig. 6.19 bottom shows the fit of Eq. 6.10 to the $k_{\rm T}$ dependence of $R_{\rm long}$. Assuming T_f is 120 MeV, the proper time τ_0 is evaluated to be $\sim 8.8 \pm 0.2$ fm/c with $chi2$/DoF~9.4/8 for *pimp* data, as summarized in Table 6.7.

6.3.5 Comparison with HBT radii at lower energies

Fig. 6.20 shows the $k_{\rm T}$ dependence of Bertsch-Pratt radius parameters measured at mid-rapidities for various collision energies – $\sqrt{s_{\rm NN}} = 4.1$ GeV (E895) [25] and $\sqrt{s_{\rm NN}} = 4.9$ GeV (E866) [24] in Au+Au at AGS, $\sqrt{s_{\rm NN}}$ = 17.3 GeV in Pb+Pb (NA44) [27] at SPS, $\sqrt{s_{\rm NN}}$ = 130 GeV (PHENIX [29] and STAR [28]) and $\sqrt{s_{\rm NN}}$ = 200 GeV (PHENIX) in Au+Au at RHIC. In this figure, all results are obtained with the *full* Coulomb correction. The comparison indicates that the transverse HBT radii, $R_{\rm side}$ and $R_{\rm out}$, are less sensitive to the collision energy, while only the longitudinal HBT radius, $R_{\rm long}$, significantly depends on its collision energy.

$R_{\rm geom}$ for each collision energy is derived by the fit of Eq. 6.8. Fig 6.21 shows evaluated $R_{\rm geom}$ as a function of collision energy for $\sqrt{s_{\rm NN}} \sim 5-200$ GeV with statistical error bar, and the comparable geometrical size of a Au nucleus ($R_{\rm geom}$ = 3.07 fm) is overlaid by the dashed line. In the fits, β_f is set to 0.4 for AGS and SPS energies and to 0.7 for RHIC energies, while T_f is fixed to 120 GeV for all energies [54]. The filled (opened) symbols denote results with the *partial* (*full*) Coulomb correction. A result from CERES

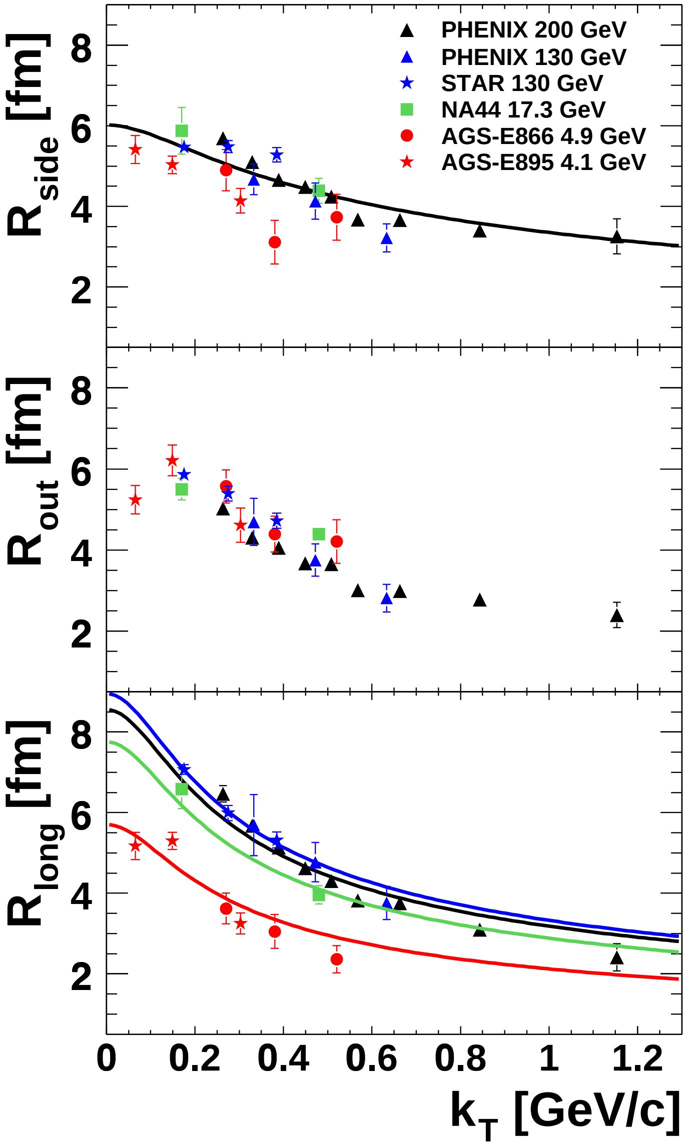

Figure 6.20: k_T dependence of 3-dimensional HBT radii measured at various collision energies; $\sqrt{s_{NN}} \sim 5$ GeV at AGS (E895 and E866), 17.3 GeV at SPS (NA44), 130 GeV and 200 GeV at RHIC (PHENIX and STAR). All HBT radii are measured with *full* Coulomb correction for $\pi^-\pi^-$, except for NA44 ($\pi^+\pi^+$). In the top panel, the solid line is a fit of Eq. 6.8 to the PHENIX-200 GeV. In the bottom panel, solid lines show fits of Eq. 6.10 to data at $\sqrt{s_{NN}} \sim 5$ GeV (red), 17.3 GeV (green), 130 GeV (blue) and 200 GeV (black).

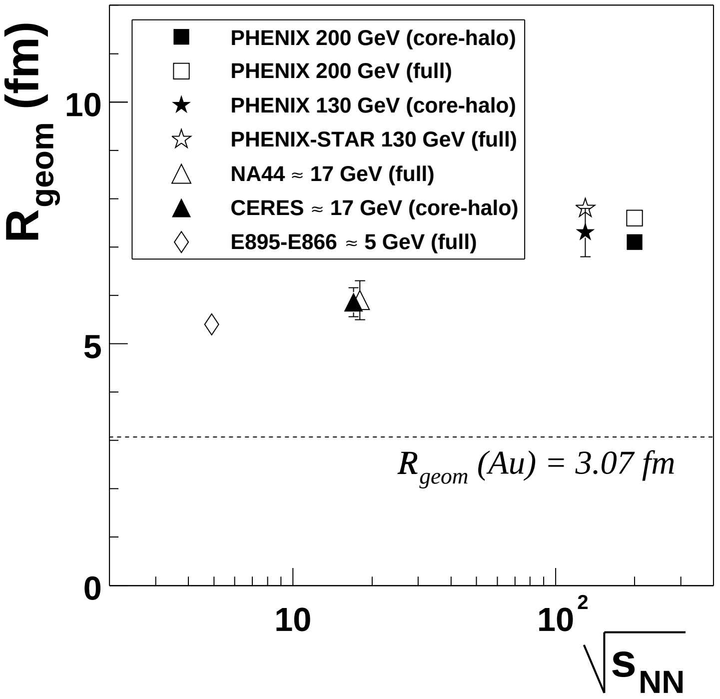

Figure 6.21: The excitation function of the geometrical source size, R_{geom}, evaluated from the fit of Eq. 6.8. Results with *partial* and *full* Coulomb corrections are shown by filled and opened symbols, respectively.

obtained with the *partial* Coulomb correction [35] is also overlaid. The difference between the *partial* and *full* Coulomb corrections looks not significant for R_{geom}. It is found that Rg increases from 5−6 fm at AGS-SPS energies to 7−8 fm at RHIC energies. All the measured R_{geom} are significantly larger than the comparable Au nucleus radius in RMS-width, 3.07 fm. Evaluated R_{geom} sizes at freeze-out at RHIC energies increase about 2 fm from those of AGS-SPS energies, nonetheless the transverse HBT radius parameter, R_{side}, does not show any increase. The reason apparently due to the stronger transverse flows at RHIC energies than those at AGS-SPS energy region. In other words, we in RHIC energy region measure rather "small length of homogeneity" in the Bose-Einstein correlations than those of AGS-SPS energy region.

On the other hand, the k_{T} dependence of R_{long}, which is independent of transverse flow, shows a clear increase with the collision energy, as shown in the bottom panel of

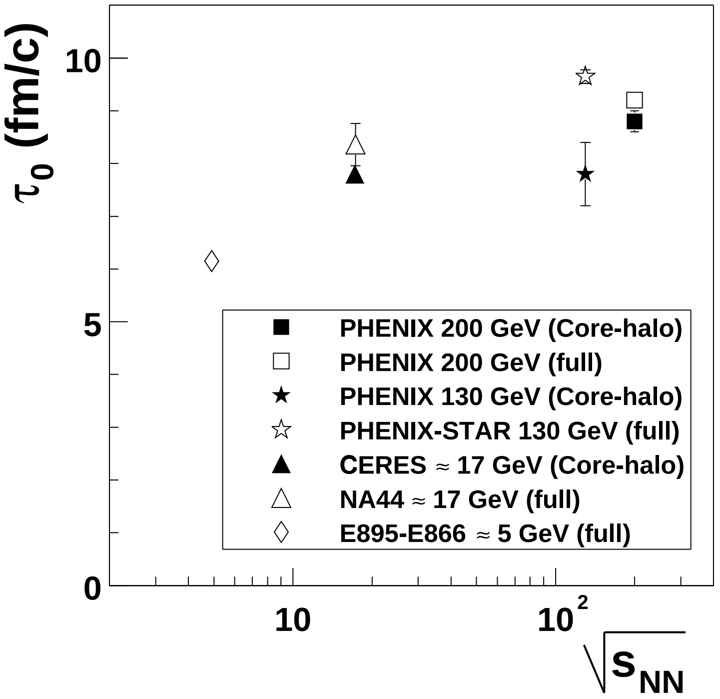

Figure 6.22: The excitation function of the proper time, τ_0, evaluated from the fit of Eq. 6.10. Results with *partial* and *full* Coulomb corrections are shown by filled and opened symbols, respectively.

Fig. 6.20. The fit of Eq. 6.10 provides the collision energy dependence of the proper time, τ_0, i.e. the life time of the system, as shown by Fig. 6.22. Assuming a kinetic freeze-out temperature T_f = 120 MeV for $\sqrt{s_{\rm NN}} \sim 5 - 200$ GeV [54], tau_0 rapidly enlarges from around 6 fm/c to 8 fm/c between AGS and SPS energies, then show a gradual increase from SPS to RHIC energy up to about 9 fm/c. The comparison of results at RHIC 130 GeV and 200 GeV indicates that τ_0 is already saturated at the energy region.

6.4 Comparison to hydrodynamical models

The $k_{\rm T}$ dependence of the Bertsch-Pratt radius parameters is compared to recent theoretical predictions by Soff [30] and Hirano [64] in Fig 6.23. In the Soff's calculation (uRQMD), the QGP is modeled as an ideal fluid, expanding with a bag model equation of state, hadronizing via a first-order phase transition at the critical temperature $T_c = 160$

MeV. The Hirano's calculation is a fully three-dimensional hydrodynamic model, assuming chemically non-equilibrium equation of state, called partial chemical equilibrium, and thermal freeze-out temperature at $T_f = 140$ MeV. In fact, this hydro-model calculation is known to well reproduce experimental results of single particle p_{T} spectra for various particle species at various rapidities as well as elliptic flows. The comparison with the theoretical predictions indicates that Hirano's hydro-model well reproduces the k_{T} dependence of R_{long}. However the k_{T} dependences of transverse radii, R_{side} and R_{out}, are still under-estimated even by the model.

Fig 6.24 shows the comparison of $R_{\mathrm{out}}/R_{\mathrm{side}}$ ratios between experimental and theoretical results as a function of k_{T}. The R_{out} ratios measured at CERES for $\sqrt{s_{\mathrm{NN}}} = 17.3$ GeV [35] are also overlaid on the figure, which are obtained with *full* and *partial* Coulomb corrections as well. The $R_{\mathrm{out}}/R_{\mathrm{side}}$ ratios measured at PHENIX shows a similar trend as those of the CERES results – $R_{\mathrm{out}}/R_{\mathrm{side}}$ decreases as k_{T} increases and results from *partial* Coulomb correction are significantly larger than those of the *full* Coulomb correction. As indicated by this comparison, $R_{\mathrm{out}}/R_{\mathrm{side}}$ ratios from different collision energies are indeed similar – e.g. at $k_{\mathrm{T}} = 0.3 - 0.4$ GeV/c, $R_{\mathrm{out}}/R_{\mathrm{side}}$ are $\sim 1.0 - 1.1$ with *partial* Coulomb correction while $\sim 0.7 - 0.9$ with *full* Coulomb correction. This result possibly excludes a theoretical prediction that the $R_{\mathrm{out}}/R_{\mathrm{side}}$ increases as k_{T} increases because pairs at high k_{T} would predominantly come from a hadronic re-scattering phase [30].

These detailed measurements of the transverse momentum dependence of the HBT radii, in particular that of $R_{\mathrm{out}}/R_{\mathrm{side}}$, are expected to provide strong constraints for model builders. The improved *partial* Coulomb correction, which yields higher values of $R_{\mathrm{out}}/R_{\mathrm{side}}$, certainly help to the solve the RHIC-HBT puzzle.

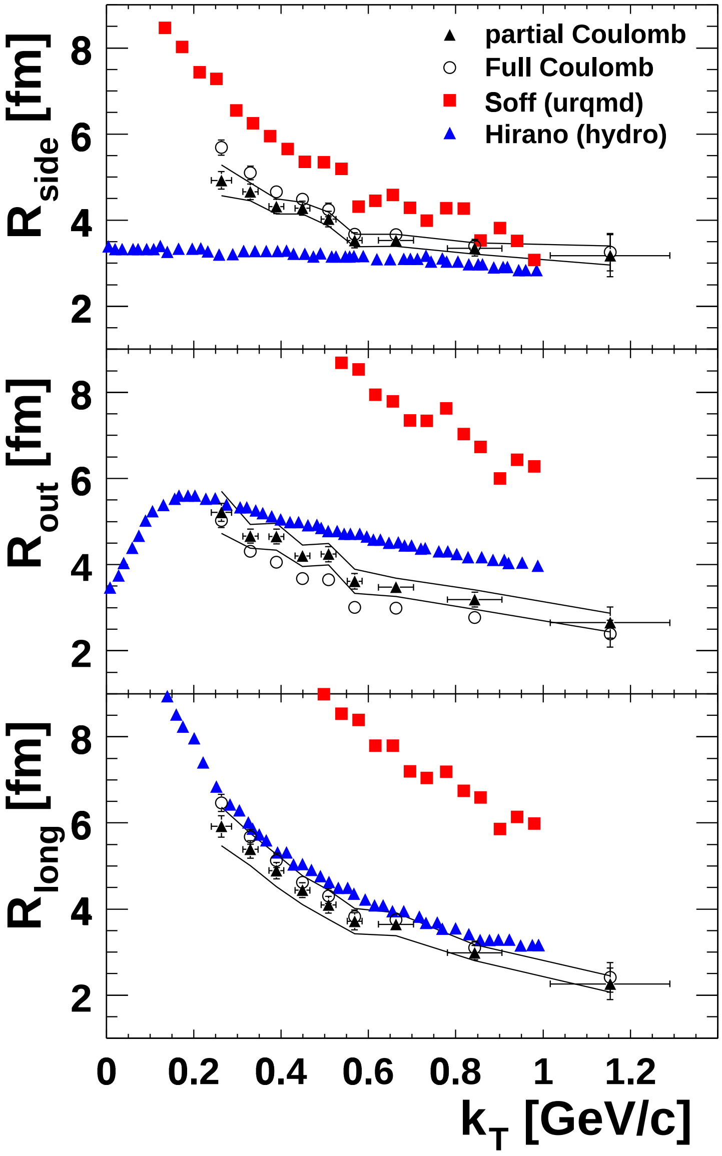

Figure 6.23: k_{T} dependence of Bertsch-Pratt radius parameters for $\pi^-\pi^-$ with *partial* (filled triangle) and *full* Coulomb (open circle) corrections, with statistical error bars and systematic error bands. Recent theoretical predictions based upon uRQMD [30] and hydrodynamics [64] calculations are shown by red and blue squares.

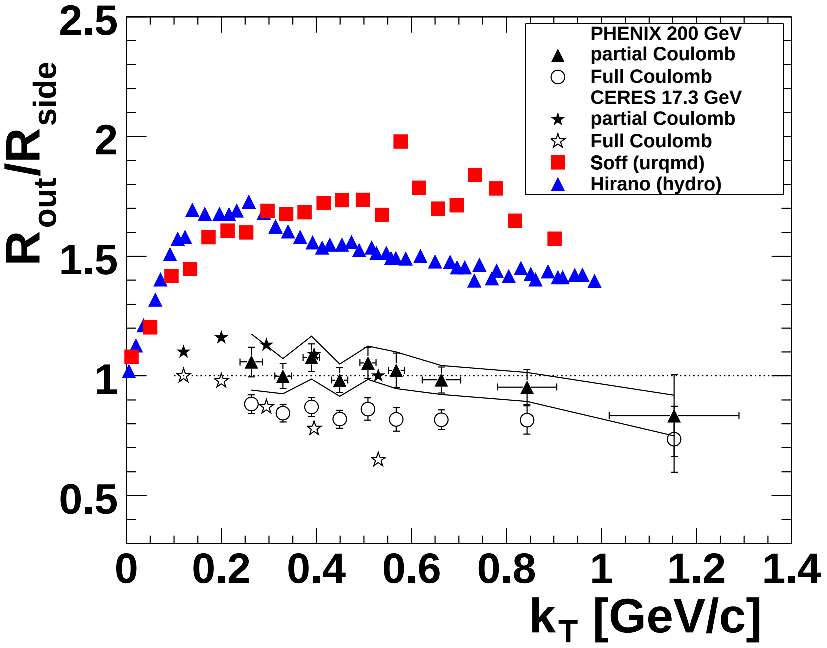

Figure 6.24: k_T dependence of R_{out}/R_{side} ratios for $\pi^-\pi^-$ with *partial* Coulomb (filled triangle) and *full* Coulomb (open circle) corrections, with statistical error bars and systematic error bands. Recent theoretical predictions based upon uRQMD [30] and hydrodynamics [64] calculations are shown by red and blue squares. Results from CERES with the *partial* and *full* Coulomb corrections are shown by filled and open stars, respectively.

Chapter 7

Conclusion

The Bose-Einstein correlations of like-sign pion pairs, $\pi^+\pi^+$ and $\pi^-\pi^-$, are measured at the mid-rapidity in Au+Au collisions at $\sqrt{s_{\mathrm{NN}}} = 200$ GeV for the first time by using high statistics data taken by PHENIX at RHIC.

To assess the conventional *full* Coulomb correction for $\pi^+\pi^+$ and $\pi^-\pi^-$ used in most earlier analyses, I also measured the $\pi^+\pi^-$ correlation function using the same real data sample. From the study, it is found that the realistic Coulomb strength for charged pion pairs is 50% of the conventional Coulomb correction. Such a dilution could be explained as a picture that, in relativistic heavy-ion collisions, many charged pions are originate from long-lived particles (e.g. η, η') and their Coulomb interactions are negligibly small. On the other hand, charged pions originate from a well-localized "core" source are eligible for the *full* Coulomb correction. To solve this issue, I applied a well improved Coulomb correction based on a picture of "core-halo" structure of source.

The Bertsch-Pratt parameterization in a longitudinally centre-of-mass frame is used to analyze the correlation functions to extract multi-dimensional HBT radii, R_{long}, R_{side} and R_{out}, and the emission duration of particles evaluated by $R_{\mathrm{out}}/R_{\mathrm{side}}$. At central nucleus-nucleus collisions, the comparison of the HBT radii to those measured at earlier experiments reveals a fact that the transverse HBT radii, R_{side} and R_{out} are less sensitive to the energy of collision, while the longitudinal HBT radius, R_{long}, slightly increases as the collision energy increases.

To investigate the space-time evolution of the overlap region between its initial and final state, the HBT radii are measured as a function of collision centrality. The centrality dependence is reasonably fitted by a linear function of the cube root of the number of participants, $p_0 + p_1 \times {N_{\mathrm{part}}}^{1/3}$, yielding $p_1 \sim 0.5$ for all radius parameters. The degrees of ${N_{\mathrm{part}}}^{1/3}$ dependence of R_{side} and R_{out} are similar to the results from the same examination at $\sqrt{s_{\mathrm{NN}}} \sim 4 - 5$ GeV at AGS. On the other hand, R_{long} shows stronger ${N_{\mathrm{part}}}^{1/3}$ dependence, namely the difference of R_{long} between AGS and RHIC energies are significant at central collisions while those are consistent at peripheral collisions.

To study the dynamics of an expanding source, I have measured the mean transverse momentum of pair (k_{T}) dependence of the measured HBT radii. All HBT radii are decrease from $\sim 5 - 6$ fm to $\sim 2 - 3$ fm as k_{T} increases from $\sim$0.2 to $\sim$1.2 GeV/c. The strong k_{T} dependence of the transverse HBT radii is explained by a picture of source which rapidly expands in transverse direction with a strong collective flow. Assuming that charged pions are freezed out at the temperature $T_0 = 120$ MeV with the transverse flow velocity $\beta_{\mathrm{T}} = 0.7$ obtained from its p_{T} spectrum, model fits to the k_{T} dependence of R_{side} and R_{long} yield the geometrical Gaussian width of the system about 7 fm, which is significantly larger than the comparable Gaussian width of Au nucleon of 3.07 fm. From a model fit to the k_{T} dependence of R_{long} provided the life time of the system about 8$-$9 fm/c. The comparisons to earlier experimental results at lower energies shows that the R_{geom} and τ slightly increase with the collision energy. The reason that the transverse HBT radii are less sensitive to the collision energy in spite of the the increase of R_{geom}, is reasonably explained by the fact that the β_{T} increases from 0.4 to 0.7 between AGS and RHIC energies.

With the conventional *full* Coulomb correction, the $R_{\mathrm{out}}/R_{\mathrm{side}}$ ratio, which has been naively considered to become more than unity in case of the finite emission duration of particles, is about 0.6-0.8 for $0.2 < k_{\mathrm{T}} < 1.2$ GeV, called “RHIC-HBT puzzle”. With the new Coulomb correction method, however, the $R_{\mathrm{out}}/R_{\mathrm{side}}$ ratio is systematically larger than that of the conventional Coulomb correction, being about 0.8-1.1 for $0.2 < k_{\mathrm{T}} < 1.2$

GeV. As a result the RHIC-HBT puzzle has been partially solved by using the improved Coulomb correction.

These results generally describe a picture that, in relativistic heavy-ion collisions at $\sqrt{s_{\rm NN}} = 200$ GeV, the system lasts about $\tau = 8 - 9$ fm/c expanding from $R_{\rm geom} = 3.07$ fm to ∼7 fm with a strong collective flow, then rapidly freeze out in a few fm/c.

However, hydrodynamical calculations, which are based on a first-order phase transition, is still unable to describe the experimental HBT radii, especially such a very small emission duration, while they can well reproduce single momentum spectra and the elliptic flow simultaneously. A few scenario would be able to explain this discrepancy. One possibility is that there actually is no such a long emission duration of particles – without the first-order phase transition, or via a "super-cooled" QGP. Secondly, some effects, which could effectively shrink the measured $R_{\rm out}$ size, are considered – a source opacity stemming from hadronic rescatterings or the two-particle correlation of jet fragmentations which significantly contributes only at the source surface. Moreover, recent lattice QCD calculations are actually suggesting the crossover phase transition from the QGP to hadronic state, not the first-order phase transition [65]. In case, the increases of the source size and the emission duration would not take place during the transition. Thus, detailed studies of the Bose-Einstein correlations in this thesis provide strong constraints for hydrodynamics and transport theories in relativistic heavy-ion collisions.

Data Tables

28163	28170	28199	28209	28212	28284	28286	28302	28444	28447
28450	28479	28483	28485	28488	28490	28570	28573	28577	28623
28625	28627	28632	28717	28718	28749	28750	28751	28761	28765
28768	28775	28777	28781	28791	28794	28798	28902	28903	28956
28958	28961	28962	28966	28968	28971	28972	28973	28987	29014
29015	29016	29017	29035	29036	29116	29122	29146	29171	29178
29179	29183	29184	29185	29186	29190	29197	29212	29213	29255
29267	29268	29354	29355	29368	29372	29380	29386	29392	29393
29401	29404	29445	29446	29454	29459	29461	29510	29512	29514
29515	29529	29531	29534	29536	29537	29555	29561	29562	29563
29566	29980	29982	29987	29989	29991	29999	30000	30001	30002
30003	30007	30008	30009	30010	30014	30015	30019	30060	30062
30069	30074	30087	30088	30112	30113	30117	30119	30123	30126
30128	30148	30149	30153	30158	30159	30193	30195	30196	30197
30218	30292	30321	30326	30329	30350	30356	30358	30388	30631
30633	30637	30642	30650	30807	30812	30813	30814	30816	30820
30910	30911	30913	30916	30917	30920	31009	31013	31014	31021
31024	31025	31058	31060	31072	31075	31076	31079	31080	31140
31143	31145	31147	31148	31152	31230	31232	31233	31239	31240
31243	31244	31249	31252	31254	31256	31343	31459	31460	31463
31464	31497	31500	31503	31515	31517	31520	31628	31631	31633
31637	31639	31641	31807	31811	31814	31815	31824	31831	31836
31837	31868	31870	32010	32017	32028	32043	32123	32127	32128
32217	32218	32222	32239	32241	32242	32271	32272	32279	32280
32367	32382	32385	32387	32435	32437	32438	32440	32441	32523
32524	32525	32526	32548	32549	32709	32713	32716	32719	32720
32721	32722	32747	32912	32913	32914	32929	32934	32948	32949
33049	33050	33051	33055	33056	33064	33067	33068	33082	33083
33085	33095	33098	33113	33119	33123	33124	33149	33150	33161
33166	33168	33169	33295	33298	33299	33303	33308	33309	33314
33321	33323	33327	33336	33337	33345	33388	33392	33393	33460
33463	33468	33526	33535	33541	33542	33547	33550	33557	33577
33608	33609	33610	33611	33612	33693	33694			

Table 7.1: Run list for the PHENIX Run2-HBT analysis.

cent.	$\langle N_{\text{part}}\rangle^{1/3}$	corr.	$\lambda_{\text{inv}}(\pi^+\pi^+)$	$R_{\text{inv}}(\pi^+\pi^+)$	$lami(\pi^-\pi^-)$	$R_{\text{inv}}(\pi^-\pi^-)$
0- 5	7.06±0.06	P.C.	0.215±0.015	6.05±0.18	0.240±0.015	6.05±0.16
		F.C.	0.352±0.010	6.06±0.09	0.375±0.010	6.11±0.09
		50%	0.269±0.013	6.15±0.15	0.291±0.013	6.16±0.14
5-10	6.69±0.09	P.C.	0.243±0.017	5.67±0.17	0.237±0.015	5.54±0.15
		F.C.	0.374±0.011	5.74±0.09	0.363±0.010	5.65±0.09
		50%	0.295±0.015	5.80±0.15	0.282±0.013	5.62±0.13
10-15	6.33±0.11	P.C.	0.248±0.019	5.58±0.20	0.240±0.016	5.27±0.17
		F.C.	0.379±0.014	5.70±0.11	0.368±0.012	5.42±0.10
		50%	0.301±0.017	5.74±0.18	0.287±0.015	5.41±0.15
15-20	5.99±0.15	P.C.	0.245±0.019	5.06±0.19	0.290±0.020	5.42±0.18
		F.C.	0.370±0.014	5.28±0.11	0.411±0.014	5.55±0.10
		50%	0.292±0.017	5.21±0.17	0.330±0.018	5.51±0.16
20-30	5.53±0.17	P.C.	0.255±0.016	4.77±0.15	0.255±0.015	4.76±0.14
		F.C.	0.375±0.012	4.98±0.09	0.370±0.011	4.95±0.08
		50%	0.299±0.014	4.89±0.13	0.296±0.013	4.87±0.12
30-40	4.89±0.20	P.C.	0.301±0.023	4.76±0.18	0.275±0.019	4.32±0.16
		F.C.	0.413±0.016	4.92±0.11	0.384±0.014	4.52±0.10
		50%	0.335±0.020	4.83±0.17	0.310±0.017	4.43±0.15
40-50	4.24±0.22	P.C.	0.309±0.028	4.04±0.20	0.330±0.028	4.22±0.19
		F.C.	0.410±0.021	4.25±0.13	0.423±0.019	4.36±0.12
		50%	0.342±0.026	4.14±0.19	0.354±0.025	4.27±0.17
50-65	3.54±0.27	P.C.	0.376±0.039	3.81±0.23	0.332±0.032	3.52±0.21
		F.C.	0.466±0.028	4.03±0.15	0.416±0.022	3.67±0.13
		50%	0.395±0.035	3.85±0.22	0.353±0.029	3.57±0.19
65-92	2.58±0.50	P.C.	0.329±0.071	3.13±0.47	0.289±0.045	2.40±0.40
		F.C.	0.397±0.049	3.25±0.28	0.359±0.030	2.33±0.24
		50%	0.347±0.065	3.17±0.44	0.307±0.043	2.47±0.38

Table 7.2: 1-dimensional fit parameters from $\pi^+\pi^+$ and $\pi^-\pi^-$ for nine centrality classes for 0.2< k_{T} <2.0 GeV/c with $\langle k_{\text{T}}\rangle$ ~0.45 GeV/c, with fits of Eq. 5.3 (P.C.), Eq. 2.15 (F.C.) and Eq. 5.7 with $lambda_{+-} = 0.5$ (50%). Centrality is in %, and all radii are in fm. Errors are statistical only.

cent.	$\langle N_{\text{part}}\rangle^{1/3}$	corr.	λ	R_{side}	R_{out}	R_{long}
0- 5	7.06±0.06	P.C.	0.308±0.017	4.54±0.17	4.90±0.18	4.85±0.19
		F.C.	0.417±0.015	4.90±0.13	4.10±0.12	5.18±0.15
		50%	0.341±0.015	4.67±0.15	4.68±0.17	4.98±0.17
5-10	6.69±0.09	P.C.	0.324±0.018	4.25±0.16	4.31±0.16	4.42±0.18
		F.C.	0.436±0.016	4.61±0.13	3.78±0.12	4.80±0.15
		50%	0.358±0.016	4.37±0.15	4.19±0.15	4.57±0.17
10-15	6.33±0.11	P.C.	0.338±0.020	4.14±0.17	4.42±0.17	4.18±0.20
		F.C.	0.452±0.018	4.53±0.14	3.95±0.13	4.60±0.17
		50%	0.371±0.018	4.26±0.16	4.34±0.17	4.33±0.19
15-20	5.99±0.15	P.C.	0.357±0.022	4.05±0.17	4.15±0.17	4.03±0.19
		F.C.	0.456±0.019	4.36±0.14	3.75±0.14	4.35±0.16
		50%	0.381±0.019	4.13±0.16	4.08±0.17	4.12±0.18
20-30	5.53±0.17	P.C.	0.349±0.017	3.67±0.12	3.71±0.13	3.70±0.15
		F.C.	0.446±0.016	3.96±0.11	3.41±0.11	4.04±0.13
		50%	0.375±0.015	3.75±0.12	3.65±0.13	3.80±0.14
30-40	4.89±0.20	P.C.	0.374±0.025	3.45±0.16	3.42±0.16	3.50±0.21
		F.C.	0.460±0.021	3.70±0.14	3.18±0.13	3.76±0.16
		50%	0.393±0.021	3.51±0.14	3.38±0.16	3.56±0.18
40-50	4.24±0.22	P.C.	0.427±0.031	3.03±0.17	3.26±0.18	3.18±0.20
		F.C.	0.498±0.028	3.21±0.15	3.11±0.15	3.36±0.18
		50%	0.437±0.028	3.06±0.16	3.25±0.18	3.21±0.19
50-65	3.54±0.27	P.C.	0.455±0.044	2.95±0.20	2.75±0.22	3.19±0.30
		F.C.	0.517±0.039	3.07±0.19	2.65±0.19	3.33±0.27
		50%	0.461±0.040	2.96±0.20	2.74±0.22	3.21±0.29
65-92	2.58±0.50	P.C.	0.423±0.085	2.48±0.46	2.83±0.63	2.25±0.38
		F.C.	0.467±0.075	2.59±0.42	2.66±0.52	2.34±0.35
		50%	0.427±0.077	2.49±0.45	2.79±0.62	2.26±0.37

Table 7.3: Bertsch-Pratt fit parameters from $\pi^+\pi^+$ for nine centrality classes for $0.2< k_{\mathrm{T}} <2.0$ GeV/c with $\langle k_{\mathrm{T}}\rangle \sim 0.45$ GeV/c, with fits of Eq. 5.3 (P.C.), Eq. 2.15 (F.C.) and Eq. 5.7 with $lambda_{+-} = 0.5$ (50%). Centrality is in %, and all radii are in fm. Errors are statistical only.

cent.	$\langle N_{\rm part}\rangle^{1/3}$	corr.	λ	$R_{\rm side}$	$R_{\rm out}$	$R_{\rm long}$
0- 5	7.06±0.06	P.C.	0.351±0.018	4.61±0.15	4.83±0.16	5.06±0.18
		F.C.	0.452±0.015	4.95±0.12	4.17±0.11	5.29±0.14
		50%	0.374±0.015	4.69±0.14	4.68±0.15	5.12±0.16
5-10	6.69±0.09	P.C.	0.328±0.017	4.32±0.15	4.24±0.16	4.62±0.18
		F.C.	0.427±0.015	4.63±0.12	3.68±0.11	4.88±0.14
		50%	0.354±0.015	4.41±0.14	4.09±0.15	4.70±0.17
10-15	6.33±0.11	P.C.	0.327±0.018	3.98±0.15	4.11±0.16	4.20±0.17
		F.C.	0.428±0.016	4.33±0.13	3.60±0.12	4.48±0.14
		50%	0.354±0.016	4.08±0.14	4.00±0.16	4.29±0.16
15-20	5.99±0.15	P.C.	0.366±0.022	4.04±0.17	4.02±0.16	4.22±0.20
		F.C.	0.467±0.019	4.37±0.14	3.64±0.13	4.54±0.16
		50%	0.391±0.019	4.12±0.16	3.96±0.16	4.31±0.19
20-30	5.53±0.17	P.C.	0.364±0.017	3.70±0.13	3.88±0.13	3.86±0.14
		F.C.	0.454±0.015	4.00±0.11	3.54±0.11	4.13±0.12
		50%	0.385±0.015	3.77±0.12	3.81±0.13	3.92±0.13
30-40	4.89±0.20	P.C.	0.345±0.020	3.18±0.15	3.27±0.15	3.41±0.17
		F.C.	0.433±0.018	3.46±0.13	3.01±0.12	3.67±0.14
		50%	0.367±0.018	3.25±0.14	3.23±0.15	3.48±0.16
40-50	4.24±0.22	P.C.	0.432±0.031	3.08±0.17	3.15±0.17	3.42±0.21
		F.C.	0.500±0.027	3.26±0.16	3.00±0.15	3.57±0.19
		50%	0.438±0.027	3.09±0.17	3.13±0.17	3.43±0.20
50-65	3.54±0.27	P.C.	0.395±0.033	2.65±0.20	2.53±0.20	2.54±0.20
		F.C.	0.462±0.031	2.81±0.19	2.42±0.17	2.71±0.18
		50%	0.407±0.030	2.68±0.20	2.52±0.20	2.57±0.20
65-92	2.58±0.50	P.C.	0.371±0.061	1.97±0.34	2.25±0.54	2.19±0.35
		F.C.	0.420±0.056	2.09±0.33	2.10±0.44	2.25±0.32
		50%	0.379±0.057	2.00±0.34	2.22±0.53	2.20±0.34

Table 7.4: Bertsch-Pratt fit parameters from $\pi^-\pi^-$ for nine centrality classes for $0.2 < k_{\rm T} < 2.0$ GeV/c with $\langle k_{\rm T}\rangle \sim 0.45$ GeV/c, with fits of Eq. 5.3 (P.C.), Eq. 2.15 (F.C.) and Eq. 5.7 with $lambda_{+-} = 0.5$ (50%). Centrality is in %, and all radii are in fm. Errors are statistical only.

k_{T} range	$\langle k_{\mathrm{T}} \rangle$	corr.	$\lambda_{\mathrm{inv}}(\pi^+\pi^+)$	$R_{\mathrm{inv}}(\pi^+\pi^+)$	$lami(\pi^-\pi^-)$	$R_{\mathrm{inv}}(\pi^-\pi^-)$
0.20-0.30	0.27±0.02	P.C.	0.248±0.018	6.45±0.22	0.257±0.018	6.62±0.21
		F.C.	0.427±0.013	7.04±0.13	0.431±0.013	7.15±0.12
		50%	0.311±0.016	6.60±0.19	0.312±0.015	6.68±0.18
0.30-0.36	0.33±0.02	P.C.	0.303±0.022	6.50±0.19	0.311±0.020	6.27±0.18
		F.C.	0.444±0.015	6.70±0.12	0.444±0.014	6.47±0.11
		50%	0.348±0.018	6.54±0.18	0.350±0.017	6.30±0.16
0.36-0.42	0.39±0.02	P.C.	0.250±0.019	5.66±0.19	0.272±0.019	5.78±0.19
		F.C.	0.377±0.013	5.79±0.11	0.396±0.013	5.94±0.11
		50%	0.295±0.016	5.72±0.17	0.313±0.017	5.82±0.17
0.42-0.48	0.45±0.02	P.C.	0.254±0.021	5.49±0.20	0.263±0.020	5.44±0.18
		F.C.	0.369±0.014	5.58±0.11	0.376±0.014	5.58±0.11
		50%	0.294±0.018	5.54±0.18	0.301±0.017	5.49±0.17
0.48-0.54	0.51±0.02	P.C.	0.263±0.027	5.57±0.25	0.265±0.027	5.64±0.25
		F.C.	0.369±0.018	5.54±0.14	0.371±0.018	5.62±0.14
		50%	0.303±0.024	5.61±0.23	0.305±0.023	5.69±0.22
0.54-0.60	0.57±0.02	P.C.	0.205±0.025	4.73±0.29	0.206±0.020	4.50±0.22
		F.C.	0.311±0.018	4.84±0.15	0.307±0.015	4.64±0.12
		50%	0.247±0.023	4.85±0.25	0.244±0.019	4.60±0.20
0.60-0.75	0.66±0.04	P.C.	0.189±0.023	4.61±0.28	0.232±0.024	4.98±0.23
		F.C.	0.286±0.016	4.61±0.14	0.324±0.016	4.90±0.12
		50%	0.231±0.022	4.73±0.24	0.267±0.021	5.02±0.21
0.75-1.00	0.84±0.06	P.C.	0.150±0.022	3.52±0.31	0.161±0.025	3.89±0.33
		F.C.	0.239±0.017	3.80±0.16	0.239±0.018	3.88±0.17
		50%	0.184±0.022	3.70±0.28	0.196±0.024	4.03±0.29
1.00-2.00	1.15±0.14	P.C.	0.121±0.036	2.87±0.64	0.134±0.063	3.76±0.89
		F.C.	0.185±0.027	2.90±0.30	0.204±0.042	3.64±0.41
		50%	0.144±0.038	3.02±0.56	0.165±0.062	3.87±0.76

Table 7.5: 1-dimensional fit parameters from $\pi^+\pi^+$ and $\pi^-\pi^-$ for nine k_{T} classes at the top 0-30% centrality with N_{part} ~280, with fits of Eq. 5.3 (P.C.), Eq. 2.11 (F.C.) and Eq. 5.7 with $lambda_{+-} = 0.5$ (50%). k_{T} range and $\langle k_{\mathrm{T}} \rangle$ are in GeV/c, and R_{inv} is in fm. Errors are statistical only.

k_T range	$\langle k_T \rangle$	corr.	λ	R_{side}	R_{out}	R_{long}
0.20-0.30	0.27±0.02	P.C.	0.288±0.018	4.67±0.20	4.93±0.21	5.86±0.27
		F.C.	0.459±0.017	5.51±0.17	4.82±0.15	6.53±0.21
		50%	0.338±0.016	4.90±0.18	4.69±0.19	6.01±0.24
0.30-0.36	0.33±0.02	P.C.	0.389±0.023	4.70±0.19	4.94±0.17	5.17±0.22
		F.C.	0.507±0.020	5.17±0.16	4.53±0.14	5.56±0.18
		50%	0.415±0.020	4.80±0.18	4.84±0.17	5.25±0.21
0.36-0.42	0.39±0.02	P.C.	0.366±0.022	4.15±0.17	4.39±0.18	4.75±0.21
		F.C.	0.460±0.019	4.50±0.14	3.70±0.13	5.03±0.17
		50%	0.391±0.020	4.24±0.16	4.28±0.18	4.84±0.20
0.42-0.48	0.45±0.02	P.C.	0.421±0.026	4.02±0.16	4.18±0.16	4.45±0.20
		F.C.	0.493±0.022	4.23±0.14	3.60±0.13	4.63±0.17
		50%	0.432±0.023	4.05±0.15	4.13±0.17	4.48±0.20
0.48-0.54	0.51±0.02	P.C.	0.430±0.030	3.93±0.18	3.99±0.17	3.99±0.20
		F.C.	0.497±0.026	4.12±0.16	3.41±0.14	4.21±0.18
		50%	0.439±0.027	3.95±0.17	3.95±0.17	4.02±0.20
0.54-0.60	0.57±0.02	P.C.	0.433±0.036	3.88±0.21	3.60±0.20	3.79±0.21
		F.C.	0.484±0.031	3.97±0.18	2.97±0.16	3.93±0.18
		50%	0.446±0.033	3.92±0.21	3.59±0.20	3.82±0.21
0.60-0.75	0.66±0.04	P.C.	0.437±0.029	3.57±0.16	3.46±0.15	3.30±0.15
		F.C.	0.484±0.026	3.68±0.14	2.90±0.12	3.44±0.14
		50%	0.443±0.027	3.59±0.15	3.44±0.16	3.31±0.15
0.75-1.00	0.84±0.06	P.C.	0.480±0.040	3.33±0.19	2.91±0.17	2.89±0.16
		F.C.	0.519±0.036	3.38±0.17	2.50±0.14	2.99±0.15
		50%	0.482±0.037	3.33±0.18	2.90±0.17	2.89±0.16
1.00-2.00	1.15±0.14	P.C.	0.363±0.066	2.64±0.38	2.06±0.37	1.97±0.31
		F.C.	0.409±0.060	2.67±0.34	1.75±0.25	2.10±0.28
		50%	0.370±0.064	2.66±0.37	2.06±0.37	1.99±0.30

Table 7.6: Bertsch-Pratt fit parameters from $\pi^+\pi^+$ for nine k_T classes at the top 0-30% centrality with N_{part} ~280, with fits of Eq. 5.3 (P.C.), Eq. 2.11 (F.C.) and Eq. 5.7 with $lambda_{+-} = 0.5$ (50%). k_T range and $\langle k_T \rangle$ are in GeV/c, and all radii are in fm. Errors are statistical only.

k_{T} range	$\langle k_{\mathrm{T}} \rangle$	corr.	λ	R_{side}	R_{out}	R_{long}
0.20-0.30	0.27±0.02	P.C.	0.307±0.018	4.92±0.21	5.21±0.21	5.92±0.25
		F.C.	0.464±0.017	5.69±0.18	5.02±0.16	6.47±0.20
		50%	0.348±0.015	5.09±0.19	4.94±0.19	5.99±0.22
0.30-0.36	0.33±0.02	P.C.	0.401±0.022	4.66±0.18	4.66±0.16	5.38±0.20
		F.C.	0.513±0.019	5.10±0.16	4.30±0.13	5.68±0.17
		50%	0.422±0.019	4.73±0.17	4.57±0.17	5.43±0.19
0.36-0.42	0.39±0.02	P.C.	0.420±0.024	4.32±0.17	4.65±0.17	4.89±0.19
		F.C.	0.507±0.021	4.66±0.15	4.05±0.14	5.13±0.17
		50%	0.436±0.021	4.37±0.16	4.59±0.18	4.94±0.19
0.42-0.48	0.45±0.02	P.C.	0.448±0.025	4.28±0.16	4.20±0.15	4.44±0.17
		F.C.	0.518±0.022	4.48±0.14	3.67±0.12	4.62±0.15
		50%	0.455±0.022	4.29±0.16	4.17±0.16	4.45±0.17
0.48-0.54	0.51±0.02	P.C.	0.462±0.030	4.02±0.18	4.24±0.17	4.10±0.19
		F.C.	0.526±0.026	4.24±0.16	3.65±0.14	4.31±0.17
		50%	0.471±0.027	4.05±0.17	4.23±0.18	4.13±0.19
0.54-0.60	0.57±0.02	P.C.	0.433±0.032	3.53±0.18	3.62±0.18	3.72±0.20
		F.C.	0.481±0.026	3.67±0.14	3.00±0.14	3.82±0.15
		50%	0.440±0.027	3.55±0.16	3.59±0.18	3.73±0.17
0.60-0.75	0.66±0.04	P.C.	0.479±0.029	3.53±0.14	3.47±0.13	3.65±0.15
		F.C.	0.525±0.025	3.66±0.13	2.99±0.11	3.76±0.13
		50%	0.481±0.026	3.53±0.14	3.46±0.14	3.65±0.15
0.75-1.00	0.84±0.06	P.C.	0.517±0.043	3.34±0.18	3.19±0.17	2.99±0.17
		F.C.	0.553±0.039	3.40±0.16	2.77±0.15	3.10±0.16
		50%	0.517±0.041	3.34±0.18	3.19±0.19	2.99±0.17
1.00-2.00	1.15±0.14	P.C.	0.446±0.098	3.18±0.49	2.65±0.36	2.26±0.37
		F.C.	0.499±0.093	3.25±0.44	2.40±0.32	2.41±0.34
		50%	0.452±0.093	3.19±0.48	2.65±0.36	2.28±0.36

Table 7.7: Bertsch-Pratt fit parameters from $\pi^-\pi^-$ for nine k_{T} classes at the top 0-30% centrality with N_{part} ~280, with fits of Eq. 5.3 (P.C.), Eq. 2.15 (F.C.) and Eq. 5.7 with $lambda_{+-} = 0.5$ (50%). k_{T} range and $\langle k_{\mathrm{T}} \rangle$ are in GeV/c, and all radii are in fm. Errors are statistical only.

Bibliography

[1] M. Jacob and U. Heinz, CERN press release, Feb. 2000.

[2] C. Lourenco, Proc. of QM'01, Nucl. Phys. **A698**, 13-22 (2002).

[3] L.D. McLerran and T. Toimcla, Phys. Rev. **D31**, 545 (1985).

[4] K. Kajantie *et al.*, Phys. Rev. **D34**, 274 (1986).

[5] S.S. Adler *et al.*, (PHENIX Collaboration), Phys. Rev. **C69**, 034909 (2004).

[6] J. Adams *et al.*, (STAR Collaboration), nucl-ex/0310004.

[7] M. Gyulassy and X. N. Wang, Nucl. Phys. **B420**, 583 (1994).

[8] S.S. Adler *et al.*, (PHENIX Collaboration), nucl-ex/0305013.

[9] J. Adams *et al.*, (STAR Collaboration), nucl-ex/0306007.

[10] T. Matsui and H. Satz, Phys. Lett. **B178**, 416 (1986).

[11] M.C. Abreu *et al.*, (NA50 Collaboration), Phys. Lett. **B450**, 456 (1999).

[12] S.S. Adler *et al.*, (PHENIX Collaboration), Phys. Rev. Lett. **91**, 072303 (2003).

[13] J. Adams *et al.*, (STAR Collaboration), Phys. Rev. Lett. **91**, 072304 (2003).

[14] G.E. Brown *et al.*, Phys. Rev. **C43**, 1881 (1991).

[15] G. Agakichiev *et al.*, (CERES Collaboration), nucl-ex/9910015.

[16] T. Hatsuda and S.H. Lee, Phys. Rev. **C46**, 34 (1992).

[17] R. Hanbury Brown and R. Twiss, Philos. Mag. **597**, (1954) 663.

[18] D.H. Rischke and M. Gyulassy, Nucl. Phys. **A597**, 701-726 (1996).

[19] G. Goldhaber, S. Goldhaber, W. Lee and A. Pais, Phys. Rev. **120**, 300 (1960).

[20] S. Pratt, Phys. Rev. Lett. **53**, 1219 (1984).

[21] G. Bertsch and G.E. Brown, Phys. Rev. **C40**, 1830 (1989).

[22] M. Gyulassy and S. Padula, Phys. Lett. **B217**, 181 (1988).

[23] W.A. Zajc *et al.*, Phys. Rev. **C29**, 2173 (1984).

[24] L. Ahle *et al.*, Phys. Rev. **C66**, 054906 (2002).

[25] M. Lisa *et al.*, Phys. Rev. Lett. **84**, 2798 (2000).

[26] M.M. Aggarwal *et al.*, Eur. Phys. J. **C16**, 445 (2000).

[27] I.G. Bearden *et al.*, Phys. Rev. **C58**, 1656 (1998).

[28] C. Adler *et al.*, Phys. Rev. Lett. **87**, 082301 (2001).

[29] K. Adcox *et al.*, Phys. Rev. Lett. **88**, 192302 (2002).

[30] S. Soff, S.A. Bass, and A. Dumitru, Phys. Rev. Lett. **86**, 3981 (2001).

[31] U. Heinz and P.F. Kolb, hep-ph/0204061.

[32] K. Adcox *et al.*, Phys. Rev. **C88**, 192302 (2003).

[33] Y.M. Sinyukov, R. Lednicky, S.V. Akkelin, J. Pluta, B. Erazmus, Phys. Lett. **B432**, 248 (1998).

[34] T. Csörgő *et al.*, Eur. Phys. J. **C9**, 275 (1999).

[35] D. Adamova *et al.*, nucl-ex/0207005.

[36] H. Hahn *et al.*, Nucl. Instrum. Methods **A499**, 245-263 (2003).

[37] K. Adcox *et al.*, Nucl. Instrum. Methods **A499**, 469-602 (2003).

[38] J. Murata *et al.*, nucl-ex/0212027.

[39] K. Ikematsu *et al.*, Nucl. Instrum. Methods **A411** 238 (1998).

[40] C. Adler *et al.*, nucl-ex/0008005.

[41] A. Oskarsson *et al.*, Nucl. Instrum. Methods **A497**/2-3 pp 263-293 (2003).

[42] Y. Akiba *et al.*, Nucl. Instrum. Methods **A433**, 143-148 (1999).

[43] T.C. Awes *et al.*, nucl-ex/0202009.

[44] J.T. Mitchell *et al.*, Nucl. Instrum. Methods **A482**, 498 (2002).

[45] J.M. Burward-Hoy, Ph.D thesis, Stony Brook, State University of New York (2001).

[46] R. Averbeck, J. Burward-Hoy, T. Chujo, A. Drees, A. Kiyomichi, F. Messer, F. Muehlbacher, H. Ohnishi, J. Velkovska, Internal PHENIX Analysis Note 37 (2001).

[47] http://nt3.phys.columbia.edu/people/molnard/OSCAR/

[48] GEANT 3.2.1, CERN program library.

[49] S. Pratt, Phys. Rev. **D33**, 72 (1986).

[50] A. Messiah, *Quantum Mechsnics Vol. 1* (North-Holland, Amsterdam, 1961).

[51] T. Mizoguchi, M. Biyajima, Phys. Lett. **B499**, 245 (2001).

[52] S. Pratt, T. Csörgő, J. Zimányi, Phys. Rev. **C42**, 2646 (1990).

[53] http://root.cern.ch/

[54] Nu Xu and Masashi Kaneta, Nucl. Phys. **A698**, 306 (2002).

[55] J.L. Nagle, M. Chiu, J. Frantz, K. Reygers, *Minimum Bias Trigger Selection and Centrality Note*, PHENIX Analysis note 113.

[56] R. Glauber and J. Natthiae, Nucl. Phys. **B21**, 135 (1970).

[57] K. Adcox *et al.*, Phys. Rev. Lett. **86**, 3500 (2001).

[58] C. Albajar *et al.*, Phys. Lett. **B86**, 410 (1989).

[59] T. Alexopoulos *et al.*, Phys. Rev. **D48**, 1931 (1993).

[60] U.A. Wiedemann, P. Scotto and U. Heinz, Phys. Rev. **C53**, 918 (1996).

[61] S Chapman, P. Scotto and U. Heinz, Phys. Rev. Lett. **74**, 4400 (1995); Heavy Ion Phys. **1**, 1 (1995).

[62] A.N. Makhlin and Yu.M. Sinyukov, Z. Phys. **C39**, 69 (1988).

[63] J.M. Burward-Hoy, Nucl. Phys. **A715**, 498c-501c (2003).

[64] T. Hirano and K. Tsuda, nucl-th/0208068.

[65] V.D. Toneev, nucl-th/0210039.